Towards Understanding the Interaction of Water with α-Al$_2$O$_3$ Surfaces: a Sum Frequency Generation Perspective

Inaugural-Dissertation

to obtain the academic degree

Doctor rerum naturalium

(Dr. rer. nat.)

submitted to the Department of Biology, Chemistry and Pharmacy

of Freie Universität Berlin

by

YANHUA YUE

2019

This work was done between October 2014 and Octorber 2019 in the Department of Physical Chemistry at the Fritz-Haber-Institut of the Max Planck Gesellschaft.

1st Reviewer: Prof. Dr. Martin Wolf
2nd Reviewer: Prof. Dr. Thomas Risse

Date of defense: 6th, Dec., 2019

Abstract

α-Al$_2$O$_3$ surfaces are omnipresent in a wide variety of applications and useful models of more complicated, environmentally abundant, alumino-silicate surfaces. Decades of work have clarified that all properties of these surfaces depend sensitively on the crystal face and the presence of even small amounts of water. This thesis aims to gain experimental insight into the interaction (adsorption structure, thermodynamic and kinetics) between water and α-Al$_2$O$_3$ using vibrational sum frequency generation (SFG) spectroscopy and Temperature Programmed Desorption (TPD).

In the first part of this thesis, I investigate uni-molecular water interaction with α-Al$_2$O$_3$ under UHV conditions. By probing the OD stretching vibration of heavy water adsorbed on the α-Al$_2$O$_3$ (11-20) surface with SFG spectroscopy I show, in conjunction with DFT calculations, the dissociative adsorption of water on this surface leads to three types of structures: the so-called inter-CUSa/Oμ2, CUSb/Oμ2 and inter-CUSb/Oμ2 (chapter 3). In chapter 4, the desorption thermodynamics and kinetics of uni-molecule water from α-Al$_2$O$_3$ (0001), (1-102) and (11-20) surfaces are systematically studied experimentally using TPD. Good agreement between these results and theory are achieved on the desorption energy of uni-molecular water from α-Al$_2$O$_3$(11-20), (1-102) and (0001), clarifying the reactivity of the three surfaces with respect to unimolecular water dissociative adsorption is (11-20)>(1-102) >(0001) and offering substantial constraints on dissociation mechanism.

In the second part of this thesis, I focus on the change in surface termination of α-Al$_2$O$_3$ (11-20) (chapter 5) and (0001) (chapter 6) as the surface is moved from UHV to ambient (and the water pressure increases by eight order of magnitude higher) with a SFG-DFT combined approach. The consistency between experiment and theory offers strong evidence that the (11-20) surface has in the absence of water one of four possible oxygen terminations, i.e. the so-called O-I, and that it is composed of doubly coordinated oxygen Al$_2$O and triply coordinated Al$_3$O in the ratio 1:2. With sub-monolayer water coverages in UHV, Al$_2$O is protonated while Al$_3$O is inactive. When the surface is exposed to water in ambient it is fully protonated and the stable surface structure is the O-III oxygen termination. This surface is composed of AlO, Al$_2$O and Al$_3$O in a ratio of 1:1:1. For the (0001) surface, it is found that termination is preparation method dependent. Preparation in UHV using annealing sputtering cycles produces one (or two possible) Al terminated surfaces, i.e. the so-called Al-I. In contrast acid etching treatment in solution yields an

oxygen terminated solid because of the dissolution of the topmost Al layer (of Al-I termination). The Al-I terminated is inert with respect to water dissociative adsorption while the O-terminated (0001) is quasi instantaneously hydroxylated in air. These findings are of crucial importance in reconciling conflicting reports of basic surface properties of these materials (e.g. different measured isoelectric points or contact angles) and suggest the possibility of a new level of control of the performance of α-Al_2O_3 in industrial applications.

As a model material, the insight into interaction between water and α-Al_2O_3 including the reactivities and the surface reconstruction of alumina from UHV to ambient conditions provides inspiration to understand water interaction with other environmentally abundant alumino-silicate materials. The SFG-DFT combined approaches as applied in this thesis can also be extended to other water/metal oxides systems, and would be of general interest to those interested in oxide/water interaction or the processes such interactions control.

Zusammenfassung

Die vorliegende Arbeit beschäftigt sich mit der Wechselwirkung zwischen Wasser und α-Al$_2$O$_3$ Oberflächen. Aluminiumoxid ist ein wichtiger Werkstoff für viele industrielle Anwendungen, dessen Oberflächenstruktur aber erheblichen Einfluss auf die Materialeigenschaften aufweist. Selbst geringe Mengen von Wasser verändern die Oberflächenstruktur und daraus folgend die chemischen Eigenschaften von Aluminiumoxid. Ziel dieser Arbeit ist es, Einblicke in die Wechselwirkung (Adsorptionsstruktur, Thermodynamik und Kinetik) zwischen Wasser und α-Al$_2$O$_3$ durch den Einsatz von optischer Schwingungsspektroskopie und Thermischer Desorptionsspektroskopie (TPD) zu gewinnen.

Der erste Teil dieser Arbeit konzentriert sich auf die Untersuchung der uni-molekularen Wasserwechselwirkung mit α-Al$_2$O$_3$(11-20) unter UHV-Bedingungen. Die Untersuchung von OD-Steckschwingungen bei schwerem Wasser mittels Summen-Frequenz-Spektroskopie (SFG) an der Oberfläche, in Verbindung mit DFT-Berechnungen, ermöglichte die Identifikation von drei favorisierten Adsorptionsstrukturen für die Dissoziation: die sogenannte inter-CUSa/Oμ2, CUSb/Oμ2 und inter-CUSb/Oμ2.   Durch Anwendung von Thermische-Desorptions-Spektroskopie (TPD) wurde ebenfalls die Desorptionskinetik von uni-molekularem Wasser auf den drei stabilsten α-Al$_2$O$_3$-Oberflächen (0001), (1-102) und (11-20) untersucht, was einen systematischen Einblick in die Thermodynamik und Kinetik der Wasser-Ad/Desorption ermöglichte. Die gute Übereinstimmung zwischen experimenteller und theoretischer Ergebnisse für die Desorptionsenergie deuten auf folgende abnehmende Reaktivität für Wasserdissoziation hin (11-20)>(1-102)>(0001) und zeigen die Abhängigkeit hierfür von der Koordination, Dichte und Topologie der Oberfläche auf.

Der zweite Teil dieser Arbeit konzentriert sich auf die Untersuchung der morphologischen Änderung der Oberflächenstruktur von α-Al$_2$O$_3$ (11-20) und (0001) beim Übergang von UHV zu Umgebungsbedingungen (und dem dadurch zunehmendem relativen Wasserdruck) mittels eines kombinierten Ansatzes aus SFG und DFT. Die Konsistenz zwischen Experiment und Theorie zeigt für (11-20), dass sie in Abwesenheit von Wasser Sauerstoff terminiert ist (die sogenannte O-I Terminierung), bestehend aus doppelt koordiniertem Sauerstoff (Al$_2$O) und dreifach koordiniertem (Al$_3$O), im Verhältnis 1:2 ; bei geringer Wasser Adsorption(<Monolage) im UHV wird Al$_2$O protoniert, während Al$_3$O inaktiv ist; wenn die Oberfläche viel Wasser ausgesetzt wird (Umgebungsbedingungen), wird die Oberfläche vollständig protoniert und zu einer O-III-Termination rekonstruiert, die aus AlO, Al$_2$O und Al$_3$O in einem Verhältnis 1:1:1 besteht. Für die (0001)-Oberfläche wurde gezeigt, dass die Terminierung

präparations Abhängig ist: bei der Präparation im UHV mit Heiz- und Sputter-Zyklen erzeugt man eine Al-terminierte Oberfläche, die sogenannte Al-I Terminierung. Im Gegensatz hierzu führt die Säureätzbehandlung zu einer O-I Terminierung aufgrund der Auflösung der obersten Al-Schicht der Al-I Terminierung. Die Al-I ist inert gegenüber dissoziativer Adsorption, während die O-Terminierung (0001) sofort in Luft hydroxyliert wird. Diese Ergebnisse sind von entscheidender Bedeutung, um die unterschiedlichen Oberflächeneigenschaften zu verstehen, die in verschiedensten vorhergehenden Arbeiten durch IEPs, Wasserkontaktwinkel usw. beobachtet wurden; ebenfalls eröffnen die Erkenntnisse Möglichkeiten, um die Eigenschaften von α-Al_2O_3 in Industrieanwendungen zu verstehen und möglicherweise zu kontrollieren.

Zusammenfassend liefert das untersuchte Modelsystem Einblicke in die Interaktion zwischen Wasser und α-Al_2O_3, einschließlich der Reaktivitäten und der Oberflächenrekonstruktion beim Übergang von UHV zu Umgebungsbedingungen und fördert das Verständnis der Wasserwechselwirkung mit anderen in der Umwelt vorkommenden Aluminium-Silikatmaterialien. Der kombinierte SFG und DFT Ansatz, wie er in dieser Arbeit angewendet wurde, kann auch auf andere Wasser/Metalloxidsysteme ausgedehnt werden und wäre somit von allgemeinem Interesse für Arbeiten, die an einer Oxid/Wasser-Wechselwirkung, sowie der Kontrolle der dabei ablaufenden Prozesse interessiert sind.

Contents

Chapter 1 Introduction

Physical and chemical phenomena at solid surfaces have been studied for centuries [1-5]. Chemical reactions at surfaces, in particular, control such processes as mineral dissolution[6, 7], corrosion[3], soil toxin and nutrient transfer in the environment[8], and underlie heterogeneous catalysis in industry[9] . Understanding the mechanism of these surface reactions is thus necessary to quantify and/or control any of these processes. For any such surface reaction, the first step, before any bond breaking or formation, is adsorption of molecules.

Two types of molecular adsorption on solid surfaces are usefully distinguished: physisorption and chemisorption. In physisorption the adsorbate interacts with the surface through Van-der-Waals forces, dipole-dipole interaction or hydrogen bonding and the adsorption energy is normally less than 50 kJ/mol. In chemisorption, strongly adsorbed molecules are often the result of a hybridization of the molecule's orbitals with the surface band structure: there is a new electronic structure of the adsorbate/surface complex. This hybridization of electronic orbitals between adsorbate and surface often induces a weakening of the internal bonds of the adsorbate and can result in its dissociation [10]. The remaining fragments typically form a chemical bond with the surface and the energies of the resulting 'chemisorption' are generally greater than 50 kJ/mol.

The general characteristics of physisorption and chemisorption are more easily understood if we consider a simplified model adsorption reaction. I imagine the adsorption of two gas molecules, AB and A_2, on a solid surface where the potential energy for both molecules along the surface normal is shown in Figure 1. 1. Clearly in case of low temperatures both gases A_2 and AB will phyisorb on the surface. If physisorption was the only adsorption channel an increase of the system's internal energy (e.g. by heating) above the zero energy line of the gas-phase would induce desorption of the molecules. But as can be seen, the potential energy surfaces for chemisorption and the physisorption of A_2 have their intersection below energy zero. This means that, on heating, A_2 would adsorb dissociatively once the increased temperature could supply enough energy to overcome the small barrier (i.e. E_{A2} between the black and blue curves) and that this dissociation would happen at temperatures below desorption. In such a situation the physisorbed state is called a precursor state for chemisorption.
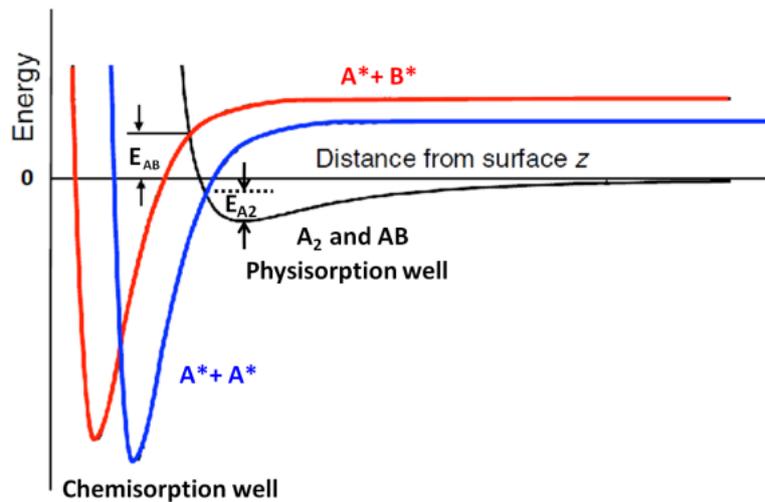
Figure 1. 1 Qualitative sketch (system energy vs. distance from the surface) of chemisorption and physisorption of the molecules A_2 and AB.

For the AB molecule in Figure 1. 1 the intersection of the potential energy surfaces for chemi- and physisorption is above zero, therefore physisorption of AB followed by heating would induce desorption. If we want to adsorb AB from the gas-phase at surface temperatures that are high enough to provide the energy for chemisorption we have to overcome an energy barrier: E_{AB} Figure 1. 1.

In the cartoon model developed in Figure 1. 1 I have discussed the situation of a single molecule (either A_2 or AB) approaching an adsorbate free surface. For many cases of interest, however, we are interested in how molecules adsorb in the presence of other molecules on a surface: the manner in which surface coverage changes the potential energy surfaces in Figure 1. 1. As a practical matter addressing such phenomena requires defining a surface coverage. If all adsorption sites of a surface are saturated by a molecule we talk about one full monolayer. In the following thesis we will often describe adsorbate concentrations in "fraction of a monolayer" (θ). θ is defined:

$$\theta = N_{ads}/N_{max}$$

where N_{ads} is the number of adsorbed molecules at the surface and N_{max} is the total number of adsorption sites on the substrate. After saturation of a monolayer, molecules are adsorbed in a multilayer. Multilayer adsorption of molecules is in general a physisorption process.

For one surface reaction, two parts are involved--the adsorbate and the substrate. The above has discussed the different types of adsorption and described the manner in which they result from interaction between the adsorbate and substrate. Given a system in which the adsorbate species and its concentration are specified, the rate and mechanism of adsorption is a function of the surface structure of the substrate. In the following part, let us start with the introduction on the substrate --α-Al_2O_3−that will be studied in this thesis.

Metal and metal oxide surfaces are everywhere in nature and common in such applications electronics and heterogeneous catalysis [4, 7-9, 11]. Among them α-Al$_2$O$_3$, the most stable crystalline form of alumina, is notable for its variety of applications in industry -- e.g. as a substrate for growth of functional materials, such as thin film semiconductors and carbon materials [12-15], and as a support in heterogeneous catalysis [11, 16-19] – and as a model for more environmentally abundant alumino-silicate materials which often have local structure (alumina octahedra alternating with silica tetrahedra) similar to the alumina [20].

As previously reported [21], the three most thermodynamically stable surfaces of α-Al$_2$O$_3$ are the C(0001), R(1-102) and A(11-20) planes. Interestingly the behavior of the different planes can differ dramatically in application [22-24]. For example, MgO films grown epitaxially on the different surfaces have very different orientations, aligned single walled carbon nanotubes (SWNTs) of similar size grow on the (11-20) and (1-102) while on the (0001) only randomly aligned, larger SWNTs have been observed [22, 23]. These and other similar results suggest that the structure and termination of each surface control subsequent thin film growth. Similarly, for a number of heterogeneous catalysis applications in which α-Al$_2$O$_3$ is a support, several prior authors have found that changing α-Al$_2$O$_3$ surface structure lead to dramatic changes in catalytic activity [17, 25-27].

It is thus clear that understanding the reactivity and performance of α-Al$_2$O$_3$ in various applications requires knowledge of the surface structure and termination. However, determining even the termination is nontrivial as there are multiple possibilities for each plane -- three for the (0001) plane, five for the (1-102) and six for the (11-20) -- and the thermodynamically favorable termination varies with the environment (e.g. the temperature and oxygen pressure) [21] . The most thermodynamically stable surface, α-Al$_2$O$_3$(0001), has been the most studied. Total-energy electronic-structure calculations based on density-functional theory in the generalized-gradient approximation (GGA) [28] revealed the Al-I termination (atomic sequence AlO3AlAlO3-R, see Figure 1.2) has the lowest energy over twenty five orders of magnitude in oxygen pressure (10^{-10}-10^{15} Pa at 1000 K) [21]. By calculating the Gibbs free energy of the α-Al$_2$O$_3$(0001) surface in equilibrium with a realistic environment that contains both oxygen and hydrogen species, it was found only the hydrogen covered oxygen termination was stable: a H3O3AlAl-R surface termination was favored [29]. Experimental techniques have also been applied to investigate the α-Al$_2$O$_3$ (0001) surface structure and termination: the results of a tensor low energy electron diffraction (LEED) study could be rationalized by assuming the surface is terminated by both Al- and O atoms with a ratio of 2:1[30, 31]; however, time-of-flight scattering and recoiling spectrometry (TOF-SARS) demonstrated a Al-I termination of ultrahigh vacuum prepared α-Al$_2$O$_3$(0001) sample [32]. To summarize, despite much previous work, the termination of the (0001) surface, and particularly the manner in which it might change with environments that contain variable amounts of oxygen and hydrogen, is still under debate.
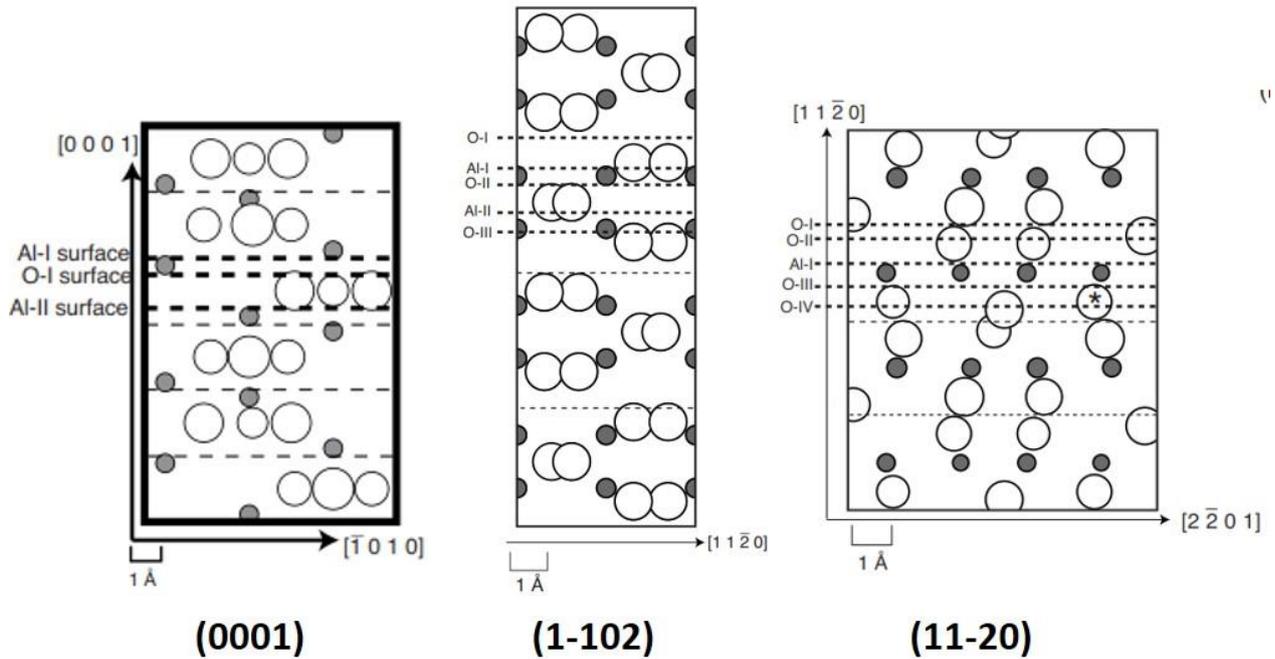
(0001)   **(1-102)**   **(11-20)**

Figure 1. 2 Terminations of α-Al$_2$O$_3$ (0001), (1-102), (11-20) plane, respectively (figure modified from [21]): Oxygen atom in blank large circle, Al atom in small solid circle.

For the second and third most thermodynamically stable surfaces, the α-Al$_2$O$_3$(1-102) plane and α-Al$_2$O$_3$(11-20) plane, surface atomic and electronic structure is substantially less studied. Crystal truncation rod (CTR) diffraction results from the (1-102) plane were interpreted to suggest an oxygen-terminated structure for the stable 1x1 clean surface [33]. Theory calculations are consistent: they find the O-I termination of the (1-102) is the most favorable over a wide range of oxygen chemical potentials [21]. The (11-20) plane annealed in O$_2$ was investigated by high resolution scattering of Helium atoms (HAS) and LEED [34]. The results of this study suggest the ideally terminated (1x1) surface is stable at temperatures below 1200 K and unreactive towards atomic hydrogen. Theoretical study of the detailed atomic structure of this 1x1 (11-20) surface suggests it is the O-I termination and thus that this termination is stable in both oxygen rich and poor environments [21]. To have a clear view and also to better understand the work in this thesis (termination will be mentioned many times in this work), the definition of the terminations of each of the three surfaces are illustrated in Figure 1. 2.

The above discussion reviewed prior work considering the dependence of α-Al$_2$O$_3$ surface termination and structure, for the three most stable surfaces, on change in oxygen, hydrogen and temperature. Because of its ubiquity on the Earth's surface in both the environment and application it is, however, often more important to ask how the presence of *water* affects termination and surface structure. Prior work demonstrates that surface reactivity, polarity and stability of α-Al$_2$O$_3$ all vary dramatically in the presence of even small amounts of water [16, 35, 36]. Thus in this work we start with sub-monolayer water adsorption situations because: i) for many gas phase systems this may be what we actually care

about and ii) we expect the interaction energy of water with alumina surfaces to be dominated by local, pair-wise effects which (if true) implies that the interaction of liquid water with alumina might be usefully thought of as the sum of a large number of, slightly perturbed, single molecule interactions. Therefore a preparation method that permits a controllable amount of water adsorption and a characterization technique that can resolve fractions of a monolayer are required.

If we imagine a simple solid at equilibrium with an atmosphere containing a gas phase adsorbate equilibrium considerations suggest the absolute coverage of the adsorbate on this solid surface will be determined by its, partial, pressure in the gas. Given a background pressure in a chamber of 1 x 10^{-6} mbar one monolayer of gas molecules per second will collide with the surface. Thus if we assume a sticking probability of 1it takes only one second to saturate the surface. In order to minimize this background adsorption effect our investigation must be performed under Ultra High Vacuum (UHV) conditions: a background pressure of $\sim 3 \times 10^{-10}$ mbar (detailed introduction in chapter 2). To dose water under UHV conditions is another challenge since high water pressure will hurt the pump devices and pollute the chamber. Normally to solve this problem people prepare the sample in a preparation chamber with high pressure and then transfer it into UHV. In this work we will deal with this problem in a different way: we apply a supersonic Molecule Beam Source (MBS) with a 3-stage pumping system that maintains a background pressure of $\sim 10^{-9}$ mbar. This MBS, (as we discuss in chapter 2) also enhances the translational kinetic energy water molecules impinging on the surface.

With a UHV chamber and MBS dosing, we are able to realize the preparation of clean α-Al_2O_3 and sub-monolayer water adsorbed samples. As mentioned earlier, the three most thermodynamically stable surfaces of α-Al_2O_3 behave quite differently in industrial applications, presumably because of different surface atomic and electronic structures. In this thesis we explore the adsorption structure of water on α-Al_2O_3 surfaces at low coverages in UHV chamber (chapter 3) and the relationship of increasing water adsorption, as pressure is changed from UHV (10^{-10} bar) to ambient conditions (10^{-2} bar), to changing solid termination (chapter 5 and 6). In addition to these surface structural studies I also address the thermodynamics of water adsorption. Much theoretical work [21, 37-41] has been done on the thermodynamics of water adsorption on α-Al_2O_3 surfaces. However, such studies typically use model chemistries whose accuracy for solid/molecular systems are uncertain [41] and assume a particular mechanism of adsorption. Additionally most prior work focusses on water adsorption process (the rate of dissociative adsorption for example) with little explicit consideration of desorption kinetics and mechanism. To address this issue I study water desorption thermodynamics and kinetics (desorption energy and order) from different surfaces of α-Al_2O_3 in chapter 4.

To experimentally study the structure of adsorbed water on α-Al_2O_3, and the manner in which adsorption changes the underlying solid, we need a tool that can detect dissociated water species and characterize the termination and surface structure of α-Al_2O_3 preferably both in UHV and ambient. Electron-

in/electron-out techniques (e.g., low energy electron diffraction (LEED)[42] and electron energy loss spectroscopy (EELS)) are applicable to characterize well defined crystals in vacuum. They are, however, generally applicable to ambient/metal oxide interface and are also challenging to apply to poorly conductive materials like α-Al$_2$O$_3$ due to surface charging. Scanning Tunneling (STM)[43, 44] or Scanning Probe microscopies (SPM)[45] are applicable to both UHV and ambient conditions, even liquid/solid interfaces, but are not sensitive to Hydrogen and STM cannot be used for bulk insulators, e.g. α-Al$_2$O$_3$ single crystals. X-ray photoelectron spectroscopy (XPS) is a powerful tool for surface science since it is surface sensitive and quantitative (providing both atomic and electronic state information of the surfaces of bulk materials or thin film)[46, 47]. XPS was widely claimed to be hydrogen-undetectable technique until recently this belief is denied by a reporter that it is able to detect H and He atom in gas phase[48]. However, XPS still fails to detect hydrogen that bonded to other atoms like H (or OH) on α-Al$_2$O$_3$ surface and, because it is an electron-out technique, is challenging to apply to solid surfaces in ambient or in contact with liquids. To summarize, most surface characterization approaches are limited to UHV conditions or material with good electrical conductivity or not sensitive to hydrogen.

Sum frequency generation (SFG) [49, 50], a nonlinear second order optical process, is surface specific for materials with inversion symmetry. In SFG two pulsed incident beams are spatially and temporally overlapped and the resulting field at the sum of the frequencies of the two incident beams detected. In this work I employ a scheme with one visible pulse centered at 800 nm that is non-resonant with detected species and one infrared (IR) pulse that is vibrationally resonant. By quantifying the intensity of the emitted sum frequency field as a function of the photon energy of the incident IR beam the SFG process results in an interface-specific vibrational spectroscopy. For a vibrational mode to be SFG active it must be both IR and Raman active. In addition to the interfacial specificity of the signal, this selection rule implies that SFG spectra are often simpler than IR and Raman spectra of the same samples [51]. Due to these attractive characteristics, SFG spectroscopy has been applied to investigate many surfaces and interfaces and played a more and more important role in gaining insight into surface chemistry since its demonstration in 1989 [52]. Of most direct relevance to this work, SFG has been employed to detect OH stretching modes at the air/metal oxide or liquid water/metal oxide interface [53-58] while in our group it has been applied to study water adsorption on α-Al$_2$O$_3$ under UHV and ambient conditions[59, 60]. Additionally it was applied for characterization of surface phonon vibrations of metal oxides like Si-O[51, 61, 62], Ti-O[63] and Al-O[64].

In this thesis, I employ SFG spectroscopy to study water dissociative adsorption on α-Al$_2$O$_3$(11-20) by probing OH (OD) stretching vibrations (chapter 3) and investigate the termination change of α-Al$_2$O$_3$ with increased water pressure by probing the surficial Al-O (H) vibrations in both UHV and ambient conditions (in chapter 5 for the (11-20) surface and chapter 6 for the (0001)). While SFG spectra offer

unique insight into surface structure they offer little insight into the thermodynamics of water adsorption. To address this aspect of the α-Al$_2$O$_3$ water interaction problem I also performed Temperature Programmed Desorption (TPD) measurements of water on all three α-Al$_2$O$_3$ surfaces (chapter 4). The details of both approaches, and additional supporting techniques, are discussed in more detail in Chapter 2.

1.1 References

1.   Winfried, K., et al., Surface Phonons. Springer Series in Surface Science. Vol. 21. 1990, Berlin: Springer.

2.   Adamson, A.W., et al., Physical chemistry of surfaces. 1997, New York: Wiley Interscience Publication, John Wiley & Sons, Inc.

3.   Butler, G.I., H.C.K. , Corrosion and its prevention in waters. 1966, Country unknown/Code not available: 1966.

4.   Fujishima, A., X. Zhang, and D.A. Tryk, TiO$_2$ photocatalysis and related surface phenomena. Surface Science Reports, 2008. **63**(12): p. 515-582.

5.   Diehl, H.W., The theory of boundary critical phenomena. International Journal of Modern Physics B, 1997. **11**(30): p. 3503-3523.

6.   Ullman, W.J., et al., Laboratory evidence for microbially mediated silicate mineral dissolution in nature. Chemical Geology, 1996. **132**(1): p. 11-17.

7.   Banfield, J.F., et al., Biological impact on mineral dissolution: application of the lichen model to understanding mineral weathering in the rhizosphere. Proceedings of the National Academy of Sciences, 1999. **96**(7): p. 3404.

8.   McBride, M.B., et al., Mobility and solubility of toxic metals and nutrients in soil fifteen years after sludge application. Soil Science, 1997. **162**(7): p. 487-500.

9.   Satterfield, C.N., Heterogeneous catalysis in industrial practice. 2nd edition. 1991: New York, NY (United States); McGraw Hill Book Co.; None. Medium: X; Size: Pages: (542 p).

10.   Mills, G., H. Jónsson, and G.K. Schenter, Reversible work transition state theory: application to dissociative adsorption of hydrogen. Surface Science, 1995. **324**(2): p. 305-337.

11.   Ji, L., J. Lin, and H.C. Zeng, Metal−support interactions in Co/Al$_2$O$_3$ catalysts: a comparative study on reactivity of support. The Journal of Physical Chemistry B, 2000. **104**(8): p. 1783-1790.

12.   Amano, H., et al., Metalorganic vapor phase epitaxial growth of a high quality GaN film using an AlN buffer layer. Applied Physics Letters, 1986. **48**.

13.   Harrison, S.E., et al., Two-step growth of high quality Bi$_2$Te$_3$ thin films on α-Al$_2$O$_3$(0001) by molecular beam epitaxy. Applied Physics Letters, 2013. **102**.

14.   Kim, J.H., et al., Growth of heteroepitaxial ZnO thin films on GaN-buffered Al$_2$O$_3$(0001) substrates by low-temperature hydrothermal synthesis at 90 °C. Advanced Functional Materials, 2007. **17**(3): p. 463-471.

15.   Ago, N.I.H., Crystal plane dependent growth of aligned single-walled carbon nanotubes on sapphire. Journal of the American Chemical Society, 2008. **130**(30): p. 9918-9924.

16. Kijlstra, W.S., et al., Inhibiting and deactivating effects of water on the selective catalytic reduction of nitric oxide with ammonia over MnOx/Al2O3. Applied Catalysis B: Environmental, 1996. **7**(3): p. 337-357.

17. Shimada, H., Morphology and orientation of MoS_2 clusters on Al_2O_3 and TiO_2 supports and their effect on catalytic performance. Catalysis Today, 2003. **86**(1): p. 17-29.

18. Nehasil, V., et al., The interaction of carbon monoxide with $Rh/\alpha-Al_2O_3$ model catalysts: influence of the support structure. Surface Science, 1999. **433-435**: p. 215-220.

19. Bolt, P.H., et al., The interaction of thin NiO layers with single crystalline $\alpha-Al_2O_3$(11-20) substrates. Surface Science, 1995. **329**(3): p. 227-240.

20. de Jong, B.H.W.S. and G.E. Brown, Polymerization of silicate and aluminate tetrahedra in glasses, melts, and aqueous solutions—I. Electronic structure of $H_6Si_2O_7$, $H_6AlSiO_7^{1-}$, and $H_6Al_2O_7^{2-}$. Geochimica et Cosmochimica Acta, 1980. **44**(3): p. 491-511.

21. Kurita, T., K. Uchida, and A. Oshiyama, Atomic and electronic structures of $\alpha-Al_2O_3$ surfaces. Physical Review B, 2010. **82**(15).

22. Ishigami, N., et al., Crystal plane dependent growth of aligned single-walled carbon nanotubes on sapphire. Journal of the American Chemical Society, 2008. **130**(30): p. 9918-9924.

23. Stampe, P.A., et al., Growth of MgO thin films on M-, A-, C- and R-plane sapphire by laser ablation. Journal of Physics D: Applied Physics, 1999. **32**(15): p. 1778-1787.

24. Zhang, K.L., et al., Domain matching epitaxial growth of In_2O_3 thin films on $\alpha-Al_2O_3$(0001). Crystal Growth & Design, 2012. **12**(2): p. 1000-1007.

25. Khodakov, A., et al., Structure and catalytic properties of supported Vanadium oxides: support effects on oxidative dehydrogenation reactions. Journal of Catalysis, 1999. **181**: p. 205–216.

26. Ji, L., J. Lin, and H.C. Zeng, Metal−support interactions in Co/Al_2O_3 catalysts: a comparative study on reactivity of support. The Journal of Physical Chemistry B, 2000, 104,. **104**: p. 1783-1790.

27. He, S., et al., Dehydrogenation of long chain paraffins over supported $Pt-Sn-K/Al_2O_3$ catalysts: A study of the alumina support effect. Applied Catalysis A: General, 2009. **356**(1): p. 88-98.

28. Baxter, R., et al., The extent of relaxation of the $\alpha-Al_2O_3$(0001) surface and the reliability of empirical potentials. Surface Science, 2000. **445**(2): p. 448-460.

29. Wang, X.-G.C., Anne; Scheffler, Matthias, Effect of the environment on $\alpha-Al_2O_3$(0001) surface structures. Physical Review Letters, 2000. **84**(16): p. 3650-3653.

30. Toofan, J. and P.R. Watson, The termination of the $\alpha-Al_2O_3$(0001) surface: a LEED crystallography determination. Surface Science, 1998. **401**(2): p. 162-172.

31. Soares, E.A., et al., Structure of the $\alpha-Al_2O_3$(0001) surface from low-energy electron diffraction: Al termination and evidence for anomalously large thermal vibrations. Physical Review B, 2002. **65**(19): p. 195405.

32. Ahn, J. and J.W. Rabalais, Composition and structure of the $\alpha-Al_2O_3$ (0001)-(1 × 1) surface. Surface Science, 1997. **388**(1): p. 121-131.

33. Trainor, T.P., et al., Crystal truncation rod diffraction study of the $\alpha-Al_2O_3$(1-102) surface. Surface Science, 2002. **496**(3): p. 238-250.

34. Becker, T., et al., Microstructure of the $\alpha-Al_2O_3$(11-20)surface. Physical Review B, 2002. **65**(11).

35.   Shapovalov, V. and T.N. Truong, Ab initio study of water adsorption on α-Al$_2$O$_3$(0001) crystal surface. The Journal of Physical Chemistry B, 2000. **104**(42): p. 9859-9863.

36.   Rabung, T., et al., Cm(III) sorption onto sapphire (α-Al$_2$O$_3$) single crystals. The Journal of Physical Chemistry B, 2004. **108**(44): p. 17160-17165.

37.   Hass, K., et al., The chemistry of water on alumina surfaces: reaction dynamics from first principles. Science, 1998. **282**: p. 265-268.

38.   Wirth, J. and P. Saalfrank, The chemistry of water on α-alumina: kinetics and nuclear quantum effects from first principles. The Journal of Physical Chemistry C, 2012. **116**(51): p. 26829-26840.

39.   Wang, B., et al., Density functional/all-electron basis set slab model calculations of the adsorption/dissociation mechanisms of water on α-Al$_2$O$_3$(0001) Surface. The Journal of Physical Chemistry C, 2011. **115**(27): p. 13399-13411.

40.   Heiden, S., et al., Water dissociative adsorption on α-Al$_2$O$_3$(11-20) is controlled by surface site undercoordination, density, and topology. The Journal of Physical Chemistry C, 2018. **122**(12): p. 6573-6584.

41.   Wirth, J., et al., Characterization of water dissociation on α-Al$_2$O$_3$((1-102): theory and experiment. Physical Chemistry Chemical Physics, 2016. **18**(22): p. 14822-32.

42.   Elam, J.W., et al., Adsorption of H$_2$O on a single-crystal α-Al$_2$O$_3$(0001) surface. The Journal of Physical Chemistry B, 1998. **102**.

43.   Binnig, G., et al., Surface Studies by Scanning Tunneling Microscopy. Physical Review Letters, 1982. **49**(1): p. 57-61.

44.   Kliewer, K.L. and R. Fuchs, Optical modes of vibration in an ionic crystal slab including retardation. II. radiative region. Physical Review, 1966. **150**(2): p. 573-588.

45.   Weiss, S., et al., Ultrafast scanning probe microscopy. Applied Physics Letters, 1993. **63**(18): p. 2567-2569.

46.   Trainor, T.P., et al., Crystal truncation rod diffraction study of the α-Al$_2$O$_3$(1-102) surface. Surface Science, 2002. **496**: p. 238-250.

47.   Tanwar, K.S., et al., Surface diffraction study of the hydrated hematite surface. Surface Science, 2007. **601**(2): p. 460-474.

48.   Zhong, J.-Q., et al., Synchrotron-based ambient pressure X-ray photoelectron spectroscopy of hydrogen and helium. Vol. 112. 2018. 091602.

49.   Zhu, X.D., H. Suhr, and Y.R. Shen, Surface vibrational spectroscopy by infrared-visible sum frequency generation. Physical Review B, 1987. **35**(6): p. 3047-3050.

50.   Guyot-Sionnest, P., J.H. Hunt, and Y.R. Shen, Sum-frequency vibrational spectroscopy of a Langmuir film: study of molecular orientation of a two-dimensional system. Physical Review Letters, 1987. **59**(14): p. 1597-1600.

51.   Liu, W.T., et al., Sum-frequency phonon spectroscopy on α-quartz. Physical Review B, 2008. **78**(2): p. 024302-1 -024302-6.

52.   Shen, Y.R., Surface properties probed by second-harmonic and sum-frequency generation Nature, 1989. **337**: p. 519-525.

53. Sung, J., Y.R. Shen, and G.A. Waychunas, The interfacial structure of water/protonated α-Al$_2$O$_3$(11-20) as a function of pH. Journal of Physics: Condensed Matter, 2012. **24**(12): p. 124101.

54. Sung, J., et al., Surface structure of protonated R-sapphire (1-102) studied by sum-frequency vibrational spectroscopy. Journal of the American Chemical Society, 2011. **133**(11): p. 3846-53.

55. Zhang, L., et al., Structures and charging of α-Alumina (0001)/water interfaces studied by sum-frequency vibrational spectroscopy. Journal of the American Chemical Society, 2008. **130**(24): p. 7686-7694.

56. Uosaki, K., T. Yano, and S. Nihonyanagi, Interfacial water structure at As-prepared and UV-induced hydrophilic TiO$_2$ surfaces studied by sum frequency generation spectroscopy and quartz crystal microbalance. The Journal of Physical Chemistry B, 2004. **108**(50): p. 19086-19088.

57. Backus, E.H.G., et al., On the role of Fresnel factors in sum-frequency generation spectroscopy of metal–water and metal-oxide–water interfaces. The Journal of Physical Chemistry C, 2012. **116**(44): p. 23351-23361.

58. Wang, C.-y., H. Groenzin, and M.J. Shultz, Direct observation of competitive adsorption between methanol and water on TiO$_2$: an in situ sum frequency Generation study. Journal of the American Chemical Society, 2004. **126**(26): p. 8094-8095.

59. Kirsch, H., et al., Experimental characterization of unimolecular ater dissociative Adsorption on α-alumina. The Journal of Physical Chemistry C, 2014. **118**(25): p. 13623-13630.

60. Wirth, J., et al., Characterization of water dissociation on α-Al$_2$O$_3$(1-102): theory and experiment. Physical Chemistry Chemical Physics, 2016. **18**(22): p. 14822-32.

61. Liu, W.T., et al., Sum-frequency spectroscopy on bulk and surface phonons of noncentrosymmetric crystals. Annalen der Physik, 2011. **523**(1-2): p. 101-106.

62. Liu, W.T., et al., Surface vibrational modes of α-quartz(0001) probed by sum-frequency spectroscopy. Physical Review Letters, 2008. **101**(1): p. 016101.

63. Cao, Y., et al., Evolution of anatase surface active sites probed by in situ sum-frequency phonon spectroscopy. Science Advances, 2016. **2**(9): p. e1601162.

64. Tong, Y., et al., Optically probing Al-O and O-H vibrations to characterize water adsorption and surface reconstruction on alpha-alumina: an experimental and theoretical study. The Journal of Chemical Physics, 2015. **142**(5): p. 054704.

Chapter 2 Methods and experimental setup

As introduced in chapter 1, in this thesis I will study water adsorption and desorption, and the resulting surface reconstruction, on α-Al$_2$O$_3$ surfaces in both UHV and ambient conditions. In this chapter, I first introduce the experimental setup describing the UHV chamber, sample preparation/ mounting and the laser. I next describe the theoretical background of the optical spectroscopy, i.e. vibrationally resonant sum frequency generation spectroscopy. In part three the approach to analysis of temperature programmed desorption (TPD) spectra is described in detail. The chapter is concluded with a brief introduction to the first principles calculation approach. While these calculations were performed by collaborators, some methodological description is important because the results are employed here to help better understand the experimental observables I have generated.

2.1 Experimental setup

The main part of the work described in this thesis was done in an Ultra High Vacuum (UHV) chamber including: a) prepare the samples; b) to do optical spectroscopy; c) and perform TPD measurement. In the following section the details of this system and the techniques used for sample preparations and characterization are introduced.

2.1.1 UHV chamber

The initial stages of this work were performed on an older UHV system. This system had several shortcomings. Some of them qualitatively effected the data that could be obtained, e.g. the sample mounting in UHV did not allow rotation around the surface normal, while others simply made performing experiments much less efficient, e.g. installation of a new sample required venting of the chamber. In part because of these limitations midway through my thesis a new system was installed. Because the great majority of the data I describe here was collected using this system I focus on its description highlighting differences where appropriate. This 'new' UHV system has a 5 axis manipulator (Figure 2. 1) that allows the sample to be translated in the x, y, and z directions (with x & y in the table surface and z perpendicular) and rotated around the R1 (i.e. around z) and R2 (perpendicular to the sample surface) rotational axes. As shown in Figure 2. 1, the entire system is composed of three chambers: an SFG/analysis chamber for optical and TPD measurements, the UFO for sample transfer and the Pre-chamber which is used for higher pressure applications like sample cleaning.
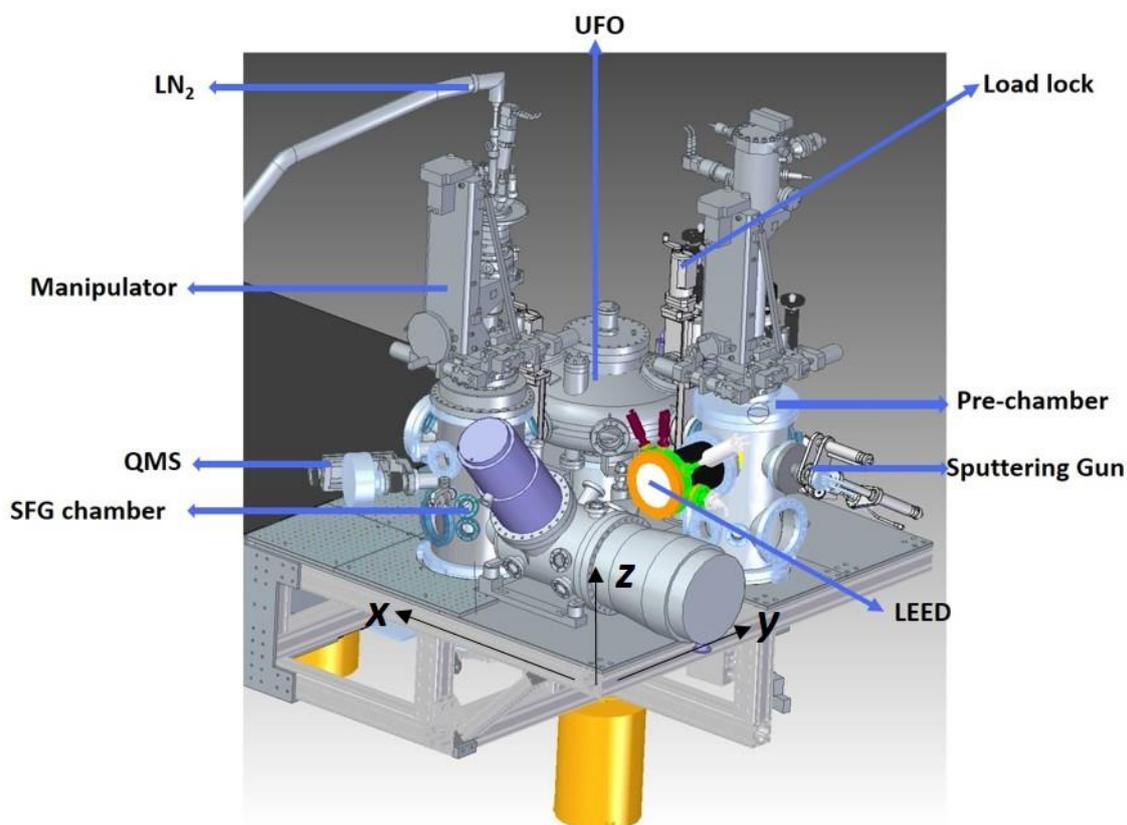
Figure 2. 1 UHV setup and the accessories.

The load lock and UFO chamber make sample transfer in and out of the system without disturbing the vacuum. To prepare a sample for characterization, α-Al_2O_3 crystal is put in the load lock chamber. The load lock is then pumped until the pressure reaches 10^{-10} mbar, transferred to the UFO and delivered to the Pre-chamber. Once in the pre-chamber it is cleaned using the attached sputtering gun and gas source (Ar and O_2) where the sample could be heated and cooled with the same method as for the SFG chamber. Low energy electron diffraction (LEED) and Auger electron spectroscopy (AES) equipment are also mounted on this chamber to confirm the quality of the prepared surface.

By pumping with a scroll pump and turbo pump for the UFO and SFG chambers each can easily reach a base vacuum of 3×10^{-10} mbar after bake out (at 120 ℃ for 24 hours). After preparation and conformation of surface quality in the Pre-chamber the sample is transferred, via the UFO, to the SFG chamber. The combination of manipulator and sample holder allows sample cooling in SFG chamber, via liquid nitrogen, to 85 K. The heating of the sample in this work is realized by electron beam heating (resistance heating is also available) and the temperature of the crystal can reach as high as 1400 K with resolution of 0.5 K under control of both this heating and liquid nitrogen cooling system. To study desorption of water from α-Al_2O_3 with TPD, a linear heating ramp is applied to the adsorbate/substrate system and the desorbed molecules are detected using a quadrupole mass spectrometer (LM500, Spectra) [1] attached to the SFG chamber.
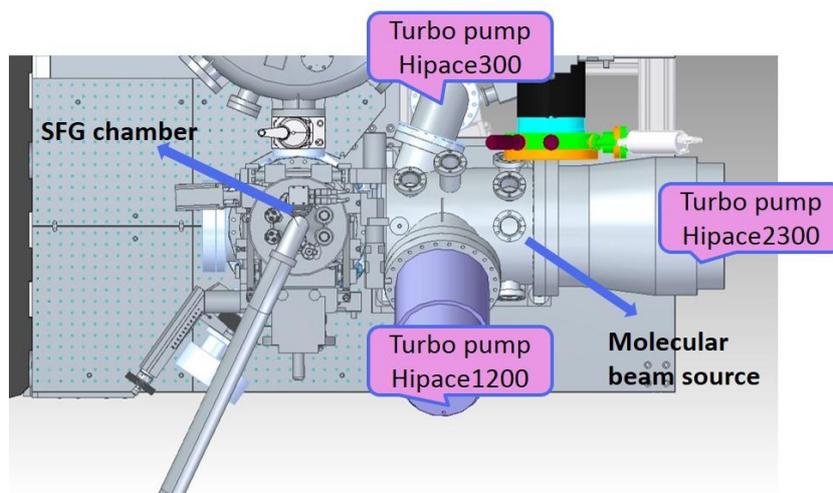
Figure 2. 2 The top view of MBS amounting

To introduce water or other gas sources onto the sample under UHV conditions a three-stage supersonic molecular beam source (MBS) based on previously published designs [2, 3] was set up attached to the SFG chamber. Figure 2. 2 shows the top view of the mounted MBS. As can be seen, it employs three turbo pumps of different sizes to successively decrease the pressure inside the MBS (background pressure 10^{-9} mbar, while dosing it is 10^{-5} mbar) and inhibit SFG chamber poisoning. Compared to pinhole dosing, dosing with MBS enhances the local water pressure near the surface which is expected to increase the dissociative sticking of water in UHV.

2.1.2 Sample mounting and preparation

Figure 2. 3 The structure of sample stage.

The α-Al_2O_3 crystal used in this work is of diameter =15 mm, polished on one side with a roughness < 0.5 nm (MaTeck. Corp) and has a thickness of 1 mm. The as received crystal was first cleaned in an

ultrasonic bath with methanol, acetone and Milli-Q water, each for 15 min. After drying with nitrogen, the crystal was mounted on the sample stage as shown in Figure 2. 3. The crystal is fixed by three clips on a piece of Mo and the temperature of the sample is read out by a thermocouple that is plugged into a hole drilled on the side of the plate. The sample stage is then transferred into the preparation chamber and further cleaned.
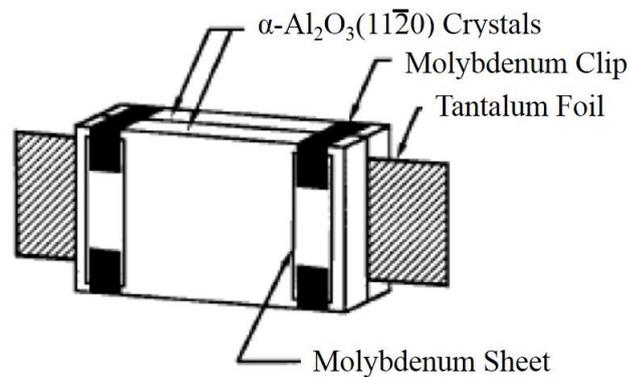

Figure 2. 4 Schematic view of sample mounting of the Al_2O_3 single crystal. The mounting was adopted from previous studies on this subject. Two crystals were clamped around a thin tantalum foil. Figure taken from literature[4] with slightly modification.

While most of the work in this thesis was done with this crystal and the sample stage shown in Figure 2. 3, the work shown in chapter 3 was done with crystals purchased from Princeton Scientific Corp. with a size of $10 \times 15 \times 0.5$ mm polished on one side with a roughness < 0.5 nm. Following previous authors this crystal was mounted by creating a sandwich (Figure 2. 4) of two α-Al_2O_3(11-20) crystals around a 0.01 mm thick piece of tantalum foil[4]. Measurement of the sample temperature (T_{Al2O3}) was achieved by two Chromel/Alumel thermocouples, which were attached to the crystal edges with ceramic glue (Cerabond 605). The thermocouples were connected to a temperature controller (Model 340, Lakeshore) that was connected itself to a power supply for resistive heating. By attaching two thermocouples to the crystal's diagonally opposite edges (e.g. the upper left and lower right) it was ensured that the sample was heated homogeneously (temperature differences in the plane of the sample surface are < 5 K). While this set up allowed sample heating to 1200 and cooling to 130 K the design of the sample holder, and the hardware available in the chamber, allowed only resistive heating. As a result maintaining linear heating ramps at high temperatures (during TPD measurements) was very difficult.

Regardless of the sample mounting, the cleaning of α-Al_2O_3 surfaces was done using the same procedure: the sample was sputtered under 1.0 K eV with an Argon plasma and then annealed to 900 K, 1000 K and 1200 K (for the (0001) surface not higher than 1150 K since prior work has shown that it reconstructs above 1300 K in UHV [4, 5]) for 10 min, respectively, in an O_2 atmosphere. Repeating this cycle 2-3

times results in a carbon free surface (as verified by Auger spectroscopy) that shows a well-defined 1x1 LEED pattern for all the three surfaces -- α-Al$_2$O$_3$(11-20), (1-102) and (0001) -- as presented in Figure 2. 5.
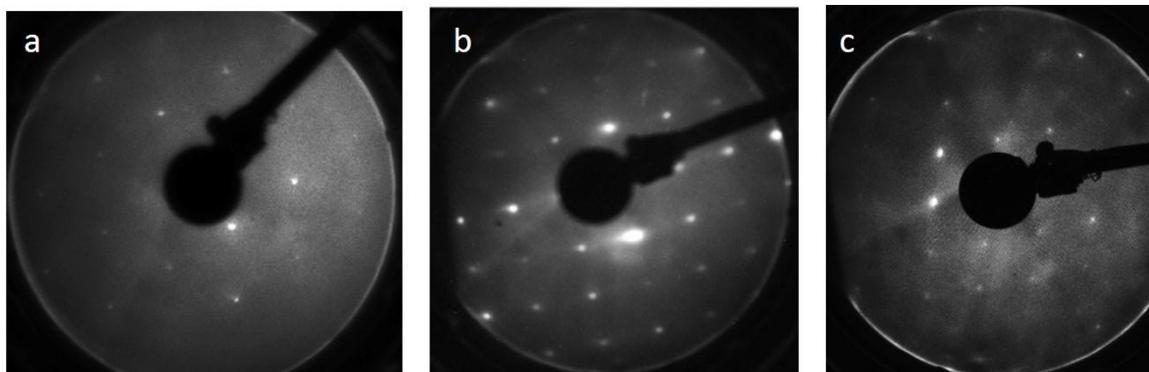

Figure 2. 5 1x1 LEED pattern of (a) α-Al$_2$O$_3$(0001) collected at 158 eV,(b) α-Al$_2$O$_3$ (1-102) collected at 120 eV and (c) α-Al$_2$O$_3$ (11-20) collected at 275 eV.

2.1.3 The Laser setup and SFG measurements

The setup of the laser system for SFG spectroscopy is shown in Figure 2. 6. The process of pulse generation and the full description of the laser itself has been already intensively discussed in previous works[6-12]. The key points of the setup are the generation of the intense ultrashort 800 nm pulses is based on a commercial Ti:sapphire oscillator (Vitesse; Coherent, Inc.), which seeds a regenerative and multipass amplifier (Legend Elite Due HE, Coherent). For pumping the amplifiers we employ two pulsed Nd:YLF lasers from Quatronix.

After amplification, the output pulse reaches its maximum around 800 nm. More than half of the regenerative amplifier output (5 mJ/pulse out of 8 mJ/pulse, 45 fs pulses, 1 kHz, centered at 800 nm) was used to pump an optical parametric amplifier and difference frequency generation unit (TOPAS, Light conversion) to generate tunable broadband-IR pulses (bandwidth 130-150 cm^{-1} (FWHM)) with pulse energies of 10-15 μJ and durations of ≈ 150 fs. The residual 800 nm pulse from the OPA process was used for creation of the 800 nm up-conversion pulse after spectral narrowing by an etalon.

After generation, the IR and spectrally narrowed 800 nm beams (electric field of both are parallel to the laser table) are propagated through a λ/2 plate for polarization control of the two incident beams and suitable lens to focus on the sample surface. Several different incident angle were employed in this thesis for the two beams depending on the system characteristics. For samples in the UHV chamber the possible incident angles are determined by the orientation of windows with respect to the sample holder/manipulator. In this thesis, the geometries for SFG measurements are: incident angles of 70°/75°
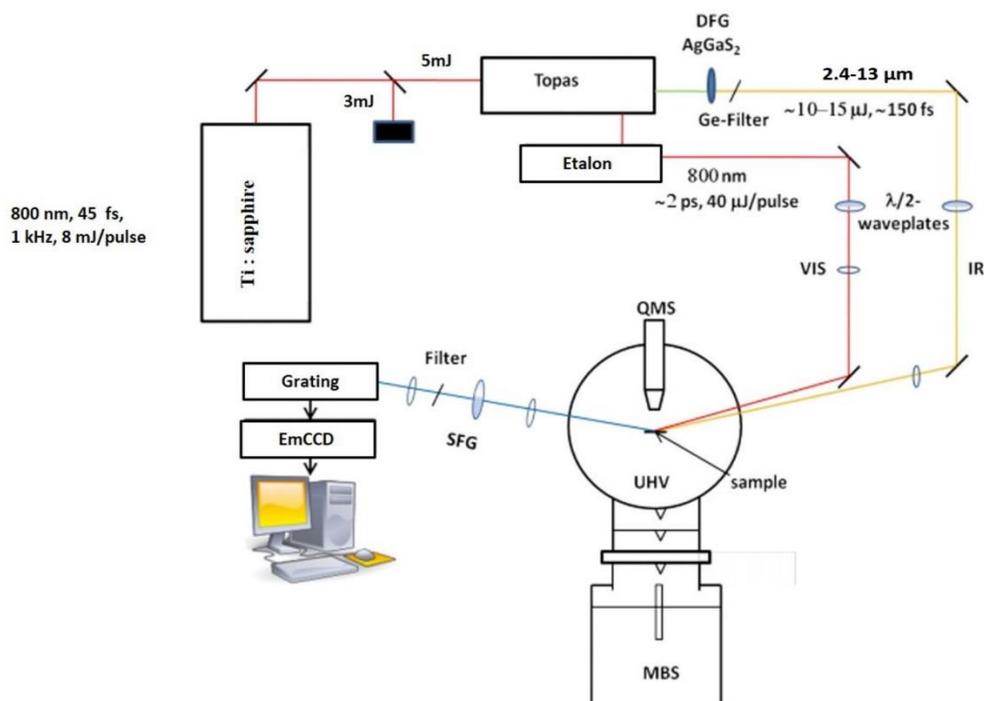
Figure 2. 6 The sketch of the input beam path for SFG generation and signal collection

for IR/Vis relative to the surface normal (probing OD stretching mode in UHV in chapter 3); 54°/61° (probing surface phonon in UHV in chapter 5) and 62°/45° (probing surface phonon in ambient in chapter 5); and in chapter 6 for probing surface phonon of α-Al_2O_3(0001), the incident angles for IR/Vis are 60°/36° in ambient measurement and 54°/61° for the UHV measurements. By adjusting a delay stage (in the path of the IR) and the two mirrors before the chamber in each incident beam path, the incident IR and 800 nm beams are overlapped, spatially and temporally, at the sample surface. As this discussion implicitly suggests, the measured SFG intensity, whether resonant or nonresonant, depends strongly on polarization combination and the experimental geometry. The details of this dependence, and the manner in which they offer insight into interfacial structure, will be discussed below.

Once the SFG signal was generated on the sample in the UHV chamber (or in ambient), the light was collimated, propagated through a polarizer and λ/2 plate and several filters to control polarization and remove the reflected VIS light, focused into a spectrometer and dispersed via one grating of the possible three (1800 g/mm, 1200 g/mm, 900 g/mm) across an emICCD camera (Princeton Instruments).

Calibration is necessary to connect the dispersed signal to wavelength. I did this calibration using a LOT Pen-Ray Ne-lamp with precisely known, extremely narrow, emission lines. To crosscheck, and correct for any misalignment of the detected field propagating into the spectrometer, we also put a polystyrene sample on the IR beam path and calibrate the IR wavelength on the known absorption maxima of polystyrene. Both procedures gave the same IR frequency after calibration.

The experimental spectral resolution of our setup is determined by the bandwidth of our Vis pulse (because of a convolution of the bandwidth of the Vis pulse and the natural bandwidth of the resonance). The spectral resolution was 12 ± 5 cm^{-1} for FWHM (Full width at half maximum) as in this work.

2.2 Sum frequency generation

As discussed in Chapter 1, as a result of the importance of surfaces in a wide variety of biological, environmental and technological systems, many characterization techniques have been developed. However, probing methods based on electrons[4], x-rays[13, 14] or atoms are generally insensitive to hydrogen[15] or are not applicable in ambient atmospheres or at the solid/liquid. A different approach is to probe the surface with photons with energies in the infrared. Here when the photon energy matches the energy difference between energy levels of a molecule's vibrations (or solid lattice oscillations), the interaction between the incident field and the sample is resonant: the excited mode of the molecule or lattice oscillates at much higher amplitude. By detecting the transmitted or reflected light as a function of the frequency of the incident photon energy one obtains the characteristic vibrational modes of the sample. For this work, vibrationally resonant sum frequency generation (SFG) spectroscopy is applied to investigate the water/α-Al$_2$O$_3$ interface. SFG is a surface specific spectroscopy for inversion symmetric materials, is applicable from solid/vacuum to liquid/solid interfaces and is sensitive to hydrogen (bonded to other atoms). This surface specificity avoids the necessity of using exotic sample geometries or the difficulties in signal normalization that typically come when trying to use conventional, bulk-sensitive vibrational spectroscopies, e.g. infrared absorption or spontaneous Raman scattering, to gain insight into surfaces. The theory for SFG including the generation process and how different factors contribute to the intensity of the signal are introduced next.

2.2.1 Linear and Nonlinear Optics

Before discussing the SFG-process, it is useful to start with a general introduction into linear and nonlinear optics[67]. Most of the optical phenomena around us are governed by the interaction of electromagnetic radiation with matter. One way to think of such an interaction is that the applied field induces a polarization in the molecule. In the limit of a relatively weak applied field the induced polarization P is linearly proportional to the amplitude of the applied electric field E of the light.

$$P = P^{(0)} + \varepsilon_0 \chi^{(1)} E \qquad\qquad 2.1$$

$$\chi^{(1)} = N < \alpha > /\varepsilon_0 \qquad\qquad 2.2$$

Where, ε_0 is the vacuum permittivity, $P^{(0)}$ is the static polarization. $\chi^{(1)}$ is the linear susceptibility which is a function of also the dielectric constant of the material ε and is proportional to the number of

molecules per unit volume *N*, and the molecular polarizability averaged over all the orientations of molecules in the material $<\alpha>$.

In an intense electric field, for example, a laser source, the applied electric fields become comparable to the fields felt by an electron in a molecule. In this regime the response of the molecules electron density, i.e. the induced polarization, is no longer linear in the applied field and higher order terms in E must be considered. Writing the induced polarization as a Taylor series gives:

$$P = P^{(0)} + P^{(1)} + P^{(2)} + P^{(3)} + ...$$
$$= P^{(0)} + \varepsilon_0 \left(\chi^{(1)} E + \chi^{(2)} : EE + \chi^{(3)} \vdots EEE + ... \right)$$

2. 3

where $\chi^{(2)}$ and $\chi^{(3)}$ are the second- and third-order nonlinear susceptibilities and $\chi^{(2)}$ is a third-rank and $\chi^{(3)}$ a fourth-rank tensor. These give rise to nonlinear optical effects that are known as second- and third-order nonlinear effects, respectively.

The nonlinear processes that will be extensively studied in this thesis is sum frequency generation (SFG). Assuming two laser beams with electric fields of $E_1 cos(\omega_1 t)$ and $E_2 cos(\omega_2 t)$ are present simultaneously

$$P^{(2)} = \varepsilon_0 \chi^{(2)} : \left(E_1 \cos(\omega_1 t) + E_2 \cos(\omega_2 t) \right)^2$$

2. 4

and generate the second order nonlinear polarization $P^{(2)}$, equation 2. 4 can be further expanded to:

$$P^{(2)} = \frac{1}{2} \varepsilon_0 \chi^{(2)} : \left[E_1^2 \left(1 + \cos(2\omega_1)t \right) + E_1^2 \left(1 + \cos(2\omega_2)t \right) \right]$$
$$+ \varepsilon_0 \chi^{(2)} : E_1 E_2 \left(\cos(\omega_1 + \omega_2)t + \cos(\omega_1 - \omega_2)t \right)$$

2. 5

This equation shows that the polarized media itself acts as a light source and emits at frequencies *2ω₁, 2ω₂, ω₁+ω₂,* and *ω₁-ω₂*: second harmonic generation (SHG) for both input beams, sum frequency generation (SFG), and difference frequency generation (DFG), respectively. Besides, there are also two cases that are not frequency dependence-the optical rectification of the two input fields.

In the SFG process, the frequency of the emitted signal is equal to the sum of the infrared and the visible, as shown in equation 2. 6:

$$\omega_{SFG} = \omega_{vis} + \omega_{IR}$$

2. 6

Furthermore this process follows momentum conservation which is:

$$k_{SFG}\,sin\beta_{SFG} = k_{Vis}\,sin\beta_{Vis} + k_{IR}\,sin\beta_{IR} \qquad\qquad 2.7$$

where β_{SFG}, β_{Vis} and β_{IR} are the angles with respect to the surface normal and k_{SFG}, k_{Vis} and k_{IR} are the wave vectors of each beam. Equation 2. 7 implies that the angle of the emitted SFG light depends on the angle of both incoming beams as well as their frequencies.

Nonlinear media can be divided into two groups depending on their internal symmetry: those that are centro-symmetric, i.e. have inversion symmetry, and those that do not. In case of centro-symmetry the material must have the same property at position x and −x. A look at the $\chi^{(2)}$ for second order processes makes clear what the consequences of inversion symmetry. $\chi^{(2)}$ is a third-rank tensor with 27 components and changes its sign under inversion operation: (equation 2. 8):

$$\chi^{(2)}_{ijk} = -\chi^{(2)}_{-i-j-k} \qquad\qquad 2.8$$

But due to inversion symmetry of the medium $\chi^{(2)}$ must also be insensitive to this transformation as in equation 2. 9: In a medium with inversion symmetry all directions are identical and thus:

$$\chi^{(2)}_{ijk} = \chi^{(2)}_{-i-j-k} \qquad\qquad 2.9$$

Only if $\chi^{(2)} = 0$ are both equations 2. 8 and 2. 9 fulfilled: $\chi^{(2)}$ for media with inversion symmetry is equal to zero. Bulk α-Al_2O_3 is such a media and therefore does not contribute to the detected SFG signal. Terminating any bulk phase, whether an inversion symmetric solid, a liquid or a gas, must break inversion symmetry. As a result for such system $\chi^{(2)} \neq 0$, and SFG is possible, but only from an interface.

2.2.2 SFG generation

Depending on the photon energy of the incident and/or outgoing fields, SFG can be used as an electronic, vibrational or doubly resonant spectroscopy[7, 8]. In this thesis, only vibrationally resonant SFG is employed. In our scheme one incident beam is from the mid-infrared region and interacts resonantly with the sample. The second incident beam has photon wavelengths in the visible (in this work 800 nm) and does not interact resonantly with the material. Similarly, the emitted SFG beam also has wavelengths in the visible and interacts with the sample only nonresonantly. The resulting SFG signal is in the visible and can thus be detected on a sensitive, Si based, CCD detector. In our realization of SFG the two pulsed incident beams are co-propagating and overlap spatially and temporally on the surface of sample while the generated SFG signal is detected in the reflected direction. As shown in Figure 2. 7, the SFG process can be considered as an infrared excitation (red arrow) followed by an anti-Stokes Raman transition (Blue and purple arrows). Therefore, only a vibrational mode that is both IR and Raman active is SFG active. Consequently, SFG spectra collected in this manner are typically simplified compared to IR or Raman spectra[16].
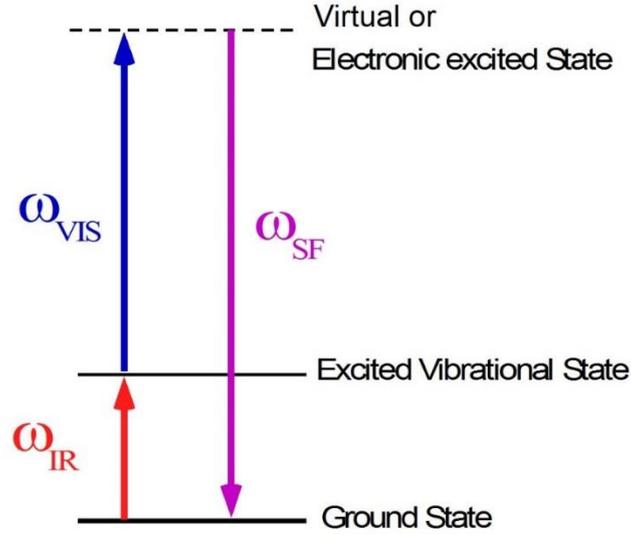
Figure 2. 7 Energy-level diagram that describes sum frequency generation (SFG) process, which can be regarded as an infrared excitation (red arrow) followed by an anti-Stokes Raman transition (Blue and purple arrows).

2.2.3 Fresnel factor

Figure 2. 8 shows a schematic diagram for SFG from an interface between air or water (medium 1) and α-Al_2O_3 (medium 2). The SFG intensity is proportional to the intensities of the incident visible and IR beams and to the squared modulus of the second-order nonlinear susceptibility, $\chi^{(2)}_{ijk}$, of the interface[6].

$$I_{SF}(\omega_{SF}) \propto \left| \sum_i \sum_{j,k} L_{ii}(\omega_{SF}) L_{jj}(\omega_{vis}) L_{kk}(\omega_{ir}) \chi^{(2)}_{ijk} \right|^2 I_{vis} I_{ir} \qquad \text{2. 10}$$

where (i, j, k = x, y, z) are the cartesian coordinates of the interface-fixed reference frame; I_{SF}, I_{vis}, and I_{ir} are the intensities of SFG, visible, and IR beams, respectively. As described before, $\chi^{(2)}_{ijk}$ is the second-order susceptibility of the interface and is a third rank tensor containing 27 elements. L_{ii}, L_{jj} and L_{kk} are termed either Fresnel coefficients or local field factors (L factors). These coefficients are necessary to relate the IR induced polarization to the emitted SFG E field and to take into account phase matching during the SFG process[17]. Obviously, the detected SFG intensity depends not only on the nonlinear material response, i.e. $\chi^{(2)}_{ijk}$, but also on the L factors[16-18].
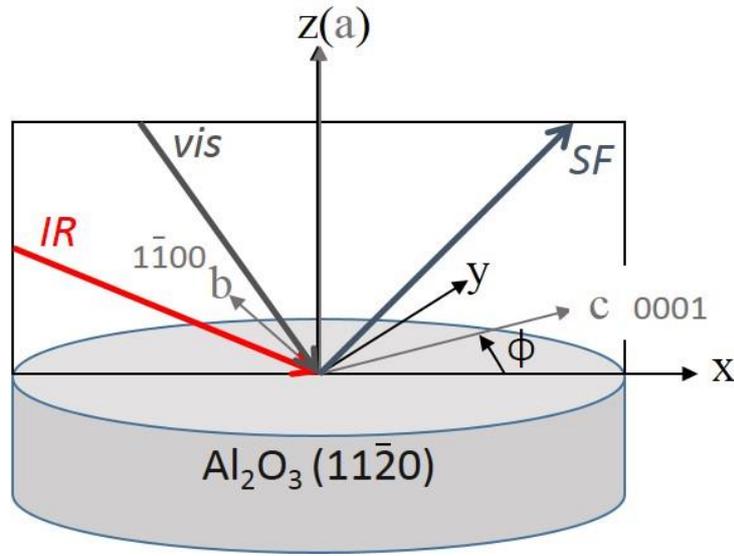
Figure 2. 8 Experimental geometry. All beams are in the x-z plane. SFG spectra were collected at different azimuthal angle (ϕ) which is defined as the angle between the crystal c axis (0001) and the x axis in the lab (rotation in clockwise is positive), z is parallel to (11-20) direction.

For interface between air or vacuum (label as 1) and alumina (label as 2), the L factors in a reflected direction are given by[17] in equation 2. 11,

$$L_{xx}(\omega) = \frac{2n_1(\omega)\cos\gamma}{n_1(\omega)\cos\gamma + n_2(\omega)\cos\beta}$$

$$L_{yy}(\omega) = \frac{2n_1(\omega)\cos\beta}{n_1(\omega)\cos\beta + n_2(\omega)\cos\gamma}$$

$$L_{zz}(\omega) = \frac{2n_1(\omega)\cos\beta}{n_1(\omega)\cos\gamma + n_2(\omega)\cos\beta}\left(\frac{n_1(\omega)}{n'(\omega)}\right)^2$$

2. 11

where ω is the beam frequency, n_1 and n_2 are the refractive index of light with frequency ω in phase 1 and 2 and n′ is the refractive index of that at the interface which can be expressed in terms of n_1 and n_2:

$$n' = n^2\sqrt{\frac{n_2^2 + 5n_1^2}{4n_2^2 + 2n_1^2}}$$

2. 12

β is the incident angle while γ is the refraction angle, and can be obtained by $n_1(\omega)\sin\beta = n_2(\omega)\sin\gamma$. However α-Al$_2O_3$ is birefringent crystal (see Figure 2. 9): the refractive index n depends on the polarization and propagation direction of light. When the polarization (or electric field E) of light is perpendicular to the optical axis c, the transmission is governed by ordinary refractive index value n_o; while it is governed by extraordinary refractive index n_e if the polarization direction is parallel to the c

axis. Thus the calculation of L factors for SFG from alumina surfaces requires consideration of the effects of crystal anisotropy.
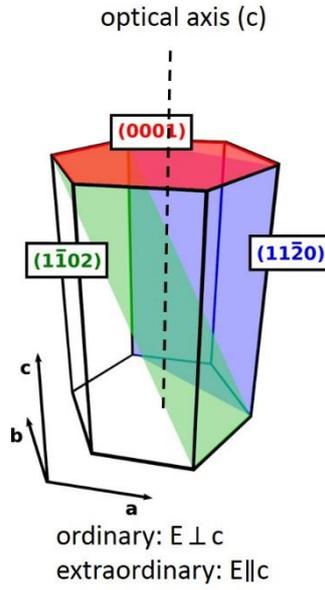
Figure 2. 9 Optical axis c and the definition of ordinary/extraordinary ray: electric field E ⊥ c is defined as ordinary ray; E ∥ c is extraordinary ray as in α-Al2O3.

i.   L on α-Al$_2$O$_3$(11-20)

Here as shown in Figure 2. 8, we define $\phi = 0°$ when the (0001) direction is parallel to the x axis in the lab. Then the Fresnel factor L can be calculated by[18, 19]:

$$L_{xx} = \frac{2k_{2z,e}}{\epsilon_\parallel \, k_{0z} + k_{2z,e}} \qquad \text{2. 13}$$

$$L_{yy} = \frac{2k_{0z}}{k_{0z} + k_{2z,o}}$$

$$L_{zz} = \frac{\epsilon_\parallel}{\epsilon_\perp} \frac{2k_{0z}}{\epsilon_\parallel \, k_{0z} + k_{2z,e}}$$

with $k_{2z,o(e)}$ the z component of the wave vectors of ordinary(extraordinary) waves inside the crystal α-Al$_2$O$_3$ while k_{0z} is the wave vector in air; $\epsilon_{\parallel(\perp)}$ is the dielectric function for electric field vectors parallel (perpendicular) to the c axis[18, 19]:

$$k_{2z,o} = \frac{2\pi\omega}{c_0}\sqrt{\epsilon_\perp - \sin^2\beta}$$

$$k_{2z,e} = \frac{2\pi\omega}{c_0}\sqrt{\epsilon_\parallel - \frac{\epsilon_\parallel}{\epsilon_\perp}\sin^2\beta}$$

2. 14

At position $\phi = 90°$ (as shown in Figure 2. 8, rotate the sample in clockwise direction by 90 degree), L is expressed by[18, 19]:

$$L_{xx} = \frac{2k_{2z,o}}{\epsilon_\perp k_{0z} + k_{2z,o}}$$

$$L_{yy} = \frac{2k_{0z}}{k_{0z} + k_{2z,e}}$$

$$L_{zz} = \frac{2k_{0z}}{\epsilon_\perp k_{0z} + k_{2z,o}}$$

2. 15

while the wave vectors can be calculated:

$$k_{2z,o} = \frac{2\pi\omega}{c_0}\sqrt{\epsilon_\perp - \sin^2\beta}$$

$$k_{2z,e} = \frac{2\pi\omega}{c_0}\sqrt{\epsilon_\parallel - \sin^2\beta}$$

2. 16

The effective second order nonlinear susceptibility is dependent on the polarization of both SFG signal and input beams. In this work, p polarization is defined as wave electric field parallel to the incident plane while s polarization is when the electric field is perpendicular to the incident plane. For α-Al$_2$O$_3$ (11-20), our work in chapter 5 will suggest its surface optical response (SFG of surface phonons) has C$_{2v}$ symmetry. For such a surface there are 13 nonvanishing elements of $\chi^{(2)}$ [11, 20] :

χ_{cab} , χ_{cba}, χ_{cca}, χ_{cac}, χ_{aaa}, χ_{bab}, χ_{abb}, χ_{bba}, χ_{acb}, χ_{abc}, χ_{bca}, χ_{bac} and χ_{acc}

where a, b, c are the crystal axes.

Under different polarization combinations, $\chi^{(2)}$ would be contributed by different combinations of the above. Given this sample symmetry, an experimental geometry (beam incident angles and polarizations) and the corresponding L factors one can write a $\chi^{(2)}_{eff}$ (effective second order non-linear susceptibility)

for each measurement condition. The $\chi^{(2)}_{eff}$ under ssp (SFG/Vis/IR) and ppp (SFG/Vis/IR) polarization combinations for the (11-20) surface can be written [16, 20, 21] (equation 2. 17 and equation 2. 18):

$$\chi^{(2)}_{eff,ssp} = \sin\beta_{ir}\, L_{yy}(\omega_{SF})L_{yy}(\omega_{vis})L_{zz}(\omega_{ir})\,(\chi_{bba}\cos^2\phi + \chi_{cca}\sin^2\phi\,)$$

$$-\sin\beta_{ir}\,L_{yy}(\omega_{SF})L_{yy}(\omega_{vis})L_{zz}(\omega_{ir})(\chi_{cba}\cos\phi\sin\phi + \chi_{bca}\sin\phi\cos\phi\,)$$

2. 17

$$\begin{aligned}\chi^{(2)}_{eff,ppp} = &-\cos\beta_{SF}\cos\beta_{vis}\sin\beta_{ir}\,L_{xx}(\omega_{SF})L_{xx}(\omega_{vis})L_{zz}(\omega_{ir})\,(\chi_{cca}\cos^2\phi\\ &+ \chi_{bba}\sin^2\phi - \chi_{cba}\cos\phi\sin\phi - \chi_{bca}\sin\phi\cos\phi\,)\\ &+ \sin\beta_{SF}\cos\beta_{vis}\cos\beta_{ir}L_{zz}(\omega_{SF})L_{xx}(\omega_{vis})L_{xx}(\omega_{ir})(\chi_{acc}\cos^2\phi\\ &+ \chi_{abb}\,\sin^2\phi - \chi_{acb}\cos\phi\sin\phi - \chi_{abc}\sin\phi\cos\phi)\\ &- \cos\beta_{SF}\sin\beta_{vis}\cos\beta_{ir}L_{xx}(\omega_{SF})L_{zz}(\omega_{vis})L_{xx}(\omega_{ir})(\chi_{cac}\cos^2\phi\\ &+ \chi_{bab}\,\sin^2\phi - \chi_{cab}\cos\phi\sin\phi - \chi_{abc}\sin\phi\cos\phi)\end{aligned}$$

2. 18

$$+\sin\beta_{SF}\sin\beta_{vis}\sin\beta_{ir}L_{zz}(\omega_{SF})L_{zz}(\omega_{vis})L_{zz}(\omega_{ir})\chi_{aaa}$$

Where β_x is the incident angle of beam x (with respect to the surface normal) and ϕ is the azimuthal angle as defined above.

In this work, I will focus on SFG spectra that were collected at this two extreme positions $\phi=0°$ and $\phi=90°$ to simplify the calculations of L for 2-fold surface symmetry of α-Al$_2$O$_3$(11-20). While it is in principle possible to calculate L as a function of azimuthal angle using a transform matrix approach doing so is beyond the scope of this thesis.

ii.   L on α-Al₂O₃(0001)

On the c-cut (0001) plane, for the hydroxylated α-Al$_2$O$_3$ (0001) surface prepared in ambient conditions, a 3-fold symmetry with respect to the azimuthal angle ϕ was identified by our previous SFG study [22]. The non-vanishing components of $\chi^{(2)}$ on such a surface are[11]:

$$\chi^{(2)}_{aac} = \chi^{(2)}_{bbc}$$

$$\chi^{(2)}_{ccc}$$

$$\chi^{(2)}_{aaa} = -\chi^{(2)}_{abb} = -\chi^{(2)}_{bba} = -\chi^{(2)}_{bab}$$

$$\chi^{(2)}_{aca} = \chi^{(2)}_{bcb}$$

$$\chi_{caa}^{(2)} = \chi_{cbb}^{(2)}$$

The effective second order nonlinear susceptibility $\chi^{(2)}_{eff}$ for this C_{3v} surface is given in equation 2. 19 for ssp and equation 2. 20 for ppp polarizations [22, 23].

$$\chi_{eff,ssp}^{(2)} = L_{yy}(\omega_{SF})L_{yy}(\omega_{vis})L_{zz}(\omega_{ir})\sin\beta_{ir}\chi_{yyz}^{(2)}$$
$$+ L_{yy}(\omega_{SF})L_{yy}(\omega_{vis})L_{xx}(\omega_{ir})\cos\beta_{ir}\chi_{yyx}^{(2)}$$

$$= L_{yy}(\omega_{SF})L_{yy}(\omega_{vis})L_{zz}(\omega_{ir})\sin\beta_{ir}\chi_{aac}^{(2)}$$
$$- L_{yy}(\omega_{SF})L_{yy}(\omega_{vis})L_{xx}(\omega_{ir})\cos\beta_{ir}\chi_{aaa}^{(2)}\cos3\phi$$

2. 19

$$\chi_{eff,ppp}^{(2)} = -L_{xx}(\omega_{SF})L_{xx}(\omega_{vis})L_{zz}(\omega_{ir})\cos\beta_{SF}\cos\beta_{vis}\sin\beta_{ir}\chi_{xxz}^{(2)}$$
$$- L_{xx}(\omega_{SF})L_{xx}(\omega_{vis})L_{xx}(\omega_{ir})\cos\beta_{SF}\cos\beta_{vis}\cos\beta_{ir}\chi_{xxx}^{(2)}$$
$$- L_{xx}(\omega_{SF})L_{zz}(\omega_{vis})L_{xx}(\omega_{ir})\cos\beta_{SF}\sin\beta_{vis}\cos\beta_{ir}\chi_{xzx}^{(2)}$$
$$+ L_{zz}(\omega_{SF})L_{xx}(\omega_{vis})L_{xx}(\omega_{ir})\sin\beta_{SF}\cos\beta_{vis}\cos\beta_{ir}\chi_{zxx}^{(2)}$$
$$+ L_{zz}(\omega_{SF})L_{zz}(\omega_{vis})L_{zz}(\omega_{ir})\sin\beta_{SF}\sin\beta_{vis}\sin\beta_{ir}\chi_{zzz}^{(2)}$$

$$= -L_{xx}(\omega_{SF})L_{xx}(\omega_{vis})L_{zz}(\omega_{ir})\cos\beta_{SF}\cos\beta_{vis}\sin\beta_{ir}\chi_{aac}^{(2)}$$
$$- L_{xx}(\omega_{SF})L_{xx}(\omega_{vis})L_{xx}(\omega_{ir})\cos\beta_{SF}\cos\beta_{vis}\cos\beta_{ir}\chi_{aaa}^{(2)}\cos3\phi$$
$$- L_{xx}(\omega_{SF})L_{zz}(\omega_{vis})L_{xx}(\omega_{ir})\cos\beta_{SF}\sin\beta_{vis}\cos\beta_{ir}\chi_{aca}^{(2)}$$
$$+ L_{zz}(\omega_{SF})L_{xx}(\omega_{vis})L_{xx}(\omega_{ir})\sin\beta_{SF}\cos\beta_{vis}\cos\beta_{ir}\chi_{caa}^{(2)}$$
$$+ L_{zz}(\omega_{SF})L_{zz}(\omega_{vis})L_{zz}(\omega_{ir})\sin\beta_{SF}\sin\beta_{vis}\sin\beta_{ir}\chi_{ccc}^{(2)}$$

2. 20

$$\approx -L_{xx}(\omega_{SF})L_{xx}(\omega_{vis})L_{zz}(\omega_{ir})\cos\beta_{SF}\cos\beta_{vis}\sin\beta_{ir}\chi_{aac}^{(2)}$$
$$- L_{xx}(\omega_{SF})L_{xx}(\omega_{vis})L_{xx}(\omega_{ir})\cos\beta_{SF}\cos\beta_{vis}\cos\beta_{ir}\chi_{aaa}^{(2)}\cos3\phi$$
$$+ L_{zz}(\omega_{SF})L_{zz}(\omega_{vis})L_{zz}(\omega_{ir})\sin\beta_{SF}\sin\beta_{vis}\sin\beta_{ir}\chi_{ccc}^{(2)}$$

Since $\chi^{(2)}_{caa} \approx \chi^{(2)}_{aca}$ (in our measurement the frequency of SFG signal is near to that of visible and both are nonresonant) due to intrinsic displacement symmetry[24], and the Fresnel factor for these two components have similar values but opposite signs, the contribution of these two components could be canceled. That is the reason why we do an approximation in equation 2. 20.

For the UHV prepared (0001) sample, as we will discuss in chapter 6, the surface optical response has $C_{\infty v}$ symmetry (SFG response is azimuthal angle independent). Under this condition x(or a) and y (or b) in the laboratory frame are equivalent and the non-vanishing components of the $\chi^{(2)}$ are:

$$\chi^{(2)}_{aac} = \chi^{(2)}_{bbc}$$

$$\chi^{(2)}_{aca} = \chi^{(2)}_{caa} = \chi^{(2)}_{bcb} = \chi^{(2)}_{cbb}$$

$$\chi^{(2)}_{ccc}$$

As we discussed in the above, since the Fresnel factor part of the two components $\chi^{(2)}_{aca} \approx \chi^{(2)}_{caa}$ has similar values but opposite sign[24], $\chi^{(2)}{}_{eff}$ under ppp polarization for $C_{\infty v}$ symmetry simplifies to the expression in equation 2. 21:

$$
\begin{aligned}
\chi^{(2)}_{eff,ppp} = &-L_{xx}(\omega_{SF})L_{xx}(\omega_{vis})L_{zz}(\omega_{ir})\cos\beta_{SF}\cos\beta_{vis}\sin\beta_{ir}\chi^{(2)}_{aac} \\
&-L_{xx}(\omega_{SF})L_{zz}(\omega_{vis})L_{xx}(\omega_{ir})\cos\beta_{SF}\sin\beta_{vis}\cos\beta_{ir}\chi^{(2)}_{aca} \\
&+L_{zz}(\omega_{SF})L_{xx}(\omega_{vis})L_{xx}(\omega_{ir})\sin\beta_{SF}\cos\beta_{vis}\cos\beta_{ir}\chi^{(2)}_{caa} \\
&+L_{zz}(\omega_{SF})L_{zz}(\omega_{vis})L_{zz}(\omega_{ir})\sin\beta_{SF}\sin\beta_{vis}\sin\beta_{ir}\chi^{(2)}_{ccc}
\end{aligned}
\qquad \text{2. 21}
$$

$$
\begin{aligned}
\approx &-L_{xx}(\omega_{SF})L_{xx}(\omega_{vis})L_{zz}(\omega_{ir})\cos\beta_{SF}\cos\beta_{vis}\sin\beta_{ir}\chi^{(2)}_{aac} + \\
&L_{zz}(\omega_{SF})L_{zz}(\omega_{vis})L_{zz}(\omega_{ir})\sin\beta_{SF}\sin\beta_{vis}\sin\beta_{ir}\chi^{(2)}_{ccc}
\end{aligned}
$$

The effects of crystal birefringence on the Fresnel factors for the α-Al$_2$O$_3$(0001) surface can be expressed with equation 2.22 which is not dependent on azimuthal angle:

$$L_{xx} = \frac{2k_{2z,e}}{\epsilon_{\perp}\,k_{0z} + k_{2z,e}}$$

$$L_{yy} = \frac{2k_{0z}}{k_{0z} + k_{2z,o}} \qquad \text{2. 22}$$

$$L_{zz} = \frac{\epsilon_{\perp}}{\epsilon_{\parallel}}\frac{2k_{0z}}{\epsilon_{\perp}\,k_{0z} + k_{2z,e}}$$

While the wave vectors can be obtained from equation 2. 23:

$$k_{2z,o} = \frac{2\pi\omega}{c_0}\sqrt{\epsilon_{\perp} - \sin^2\beta} \qquad \text{2. 23}$$

$$k_{2z,e} = \frac{2\pi\omega}{c_0} \sqrt{\epsilon_\perp - \frac{\epsilon_\perp}{\epsilon_\parallel} \sin^2 \beta}$$

With Fresnel factor corrected measured SFG intensities, we can model the experimental SFG data as a function of $\chi^{(2)}_{ijk}$, in which the nonlinear susceptibility can be described as a coherent superposition of a non-resonant background and Lorentzian resonance(s) as in equation 2. 24:

$$\chi^{(2)}_{ijk} = \chi^{(2)}_{nr} + \chi^{(2)}_r$$

$$= |A_{nr}|e^{i\theta} + \sum_q \frac{|A_q|e^{i\theta_q}}{\omega_{IR} - \omega_q + i\Gamma}$$

2. 24

with the non-resonant contribution being denoted by the amplitude $|A_{nr}|$ and phase **θ**, and the resonant contribution assumed to be capable of being approximated by discrete vibrational resonances with amplitude $|A_q|$, phase θ_q, resonant frequencies ω_q and line width Γ. To actually analyze the data we followed our prior work [22], that we substitute L factor into χ_{eff} and fit the measured SFG spectrum using the Levenberg-Marquardt algorithm as implemented in the commercial visualization and analysis program Igor Pro (Wavemetrics). Because I typically wish to describe a *series* of samples, e.g. as a function of water coverage or azimuthal angle, in which some of the line shape parameters are constant, most data analysis is generally a fit of multiple data sets simultaneously. The experimental results, fitting of the line shape model and the resulting uncertainty in this approach will be discussed in Chapter 3, Chapter 5 and Chapter 6 for specific data sets.

2.2.4 SFG dependence on molecular orientation

In the above part, we discussed the expressions of SFG intensity with Local Fresnel factors for different symmetry surface systems with different polarization combinations. Factors that influent the signal intensity include molecular orientation and incident angles of both visible and IR beam (as shown in previous equations of $\chi^{(2)}_{eff}$). In the following part, we will briefly introduce how these factors influent the SFG intensity.

We will describe the following math with focus on the example of water (D_2O) on the α-Al_2O_3/vacuum interface because this is the system where this formalism is relevant for the study in this thesis.

For this case the emitted sum frequency field can be given by the Maxwell's equation 2. 8 which has been mentioned earlier. In the laboratory frame $\chi^{(2)}_{ijk}$ can be connected to the hyperpolarizability $\beta^{(2)}_{lmn}$ of the molecule. The orientational averaging of molecules or groups is responsible for SFG intensity: because of the breaking of inversion symmetry at the interface the molecules or groups that contribute

to the signal must have some preferential orientation in the laboratory coordinate system. In case of a slow-motion approximation (i.e. the angle of individual molecular groups with respect to the surface normal (θ) does not change on the timescale of the inverse line width) the resulting relationship of the macroscopic $\chi^{(2)}_{ijk}$ to the molecular $\beta^{(2)}_{lmn}$ can be given:

$$\chi^{(2)}_{ijk} = \frac{1}{2\epsilon_0} N_s < R_{il}R_{jm}R_{kn} > \beta^{(2)}_{lmn}$$

$$2.\,25$$

in which $R_{il,}$ $R_{jm,}$ R_{kn} is the ensemble averaged transformation matrix between molecular and laboratory coordinates[12, 25].

For OH or OD stretching vibration from the (11-20) surface (chapter 3) the SFG response has $C_{\infty v}$ symmetry, and calculating the $<R_{il}R_{jm}R_{kn}>$ matrix for each of the relevant $\chi^{(2)}_{ijk}$ terms gives,

$$\chi^{(2)}_{xxz} = \chi^{(2)}_{yyz} = \frac{1}{2\epsilon_0} N_s \chi^{(2)}_{nnn}[< \sin^2\theta\cos\theta > (1-r) + 2r < \cos\theta >]$$

$$\chi^{(2)}_{xzx} = \chi^{(2)}_{zxx} = \frac{1}{2\epsilon_0} N_s \chi^{(2)}_{nnn}[(< \cos\theta > - < \cos^3\theta >)(1-r)]$$

$$2.\,26$$

$$\chi^{(2)}_{zzz} = \frac{1}{\epsilon_0} N_s \chi^{(2)}_{nnn}[r < \cos\theta > + < \cos^3\theta > (1-r)]$$

In this case for free OH/OD, n is parallel to the OH/OD stretching direction while l,m are perpendicular [26]. N_s is the molecule number in the laser spot, θ is the angle of the molecule with respect to the surface normal, and r is the hyperpolarizability ratio ($r = \beta^{(2)}_{lln}/ \beta^{(2)}_{nnn}$). With this information we are able to predict in case of known molecular orientations the dependence of the relative SFG intensity on the experimental geometry and polarization.

2.3 Temperature programmed desorption

As showed in Figure 1. 3, to desorb molecules from a surface energy must be put into the system that exceeds the adsorption energy. Temperature programmed desorption (TPD), is a popular spectroscopic method where desorption of molecules from a given surface as a function of surface temperature is monitored [27, 28]. In this work, it will be employed to study water desorption from α-Al_2O_3. The heating of the sample is realized by Heat-3 device from Prevac company which is capable of electron bombardment heating with a linear heating rate to relatively high temperatures and high-resolution temperature readout.

2.3.1 The theory of TPD spectroscopy

During a TPD measurement one measures the increase in pressure in a vacuum chamber as a function of sample temperature. To most straightforwardly interpret this quantity in terms of the surface properties of the sample such measurements are typically performed in a regime where the pumping speed of the UHV setup is large relative to the partial pressure increase due to desorption and thus the measured partial pressure is proportional to the desorption rate. This can be illustrated by the calculation below.

We assume that a chamber of volume V has a pumping rate S, molecules on the chamber surface desorb with rate L, molecules in the chamber in vacuum have a density of c_g and the sample has a surface area of A_s, from which molecules desorb with desorption rate r(t). During the TPD measurement the temperature of the sample can be expressed,

$$T(t) = T_0 + \beta \cdot t$$

2. 27

T(t) is the sample temperature and β the heating rate while T_0 is the temperature of the sample before heating. The change of number of molecules in the gas phase is given by equation 2. 28:

$$V \frac{d\Delta c_g}{dt} = A_s \bullet r(t) + L - c_g \bullet S$$

2. 28

We can assume that S and L are constants, since there is no heating of the chamber. Then we will get:

$$V \frac{d\Delta c_g}{dt} = L - c_g \cdot S$$

2. 29

For the system in steady-state the solution is therefore $c_g = L/S$. This leads to a pressure in case of no desorption from the sample of p_s:

$$p_s = k_B \cdot T(t) \cdot c_g = k_B \cdot T(t) \cdot L/S$$

2. 30

A pressure change by desorption of molecules from the sample can be described as $\Delta p(t) = p - p_s$. The relationship between pressure change and desorption-rate can thus be written as in equation 2. 31:

$$V \frac{\Delta p}{\Delta t} + S \cdot \Delta p(t) = k_B T(t) A_s r(t)$$

2. 31

In case of high pumping speed, $S \cdot \Delta t \gg V$ (the SFG chamber volume), the first term on the left side can be neglected and we get for the pressure change

$$\Delta p(t) \approx \frac{k_B T A_s}{S} r(t)$$

2. 32

Thus if pumping rate is large relative to the pressure change during desorption, it can be estimated that changes in the pressure are directly proportional to the desorption rate.

2.3.2 TPD data simulation

For investigation of desorption, we monitor the time dependent change of coverage (θ): the desorption rate r(t):

$$r(t) = -d\theta/dt \qquad\qquad 2.\,33$$

In case of an n-order desorption process, we get

$$-d\theta/dt = -k \cdot \theta^n \qquad\qquad 2.\,34$$

k is thereby the rate constant and n the kinetic order of desorption. Generally, molecular desorption has desorption order of one, molecular desorption of multilayer adsorbates an order of zero and recombinative desorption, in which two dissociated species recombine into one, an order of two. Many definitions of the rate-constant have been offered at the end of the 19th century to describe the kinetics of molecular processes: e.g. the Arrhenius expression, the Harcourt-Esson equation and the Kooij equation[29]. By the beginning of the 20th century the only one-parameter equation still in use was the Arrhenius. This formula originates from kinetic theory and connects the rate-constant quantitatively to the temperature [30]:

$$k = \nu(\theta) \cdot e^{-\left(\frac{E_r}{RT}\right)} \qquad\qquad 2.\,35$$

In this equation $\nu(\theta)$ is the pre-exponential frequency factor. From a molecular level view it is the number of attempts per second of an adsorbed molecule to desorb from the surface. While the pre-exponential factor could, in principle, be a function of surface coverage, most studies find it in the range of 10^{13} Hz over a wide range of coverages, i.e. the frequency of the lattice vibration of a solid [31]. In the argument of the exponential $E(\theta)$ is the activation energy of desorption process and R the gas-constant. With this we can describe the desorption rate[32] with equation 2. 36: the Polanyi-Wigner equation:

$$r(t) = \frac{\nu}{\beta}\theta^n \exp^{(-E(\theta)/RT)} \qquad\qquad 2.\,36$$

In this work ν is taken as independent of surface coverage both because maximum initial surface coverages are low (below 0.1 ML) and, thus, differences between the initial coverages also low. β(K·s^{-1}) is the heating rate for the TPD measurement, θ the coverage of adsorbate, n the kinetic desorption order, $E(\theta)$ the desorption energy, taken to be a function of coverage, and R the gas constant. As will be discussed in detail in Chapter 4, a desorption energy E that is independent of the surface coverage is inconsistent with measured curve shapes and cannot fit the data unless one assumes surface structural heterogeneity inconsistent with our well-defined LEED patterns. The simplest possible expression for the coverage dependence of the desorption energy consistent with our data is:

$$E(\theta) = E_0 - c \cdot \theta \qquad\qquad\qquad 2.\,37$$

where E_0 is desorption energy in the low coverage limit – i.e. the unimolecular desorption energy of water -- and c is an empirical constant. The assumed linear increase in E with decreasing θ is equivalent to assuming a pair-wise repulsive interaction between adsorbate species [32-34]. Such a pairwise repulsion is expected for water dissociatively adsorbed on α-Al_2O_3: all the adsorbate species are surface bound Al-OH.

There are several popular methods for TPD data simulation in prior work: Redhead's peak maximum method[35], Chan-Aris-Weinberg method[36] and the leading edge analysis[37]. Redhead's peak maximum method provides a way to easily get desorption energy E_d from even a single spectrum based on the peak maximum temperature T_m, heating rate β and pre-factor ν as described in the equation: $E_d = RT_m \, (ln(\nu T_m / \beta)-3.46)$ provided that E_d is independent on coverage[38]. The Chan-Aris-Weinberg method involves derivation of equations of E and ν in terms of peak maximum temperature T_m and peak width W at half or three quarters of maximum intensity, which is applicable for both first and second order desorption. However, it does not take heating rate β into account when dealing with E though T_m and W could be changed by varying β. Other analysis methods have their own limitations too, for example, heating rate variations[39] is suitable for high coverage adsorption while leading edge analysis[37] has the drawback by use of the leading edge part of the spectra for analysis because the signal/noise ratio in this region of low desorption rates is inherently low.

A simulation method for TPD data analysis rigorously based on Polanyi-Wigner equation (PW) together with equation 2. 37 is applied in this work. It generates a simulated r(t) curve with the PW equation (sharing the t dependence of the experimentally collected TPD data) with initial guesses of each of the parameters. The resulting solution of r(t) is optimized by globally fitting of family of TPD curves with different initial coverage. In this work in chapter 4, TPD curves are taken over a very small change of the initial coverage of water (also quite low coverage) on the surface which is of our interest where only dissociative water adsorption happens and is the situation that most comparable to the theory. For this reason, the TPD analysis methods as discussed above are not suitable in this work.

With the simulation method based on equation 2. 36 and 2. 37 we are able to learn the desorption energy and desorption order. The below is an example of simulated TPD spectra with different initial coverage and desorption order as shown in *Figure 2. 10*.

The spectra in *Figure 2. 10* were simulated results with equation 2. 36 with an assumed pre-exponential factor of $\nu=10^{13}$ s^{-1} (taken to be independent of surface coverage) and a desorption energy of 100 kJ $\cdot$ mol^{-1}. The effect of desorption order and coverage on the spectra can clearly be observed. For first order desorption, the spectra with increasing surface initial coverage show an asymmetric shape and a long

low temperature tail with no coverage dependent shift in the temperature of the desorption maximum. With increasing initial surface coverage desorption maximum shifts to lower temperature of the second order desorption TPD spectra.
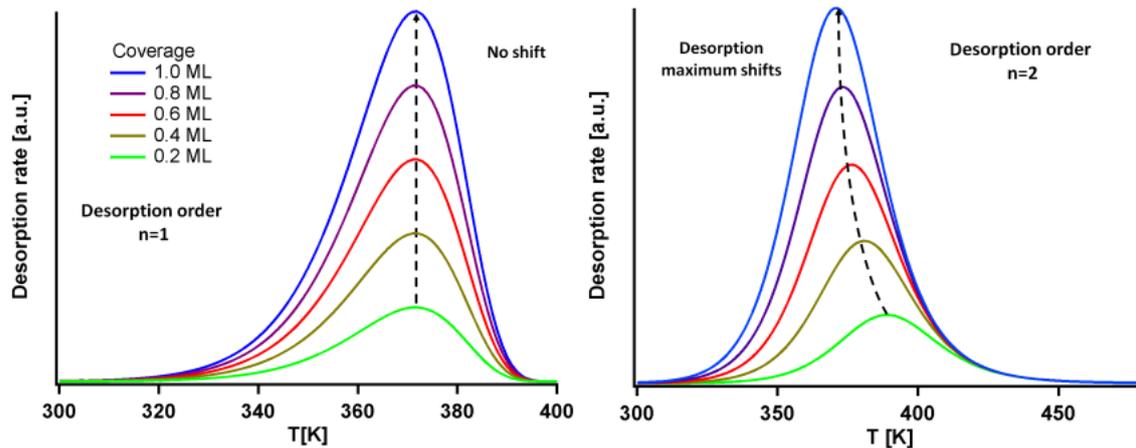
Figure 2. 10 The simulated dependence of the spectral shape of a TPD spectrum on desorption order and coverage. The spectra were simulated with the Polanyi-Wigner equation by assumption of a pre exponential factor ν of 10^{13} and a desorption energy of 100 kJ/mol.

TPD spectroscopy is an important tool to study the kinetics and thermodynamics of adsorbates. Because TPD both characterizes the thermodynamics of molecules leaving the surface, while Sum Frequency Generation Spectroscopy characterizes the structure of those that remain, the two techniques are strongly complementary.

2.4 First Principles Calculation

Theoretical calculations in this thesis, were done by our collaborators Dr. Sophia Heiden ((11-20) surface) and Dr. Giacomo Melani ((0001) surface) from Prof. Dr. Peter Saalfrank's group in University of Potsdam. Here the calculation method will be briefly introduced since the results will be compared with experimental observations in the following chapters. Periodical density functional theory (DFT) in the Kohn−Sham scheme and supercell models were employed to describe the adsorption of water on α-Al_2O_3. The DFT calculations[40] were carried out with the Vienna Ab Initio Simulation Program, version VASP5.2, employing the Projector Augmented Wave (PAW) method[41, 42]. Exchange and correlation were treated in the Generalized Gradient Approximation (GGA) using the Perdew-Becke-Ernzerhof (PBE) function[43]. A plane-wave cutoff of 400 eV and Grimme's D2 correction[40], to account for dispersion interactions, were adopted. These settings were applied for a slab model of both (0001) and (11-20) surfaces. For the structure of (0001) clean surface, Al-I termination, which was

proved to be the most stable structure under UHV conditions by the theoretical work of Kurita[44] and others[45] and also in experiment[46-48], is applied in this work while the O-I termination is the most stable structure under both UHV and high water pressure for the clean (11-20) surface. The atomic layer sequence of (1x1) unit cell of the clean α-Al$_2$O$_3$(0001) surface is -Al-O3-Al-Al-O3- while it is -O-O2-Al4-O2-O- of clean α-Al$_2$O$_3$(11-20) surface.

To allow for low water coverage, we applied a (2x2) super cell model with 10 atom layers for water adsorption on α-Al$_2$O$_3$(11-20) which is confirmed to be sufficiently accurate both for vibrational frequencies and reaction pathways when compared with more atom layers (25 layers). The upper five-layers were optimized to allow for surface relaxation, while the lower five-layers were fixed at the bulk geometry. The surface normal direction of the slab is chosen with a length of 20.5 Å. As a result, the vacuum gap is ~17 Å which is large enough to get rid of spurious interactions between individual slabs. After the termination of clean surface was optimized, a single water molecule will be brought onto the surface of (2×2) super cell, which in principle with 0.08 tML(theoretically defined monolayer, where we think all the Al active sites are occupied by dissociated water thus 12 water on 2x2 super cell) water coverage that is reasonable to compare to a low coverage situation as in experiment. It is difficult to define a monolayer water adsorption in theory, but this model is thermodynamically favorable at low water coverage. The stable structures with adsorbed water is found by optimizing the topmost five-layer slab and water fragments together. To evaluate the thermodynamic properties of the structure, Gibbs free energies G(T) were calculated for both stable species and transition states, according to

$$G(T) = H(T) - TS(T) \approx E + G_{vib}(T)$$

where the enthalpy H(T), the entropy S(T), the absolute temperature T, the self-consistent field (SCF) total energy E, and the vibrational part of the free energy, $G_{vib}(T)$. Since in this thesis understanding the reactivity of water on each surface of α-Al$_2$O$_3$ is one important task to solve, it is necessary to calculate the rates of interconversion of the various possible forms of interfacial water. For this purpose, Eyring's transition state theory was applied:

$$k(T) = \frac{k_B T}{h} e^{-\Delta G^{\ddagger}(T)/k_B T}$$

Here, h and k_B are Planck's and Boltzmann's constants, and $\Delta G^{\ddagger} = G^{\ddagger} - G(educt)$ is the activation free energy for the reaction in question, with $G^{\ddagger}$ being the free energy of the transition state. We located transition states using the Nudged Elastic Band (NEB) with Climbing Image (CI) method[49]. The vibrations are treated in the harmonic approximation by diagonalizing the dynamical matrix at the Γ-point. Only coordinates arising from atoms that were not frozen were considered.

The OH (OD) stretching vibration frequencies are determined based on the above methods on α-Al_2O_3(11-20). For the surface phonon vibrations on α-Al_2O_3(11-20), we applied a thicker slab with 25 atomic layers which is revealed to result more accurate frequencies than the thinner ones. Besides, the dipole square of normal modes of surface phonons were also evaluated as to have a quantitative understanding of SFG experimental results. For α-Al_2O_3(0001) surface, also 2x2 super cell with 25 atomic layers slab was used to calculate the normal mode of surface phonon vibrations.

The calculated stable water adsorbed structures and vibrational results of water fragments and surface phonon of α-Al_2O_3 will be introduced in the lateral part: chapter 3 water adsorption on α-Al_2O_3(11-20) surface, chapter 5 surface phonon on α-Al_2O_3(11-20) and chapter 6 surface phonon on α-Al_2O_3(0001).

2.5 References

1. Dawson, P.H., *Quadrupole mass spectrometry and its applications*. 2013: Elsevier Science.

2. Cvetanović, R.J. and Y. Amenomiya, *A temperature programmed desorption technique for investigation of practical catalysts*. Catalysis Reviews, 1972. **6**(1): p. 21-48.

3. Miller, J.T., et al., *Hydrogen temperature-programmed desorption (H_2 TPD) of supported platinum catalysts*. Journal of Catalysis, 1993. **143**(2): p. 395-408.

4. Elam, J.W., et al., *Adsorption of H_2O on a single-crystal α-Al_2O_3(0001) surface*. The Journal of Physical Chemistry B, 1998. **102**.

5. French, T.M. and G.A. Somorjai, *Composition and surface structure of the (0001) face of α-alumina by low-energy electron diffraction*. The Journal of Physical Chemistry, 1970. **74**(12): p. 2489-2495.

6. Arnolds, H. and M. Bonn, *Ultrafast surface vibrational dynamics*. Surface Science Reports, 2010. **65**(2): p. 45-66.

7. Ji, N., et al., *A novel spectroscopic probe for molecular chirality*. Chirality, 2006. **18**(3): p. 146-58.

8. Yamaguchi, S. and T. Tahara, *Novel interface-selective even-order nonlinear spectroscopy*. Laser & Photonics Review, 2008. **2**(1-2): p. 74-82.

9. Shen, Y.R., *The principles of nonlinear optics*. 1984, New York: Wiley-Interscience,. 575.

10. Shen, Y.R., *Surface properties probed by second-harmonic and sum-frequency generation*. Nature, 1989. **337**: p. 519-525.

11. Shen, Y.R., *Optical second harmonic generation at interfaces*. Annual Review of Physical Chemistry, 1989. **40**: p. 327-350

12. Shen, Y.R., *A few selected applications of surface nonlinear optical spectroscopy*. Proceedings of the National Academy of Sciences, 1996. **93**(22): p. 12104-12111.

13. Trainor, T.P., et al., *Crystal truncation rod diffraction study of the α-Al_2O_3(1-102) surface*. Surface Science, 2002. **496**: p. 238-250.

14. Tanwar, K.S., et al., *Surface diffraction study of the hydrated hematite surface*. Surface Science, 2007. **601**(2): p. 460-474.

15.   Weiss, S., et al., *Ultrafast scanning probe microscopy.* Applied Physics Letters, 1993. **63**(18): p. 2567-2569.

16.   Liu, W.T., et al., *Surface vibrational modes of α-quartz(0001) probed by sum-frequency spectroscopy.* Physical Review Letters, 2008. **101**(1): p. 016101.

17.   Lambert, A.G., et al, *Implementing the theory of sum frequency generation vibrational spectroscopy: a tutorial review.* Applied Spectroscopy Reviews, 2005. **40**(2): p. 103-145.

18.   Paarmann, A., et al., *Effects of crystal anisotropy on optical phonon resonances in midinfrared second harmonic response of SiC.* Physical Review B, 2016. **94**(13).

19.   Winta, C.J., et al., *Second-harmonic phonon spectroscopy of α-quartz.* Physical Review B, 2018. **97**(9).

20.   Sung, J., Y.R. Shen, and G.A. Waychunas, *The interfacial structure of water/protonated α-Al$_2$O$_3$(11-20) as a function of pH.* Journal of Physics: Condensed Matter, 2012. **24**(12): p. 124101.

21.   Liu, W.T., et al., *Sum-frequency phonon spectroscopy on α-quartz.* Physical Review B, 2008. **78**(2): p. 024302-1 -024302-6.

22.   Tong, Y., et al., *Optically probing Al-O and O-H vibrations to characterize water adsorption and surface reconstruction on alpha-alumina: an experimental and theoretical study.* The Journal of Chemical Physics, 2015. **142**(5): p. 054704.

23.   Liu, W.T., et al., *Sum-frequency spectroscopy on bulk and surface phonons of noncentrosymmetric crystals.* Annalen der Physik, 2011. **523**(1-2): p. 101-106.

24.   Lambert, A.G., et al., *Interference effects in sum frequency spectra from monolayers on composite dielectric/metal substrates.* The Journal of Physical Chemistry B, 2002. **106**(21): p. 5461-5469.

25.   Shen, Y.R., et al., *Mapping molecular orientation and conformation at interfaces by surface nonlinear optics.* Physical Review B, 1999. **59**: p. 12632-12640.

26.   Wang, H.F., et al., *Quantitative spectral and orientational analysis in surface sum frequency generation vibrational spectroscopy (SFG-VS).* International Reviews in Physical Chemistry, 2005. **24**(2): p. 191-256.

27.   Cvetanović, R.J. and Y. Amenomiya, *Application of a temperature-programmed desorption technique to catalyst studies*, in *Advances in Catalysis*, D.D. Eley, H. Pines, and P.B. Weisz, Editors. 1967, Academic Press. p. 103-149.

28.   Niwa, M. and N. Katada, *New method for the temperature- programmed desorption (TPD) of ammonia experiment for characterization of zeolite acidity: a review.* The Chemical Record, 2013. **13**(5): p. 432-455.

29.   Laidler, K.J., *The development of the Arrhenius equation.* Journal of Chemical Education, 1984. **61**(6): p. 494.

30.   Laidler, K.J., *Chemical kinetics.* 1994, New York: Harper and Row.

31.   Zambelli, T., et al., *Diffusion and atomic hopping of N atoms on Ru(0001) studied by scanning tunneling microscopy.* Physical Review Letters, 1996. **76**: p. 795-798.

32.   de Jong, A.M. and J.W. Niemantsverdriet, *Thermal desorption analysis: Comparative test of ten commonly applied procedures.* Surface Science, 1990 **233** p. 355-365.

33.   Tokora, Y., et al., *Analysis of thermal desorption curves for Heterogeneous Surfaces: a liear variation of the energy of desorption.* Bulletin of the chemical society of Japan, 1978. **51**: p. 85-89.

34.   Jansen, M., et al., *Influence of nitrogen atoms on the adsorption of CO on a Rh(100) single crystal surface.* The Journal of Physical Chemistry C, 2009. **113**: p. 12277-12285.

35.   Redhead, P.A., *Thermal Desorption of Gases.* Vacuum, 1962. **12**: p. 203-211.

36.   Chan, C.M., R. Aris, and W.H. Weinberg, *An analysis of thermal desorption mass spectra.* Applications of Surface Science, 1978. **1**(3): p. 360-376.

37.   Koppers, J., et al., *Evaluation of flash desorption spectra.* Surface Science 1984. **138**: p. L147-L150.

38.   de Jong, A.M. and J.W. Niemantsverdriet, *Thermal desorption analysis: comparative test of ten commonly applied procedures.* Surface Science, 1990. **233**(3): p. 355-365.

39.   Falconer, J.L., et al., *Flash desrption activation energies: DCOOH decompositon and CO desorption from Ni (110).* Surface Science 1975. **48**: p. 393-405.

40.   Grimme, S., *Semiempirical GGA-type density functional constructed with a long-range dispersion correction.* Journal of Computational Chemistry, 2006. **27**(15): p. 1787-99.

41.   Kresse, G., et al., *From ultrasoft pseudopotentials to the projector augmented-wave method.* Physical Review B, 1999. **59**(3): p. 1758-1775.

42.   Blöchl, P.E., *Projector augmented-wave method.* Physical Review B, 1994. **50**(24): p. 17953-17979.

43.   Perdew, J.P., *Generalized gradient approximation made simple.* Physical Review Letters, 1996. **77**.

44.   Kurita, T., K. Uchida, and A. Oshiyama, *Atomic and electronic structures of α-Al$_2$O$_3$ surfaces.* Physical Review B, 2010. **82**(15).

45.   Marmier, A. and S.C. Parker, *Ab initio morphology and surface thermodynamics of α-Al$_2$O$_3$.* Physical Review B, 2004. **69**(11): p. 115409.

46.   Kirsch, H., et al., *Experimental characterization of unimolecular water dissociative adsorption on α-alumina.* The Journal of Physical Chemistry C, 2014. **118**(25): p. 13623-13630.

47.   Guénard, P., et al., *Determination of the α-Al$_2$O$_3$(0001) surface relaxation and termination by measurements of crystal truncation rods.* Surface Review and Letters, 1997. **5**: p. 321-324.

48.   Soares, E.A., et al., *Structure of the α-Al$_2$O$_3$(0001) surface from low-energy electron diffraction: Al termination and evidence for anomalously large thermal vibrations.* Physical Review B, 2002. **65**(19): p. 195405.

49.   Henkelman, G., et al., *A climbing image nudged elastic band method for finding saddle points and minimum energy paths.* The Journal of Chemical Physics, 2000. **113**(22): p. 9901-9904.

Chapter 3 Water dissociative adsorption on α-Al$_2$O$_3$(11-20)

(The work in this chapter has been partly published previously in J. Phys. Chem. C 2018, 122, 6573−6584)

As the third most stable alumina surface, α-Al$_2$O$_3$(11-20) also plays an important role in heterogeneous catalysis[1-3]. The oxygen terminated (11-20) has performs differently in many applications than the most stable, Al-terminated, (0001) surface. For example, it was reported single wall carbon nanotubes obtained aligned growth on (11-20) but only grow randomly on (0001)[4]. The knowledge of surface structure and termination is of crucial importance to understand these behaviors. Water interaction with α-Al$_2$O$_3$ is of the interest of surface scientists because it changes surface properties, presumably by changing surface structure and termination, significantly [5, 6]. Prior work demonstrates even small amounts of water could change the surface reactivity, polarity and stability of α-Al$_2$O$_3$ dramatically [7-9]. To investigate the interaction with sub-monolayer water or ever single water molecule adsorption is good start point. As one of the most thermodynamic stable surfaces, (11-20) is much less studied as compared with (0001) or (1-102) surfaces which have been relatively well studied both in experiment and theory [10-17] with single water molecular adsorption as shown in *Figure 3. 1*. Thus, in this chapter we will focus our study on the interaction between water and (11-20) surface in UHV system where allows the preparation of sub-monolayer water adsorption with a combined experimental and theoretical approach.
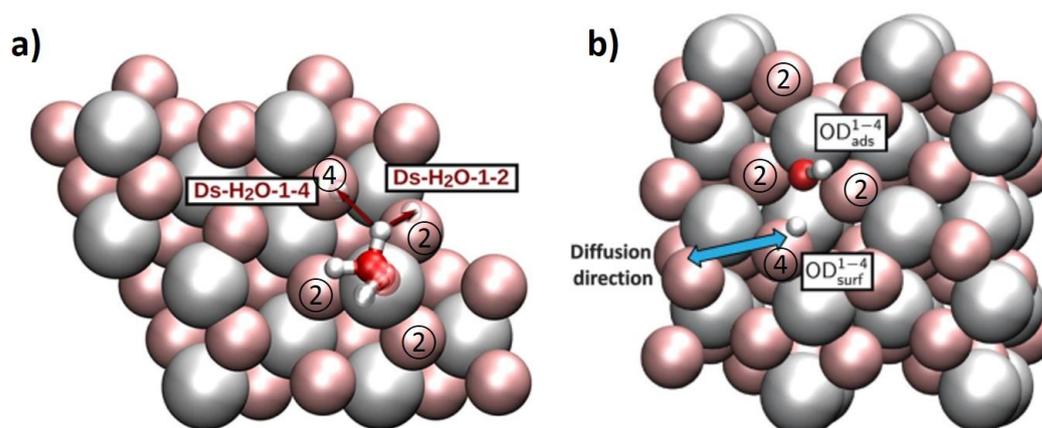

Figure 3. 1 Water dissociation structures on α-Al$_2$O$_3$(0001)[17] and (1-102)[16] surfaces: a) 1-2 and 1-4 dissociative structure on (0001); b)1-4 dissociative structure on (1-102).

From an experimental perspective, SFG is carried out to probe the interfacial OD stretching vibrations at different water coverages; from the theoretical perspective, the stable adsorption sites for molecular

water and dissociated fragments are identified based on the methods described in chapter 2, and the reaction coordinates and rates for some of the possible interconversion reactions calculated. Given the apparent agreement between theory and experiment, at the end of this chapter, the reactivity of each surface of α-Al₂O₃ with respect to water dissociative adsorption is discussed.

3.1 UHV prepared, water-free, O-I terminated α-Al₂O₃(11-20)
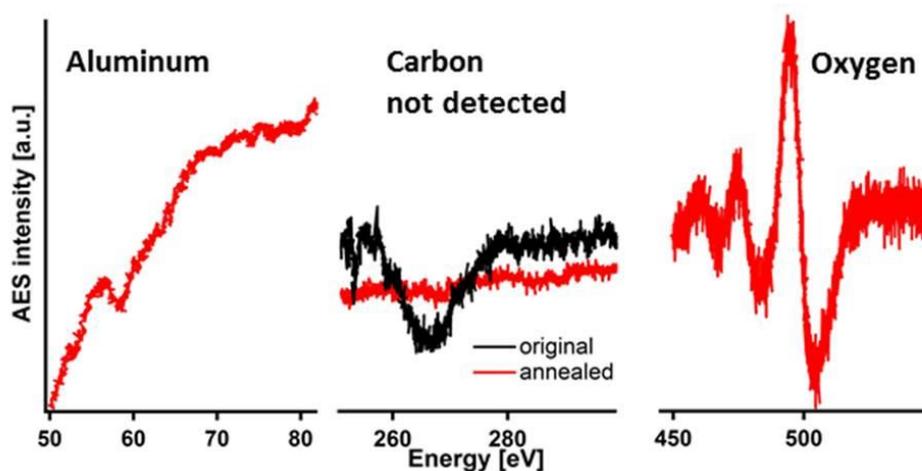
Figure 3. 2 Auger spectra of a sputtered and annealed α-Al₂O₃(11-20) crystal.

Mounting the roughly cleaned sample (ultrasonic treatment in methanol, acetone and Milli-Q water, each for 15 min, see section 2.1.2) in the UHV chamber produces a surface that still shows carbon contamination in Auger Electron spectroscopy (AES) as shown in Figure 3. 2 (black line of carbon region). To remove the carbon, as described in section 2.1.2, the sample was further sputtered and annealed at high temperatures[13]. This treatment produces a clean surface with carbon contamination below detection in AES measurements (red line in Figure 3. 2).

To characterize the surface structure of this clean α-Al₂O₃(11-20) with LEED is challenging due to the poor electrical conductivity, and thus presumably propensity to surface charging, of α-Al₂O₃: in general, it is difficult to see a clear LEED pattern and, often when one is observed, some peaks appear broadened. As a result, some regions of the LEED pattern show a clear 1x1 lattice [18] while others are signal free. To obtain a more complete pattern, we collected a series of LEED patterns at different energies as shown in Figure 3. 3. Combining the LEED patterns collected at 272 and 265 eV produced the well-defined pattern shown in Figure 3. 4b. Figure 3. 4a is the surface structure (top view) in theory of α-Al₂O₃(11-20) where the unit cell in real space is labeled with a red solid line. The ratio between the two basis vectors (the shorter labeled as $\vec{a}$, the longer as $\vec{b}$) was 1.57 as indicated in LEED pattern and 1.65 in the theoretical calculations in this work. Taking account of the uncertainty that introduced when

measuring the vectors in LEED pattern by hand, we would like to say experiment agrees with theory. This results also agreed with Becker's observations[19] where the ratio between the two basis vectors were 1.50 and 1.61(a bit smaller than we calculated since they calculated the unrelaxed termination) in experiment and in theory, respectively (as summarized in Table 3. 1).
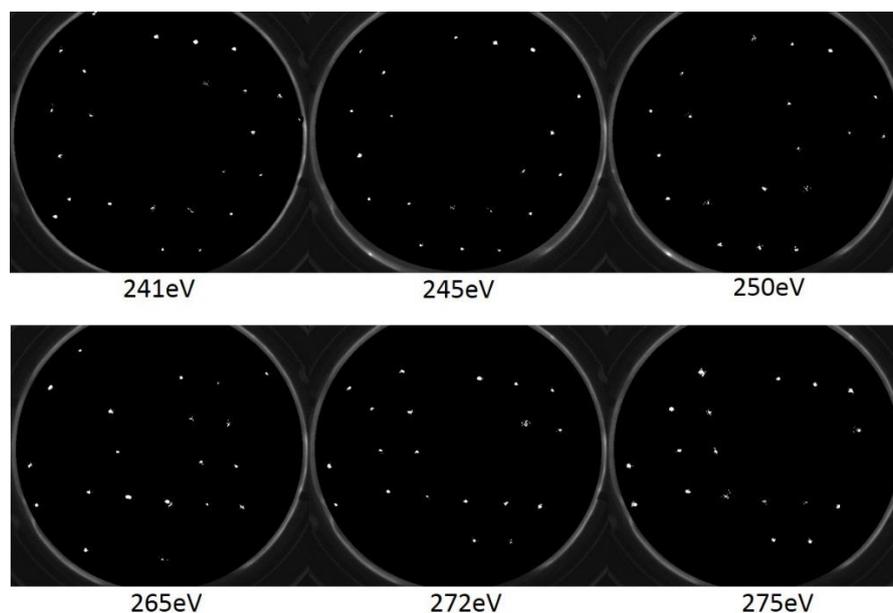
Figure 3. 3 LEED patterns of clean α-Al$_2$O$_3$(11-20) obtained at different energies
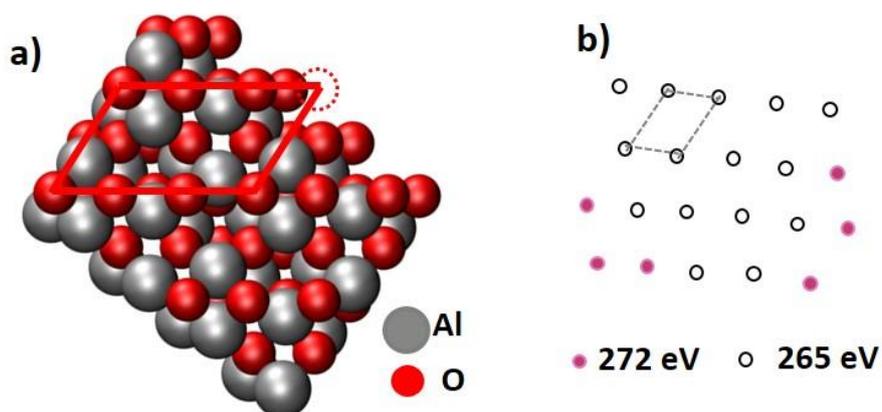
Figure 3. 4 (a) The geometry optimized α-Al$_2$O$_3$(11-20) surface used in this study with the surface unit cell indicated in red. (b) Reciprocal lattice constructed from LEED patterns collected at 272 eV (pink) and 265 eV (black circle).

This obtained (1x1) LEED pattern indicates that there are neither significant densities of defects nor of steps on the water-free surface. The reasons for such a conclusion are:

1. Defects due to the uncorrelated atom at high density would be expected to lead to a non-specular background that smears diffraction spots which is not the case in our study. Thus density of uncorrelated atomic defects is low.

2. The correlated atomic defects is of low density. If it is high, a superstructure pattern is possible to appear, in addition to the (1x1), for which we see no evidence.

3. If steps occur with high densities, the spots will be split in the (1x1) pattern along the direction of either basis vector. The step density should be low as no evidence of such splitting was observed.

Table 3. 1 Lattice parameters of the α-alumina(11-20) surface in this study and that of Becker et al[19] (θ is the angle between vectors a and b). Note that in constructing the unit cell from the theoretical structure we here employ an alternative definition to that used in developing the slab model in Figure 3. 5 in order to compare with Becker's work.

	Calculation				Experiment
	$|\vec{a}|$	$|\vec{b}|$	θ	$\dfrac{|\vec{b}|}{|\vec{a}|}$	$\dfrac{|\vec{b}|}{|\vec{a}|}$
this study	5.18Å	8.54Å	55.8°	1.65	1.57
Becker et al.	5.12Å	8.24Å	58.5°	1.61	1.50
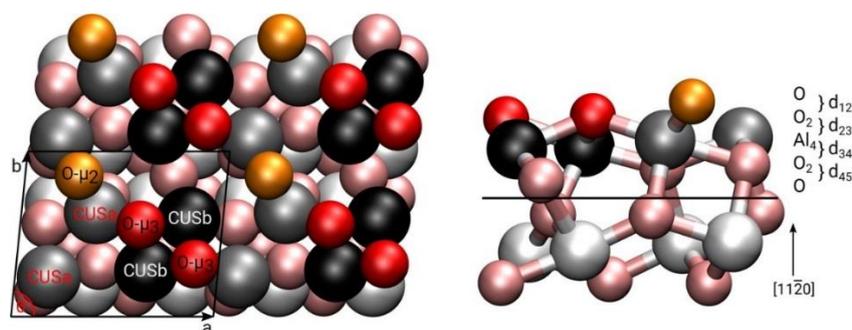
Figure 3. 5 Top view (2x2 super cell) and side view of O-I terminated α-Al2O3(11-20) surface: 2-fold oxygen gold ball, 3-fold oxygen red ball, CUSa Al atom grey ball and CUSb Al atom black ball.

Finally, to clarify further discussion, it is useful to categorize the particular types of surface atoms present on the O-I terminated α-Al$_2$O$_3$(11-20). As shown in Figure 3. 5, which displays the top and side view of this surface termination, the outmost layer is 2-fold coordinated oxygen atoms (O-μ2) with 3-fold coordinated oxygens (O-μ3) atoms in the immediate sub-layer followed by aluminum layer. This Al layer contains two kinds of Coordinatively UnderSaturated (CUS) Al atoms here defined as CUSa

and CUSb. CUSa is bonded to both 2- and 3-fold coordinated O atoms while CUSb is bonded only to 3-fold coordinated O atoms. The atomic sequence in the surface normal direction is $OO_2Al_4O_2O$ (where the indices give the number of atoms per layer in the (1x1) unit cell) and that of a (2x2) consequently O4-O8-Al16-O8-O4. Two of these sequences, i.e. ten atomic layers with 48 O and 32 Al atoms in total, were used in the calculations discussed in this chapter. The upper five-layers (above the solid line in Figure 3. 5) were optimized to allow for surface relaxation while the lower five-layers were fixed at the bulk geometry. To test the accuracy of the results based on this model, i.e. 10 atomic layers, calculations were carried out also on slabs with more layers, as discussed further in the following section.

3.2 Theory results of water adsorption on α-Al₂O₃(11-20)

The first principle calculation of water adsorption on α-Al_2O_3(11-20) at low coverage is done by our collaborator Dr. Sophia Heiden from Peter Saalfrank's group in University of Potsdam. The methodological approach was introduced in detail in section 2.4 chapter 2. The calculation is done by putting one water molecule onto 2x2 super cell of α-Al_2O_3(11-20), which is around 0.08 tML. Note that from the theoretical point of view a monolayer is defined as 12 water molecules on this 2x2 super cell. The resulting saturation of surface oxygens is a convenient reference point, no calculations were done that demonstrate that this structure is favorable for water at this surface density. To indicate the difference, and fundamental incompatibility, of the definitions of a monolayer in theory and experiment we call them tML and eML respectively. However, it is worth emphasizing that any discrepancy between estimated surface coverages in theory and experiment is likely significant only at high coverage, in the low coverage limit both definitions converge.

Table 3.2 Adsorption energies E_{ads} in eV of molecular and dissociated water species on α-Al_2O_3(11-20) surface calculated with 10 atomic layers slab.

	Species	E_{ads}
molecular	CUSb	-1.78
dissociated	Inter-CUSa/Oμ2	-2.5
	Inter-CUSa/Oμ3	-1.67
	CUSb/Oμ2	-2.28
	CUSb/Oμ3	-1.19
	Inter-CUSb/Oμ2	-2.09
	Inter-CUSb/Oμ3	-1.89

The adsorption energy of water on the α-Al_2O_3(11-20) surface (one water on 2x2 super cell, ~0.08 monolayer) is defined as $E_{ads} = E_{ads. \, species} - E_{free \, molecule+surface}$, the results of molecular and dissociated water adsorption are listed in Table 3.2.

There is one type of adsorption cite for molecular water, a CUSb Al cite with E_{ads} -1.78eV, and six possible dissociated structures for water adsorption. Other types of molecular adsorption, e.g. above or between two adjacent CUSa sites (inter-CUSa) or between two adjacent CUSb sites (inter-CUSb), do not take place at the level of theory (introduced in section 2.4 chapter 2) employed in this study: geometry optimizations starting from molecular water placed above either of these sites at different heights converge to dissociatively adsorbed species. However, molecular adsorption sites other than CUSb could be possibly found when different starting structures and/or electronic structure methods are employed.

For dissociative adsorption, the three most favorable structures observed are the result of the D (in this work D_2O is used) adsorbing to surface 2-fold coordinate oxygen, i.e. Oμ2, while the three less favorable adsorbate structures involve D adsorption to a 3-fold coordinated oxygen, i.e. Oμ3. Of the three structures in which D adsorbed to Oμ2, the most favorable is inter-CUSa/Oμ2 with E_{ads} -2.5 eV, the second most favorable CUSb/Oμ2 with E_{ads} -2.27 eV and the third inter-CUSb/Oμ2 with E_{ads} -2.09 eV. In this notation inter-CUSa/Oμ2 means the OD originating from the adsorbing D_2O, i.e. OD_{ads}, bonds to two CUSa Al atoms while D fragments (from water) combine with surface Oμ2 to from OD_{surf}. Similarly, structure CUSb/Oμ2 means OD_{ads} bonded with one CUSb Al atom while the D fragment combines with surface Oμ2; and structure inter-CUSb/Oμ2 means dissociated OD_{ads} bonds to two CUSb Al atoms while the D fragment bonds to surface Oμ2 (as shown in Figure 3. 6 and Figure 3. 7). While the thermodynamic picture seems clear, to fully understand the dissociative structure it is desirable to understand the kinetics of interconversion between minimum energy structures of each of the adsorbed species. Eyring transition state theory in combination with Nudged Elastic Band (NEB) transition state/minimum energy path method is applied for this purpose.

a) Ds: CUSb→CUSb/Oμ2

b) Df: CUSb/Oμ2→inter-CUSb/Oμ2

c) Df: CUSb/Oμ2→inter-CUSa/Oμ2
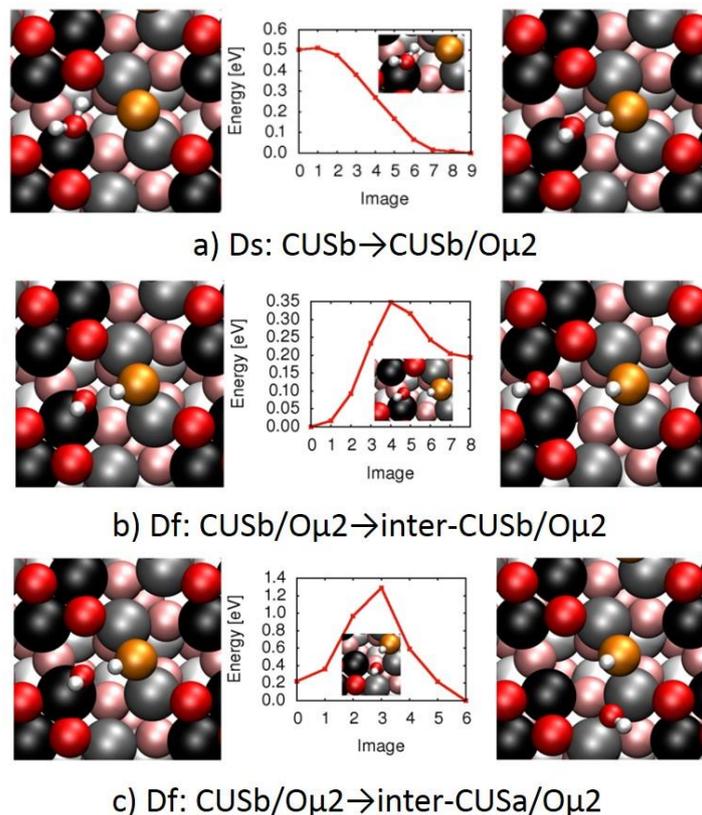
Figure 3. 6 PBE+D2 minimum energy paths with transition states (inlay; if available): a) from molecular adasorption of water at CUSb to dissociated structure CUSb/Oμ2; b) diffusion from CUSb/Oμ2 to inter-CUSb/Oμ2; c)diffusion from CUSb/Oμ2 to inter-CUSa/Oμ2.

We take molecular adsorption at CUSb as a start point. Figure 3. 6a shows the result of nudged elastic band calculations exploring the dissociation of molecular water adsorbed on CUSb. As it clearly presents there is almost no barrier (0.01 eV) from molecular adsorption CUSb to dissociative structure CUSb/Oμ2, leading to a classical dissociation rate constant at 300 K (discussed later in Table 3. 7) of $k_{diss,300K} = 5.76 \times 10^{12}$ s^{-1}. Due to the high reactivity of this dissociation reaction, water dissociation at CUSb/Oμ2 could be considered as the initial dominated structure. Other thermodynamically favored structure could be reached by diffusion. Figure 3. 6b shows the diffusion pathway from CUSb/Oμ2 to inter-CUSb/Oμ2, the third most favorable structure for water dissociation with the energy barrier which is 0.35 eV, yielding $k_{diss,300K}$ is ~1.8×10^6 s^{-1} which is also exoenergetic/exergonic. For the most favorable structure inter-CUSa/Oμ2, which is 0.23 eV more stable than CUSb/Oμ2, however, the conversion from the latter seems to be impossible since the barrier is much higher as 1.07 eV while the corresponding $k_{diss,300K}$ is ~2.4×10^{-6} s^{-1} as displayed in Figure 3. 6c.

To sum up, the kinetics of the most favorable dissociation structure inter-CUSa/Oμ2 is unclear with the calculation method in this work. Given the thermodynamics of water adsorption on (11-20) is clear, theory could not present a complete description of the kinetic network of all possible reactions. But one

thing is sure that water will dissociatively adsorb on (11-20) surface at low coverage with this three most thermodynamic stable structure inter-CUSa/Oμ2, CUSb/Oμ2 and inter-CUSb/Oμ2 while the first one is the most favorable.

To evaluate the effects of slab size on calculation results especially adsorption energies, results obtained with different sizes of slabs of molecular and the three most favorable dissociatively adsorbed structures are listed in Table 3.3.

Table 3.3 Calculated adsorption energies in eV of molecular and dissociated water species based on different size of slabs that with 10, 15, 20 and 25 atomic layers, respectively.

System	10 layers	15 layers	20 layers	25 layers
CUSb	-1.78	-1.8	-1.81	-1.83
Inter-CUSa/O-μ_2	-2.50	-2.46	-2.54	-2.56
CUSb/O-μ_2	-2.27	-2.35	-2.36	-2.35
Inter-CUSb/O-μ_2	-2.09	-2.43	-2.48	-2.36

As can be seen, the molecular adsorption energies slightly decreased from -1.78 eV to -1.83 eV as the slab is increased from 10 atomic layers to 25 layers thick. While the absolute values of E_{ads} of dissociated species change somewhat with slab size inter-CUSa/Oμ2 stays always as the most favorable of the three structures while inter-CUSb/ Oμ2 becomes more stable with thicker slab. The change in slab size won't change the vibrational frequencies of OD on the surface much, the biggest error when comparing the 10-layer model to results obtained with a thicker slab are expected for reaction rates (discussed later in Table 3. 7): 0.1 eV change in the active free energy will cause one order of magnitude change in the rate constant (so that the rate constant of this surface should be even larger with 25-layer slab model). The following discussions are all related to the theory results that obtained with the 10 layer slab.

inter-CUSa/Oμ2   CUSb/Oμ2   inter-CUSb/Oμ2
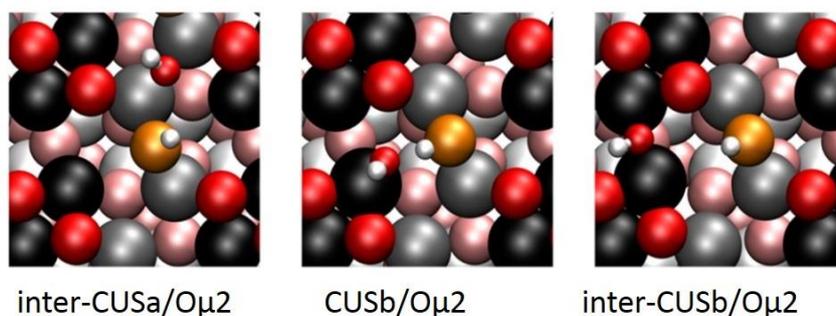
Figure 3. 7 Adsorption geometries for the three most favorable dissociatively adsorbed structures: 2-fold oxygen gold ball, 3-fold oxygen red ball, CUSa Al atom grey ball and CUSb Al atom black ball.

Table 3. 4 Calculated stretching vibration frequencies of different types of dissociated OD species on α-Al$_2$O$_3$ (11-20) and Boltzmann populations at various temperatures (take the most stable site inter CUSa/Oμ2 as 1, others are relative values to this).

OD type		θ($^\circ$)	ν(cm^{-1})	P_{130K}	P_{300K}	P_{400K}
Inter-CUSa/Oμ2	OD$_{ads}$	44	2731	1	1	1
	OD$_{surf}$	36	2694			
CUSb/Oμ2	OD$_{ads}$	26	2785	1.4x10^{-6}	6.1x10^{-3}	3.2x10^{-2}
	OD$_{surf}$	60	1711			
Inter-CUSb/Oμ2	OD$_{ads}$	53	2692	1.0x10^{-15}	1.2x10^{-6}	6.6x10^{-5}
	OD$_{surf}$	41	2689			

Since, as discussed in chapter 2 in detail, the SFG signal intensity is a function of OD orientation with respect to the surface normal, the angle of each OD fragment in the minimized structure and its harmonic frequencies of OD stretching vibration were calculated. These results are shown in the left half of Table 3. 4. To tell the relative abundance of these three kinds of dissociated configurations, Boltzmann weights $P = \exp(-G_i/k_BT)$ based on the free energy of each configuration were also calculated for various temperatures relevant for this work, relative to the value for the most stable inter-CUSa/Oμ2 configuration, as shown in Table 3. 4.

3.3 Experimental results of D$_2$O adsorption on α-Al$_2$O$_3$(11-20)

Given the theory calculations as discussed above, one might be able to make certain predictions about the relative stability of dissociatively adsorbed water structures in the limit of unimolecular adsorption (i.e. low coverage) on α-Al$_2$O$_3$(11-20). If one wants to ask whether any of these predictions are apparent in experiment it is necessary to a.) create a relatively defect free (11-20) clean surface b.) put a small amount of water on it and c.) characterize the structure of the adsorbed water.

As discussed above LEED (Figure 3. 3) and Auger (Figure 3. 2) results suggest we can prepare a carbon free 1x1 well defined (11-20) surface with a low density of defects and steps with the methods described in section 2.1.2 chapter 2. To prepare this surface with small amount of water, D$_2$O was dosed through a supersonic molecular beam source (MBS) while the sample was cooled down to liquid nitrogen temperatures. To create low coverage samples the sample was next rapidly annealed to higher temperatures and returned to liquid nitrogen temperatures. Temperature programmed desorption (TPD) spectra were carried out to define the relative coverage of water. To characterize the structure of the adsorbed water, sum frequency generation SFG spectra were collected on the prepared samples. As discussed in detail below much prior work, and the normal mode calculations, suggest the frequencies

of OD stretching vibrations are sensitive to local structure. Therefore, in the following part I am going to introduce you the results of both TPD and SFG measurements.

3.3.1 TPD results of samples prepared with different D₂O coverage

TPD measurement was carried out on a series of samples with different water coverages (prepared by annealing the sample to different temperatures as discussed in section 2.1.2 and above) with a heating rate of 100 K/min. The results are displayed in Figure 3. 8 and Figure 3. 9. Both series of TPD traces clearly show there is no obvious background desorption in the measurement. Such background desorption, if it existed, would be expected to produce a desorption peak at temperatures below the maximum annealed temperature of the samples and an apparent tail at high temperature. Neither feature is apparent in the data. It is quite obvious that TPD curves collected of samples that were annealed to147 and 165 K (Figure 3. 8) are both much more intense (even more intense than 175 K curve that is scaled by x10) and contain a shoulder to lower temperatures absent from TPD spectra of samples annealed to 175 K and higher (see Figure 3. 9). It is additionally apparent that the TPD trace of the sample annealed to 175 K shows a shoulder at high temperature and the peak maximum temperature is below 200 K. TPD spectra of samples annealed to 183 K and higher show only expected qualitative changes: all appear with a shoulder at high temperature and differences with increasing intensity are consistent with a loss of surface adsorbate population in each annealing step.
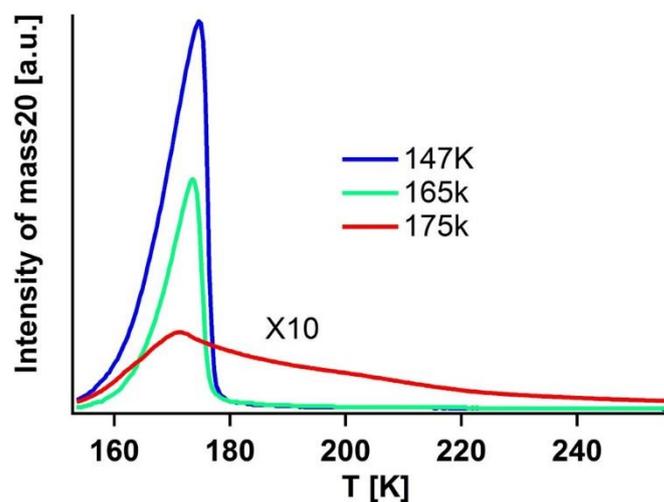
Figure 3. 8 TPD spectrum of mass 20 (D₂O) for α-Al₂O₃(11-20) samples prepared as described above after annealing to 147, 165 and 175K while the TPD trace of the sample annealed to 175 K was multiplied by 10.

These data could be most easily understood if for samples annealed to 147 and 165 K the TPD spectrum is dominated by the desorption from D₂O ice (this peak increases in intensity with dosing and its asymmetric character towards lower temperatures is characteristic of the zero[th] order desorption

expected in this system). The remaining TPD spectra are most easily understood if after annealing to 175 K there is both multilayer and monolayer adsorbed water on the surface while for samples annealed to 183 K and above the TPD spectra record only the desorption of the water monolayer. That is, the above discussion suggests that the monolayer can be reached by annealing the sample to a temperature between 175 and 183 K (but clearly closer to 183 K). In this study I assume that the 183 K spectra captures the monolayer desorption and define the coverage of a sample annealed to this temperature as 1.0 eML (note that this definition is consistent, as is data we show below, with a scenario in which the saturated monolayer contains both dissociative and molecular water adsorption. The definition of a monolayer in theory, as discussed above, does not allow this possibility). This assumed temperature is estimated to result in an uncertainty of ± 2 % (if the monolayer happens at sample flashed to 175 K) monolayer (at the maximum) in surface coverage. By integrating the area under each TPD curve, and comparing it to the area of the 183 K TPD curve, the relative coverage present after each annealing temperature was calculated. This approach suggests samples annealed to 200, 300 and 400 K are covered by 0.8, 0.14 and 0.05 eML respectively.
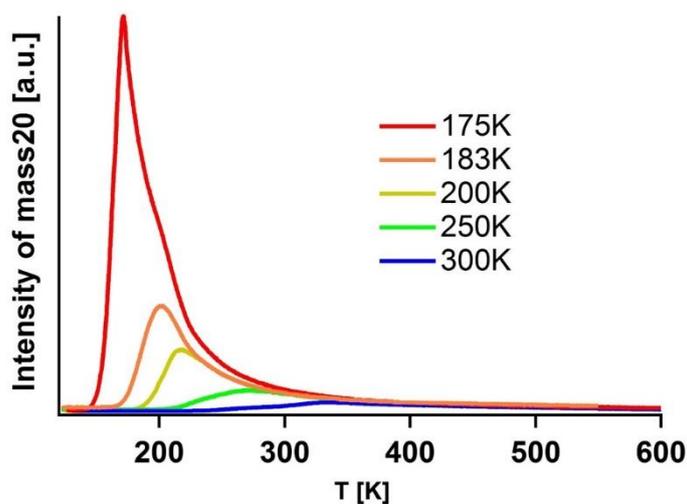
Figure 3. 9 TPD spectrum of mass 20 (D_2O) for α-Al_2O_3(11-20) samples annealed to high temperatures as 175, 183, 200, 250, and 300 K.

As mentioned earlier in this chapter, the dissociative adsorption of water in the low coverage limit is of particular interest. In principle, molecular adsorption of water may occur as coverage increases, i.e. the thermodynamically favorable monolayer may be a mixture of molecularly and dissociatively adsorbed water, on the α-Al_2O_3(11-20) surface. To distinguish molecular adsorption from dissociative adsorption experimentally, and to ensure that the experimental results we will compare to theory are dominated by dissociatively adsorbed water, SFG is applied to probe the bending mode vibrations of D_2O (once D_2O dissociates no bending mode should be apparent) in the next section.

3.3.2 Bending vibration of D_2O probed by SFG

Dosing D_2O onto the sample at 130 K generates ice multilayers and might be expected to have a strong bending vibration feature in SFG spectra. Figure 3. 10, shows SFG collected from a sample with ice at 130 K, annealed to 200 K (0.8 eML) and 300 K (0.14 eML) in D_2O bending mode vibrations at ~1265-1285 cm^{-1} [20]. It is clear that sample with ice on top shows a strong resonance at around 1300 cm^{-1} while the signal intensity decreases and shifts to somewhat lower frequencies as coverage is descreased first to 0.8 and then 0.14 eML. The bend mode frequency of 130 K is higher which is due to the strong D-bond in ice that is reported to increase the bend mode frequency[21] of water. The resonance of D_2O bending mode disappears almost completely when the coverage was reduced to 0.14 eML. It is not difficult to conclude that for samples with water coverages 0.14 eML and lower, molecularly adsorbed water populations are below our SFG detection limit. We therefore expect that, at coverages below 0.14 eML, both the SFG spectral response, and the water structure, should be dominated by dissociatively adsorbed water.
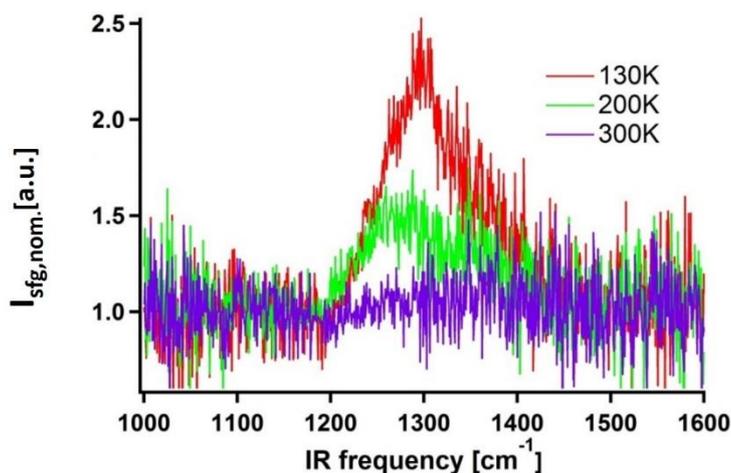
Figure 3. 10 Probing D_2O bending vibrations with SFG on α-Al_2O_3(11-20) surface.

3.3.3 OD stretching vibration probed by SFG

To study the structure of the fragments resulting from water dissociative adsorption on the α-Al_2O_3(11-20) surface, SFG is employed to probe OD stretching vibrations near 2700 cm^{-1}. The results are displayed in Figure 3. 11, the SFG signal is divided by its corresponding non-resonant response to account for the frequency dependence of our infrared source's intensity.

Looking at SFG spectra collected of sample with water coverage of 0.80 eML, a strong resonance centered at around 2780 cm^{-1} with a shoulder towards lower frequency is observed. Since we already know at this coverage there are both molecularly and dissociatively adsorbed water on the surface

(suggested by OD bending spectra in Figure 3. 10), the shoulder at low frequency should be assigned to the OD stretching vibration from molecularly adsorbed D_2O—since the calculated frequency of OD stretching of molecular water is 2689 cm^{-1}(the other vibrates at 2140 cm^{-1} which is out of detection window) which is lower than that of dissociated OD species on the surface that are expected to be observable in SFG spectra (as discussed later, see Table 3. 6). As for the other two samples loaded with 0.14 and 0.05 eML water coverage, only dissociative water adsorption is favorable thus the low frequency shoulder disappears for both of them, leaving only resonances of (Al-)OD stretching vibrations. All three spectra seem to also have weak resonance located at around 2840 cm^{-1}. Since our measured SFG intensity results from both a non-resonant and resonant contribution, one cannot directly tell the frequency of each resonance feature that appears in the spectra. To fully understand these resonance features and try to assign these observed resonances to surface structure, I model the data with the line shape model as described in detail in chapter 2.
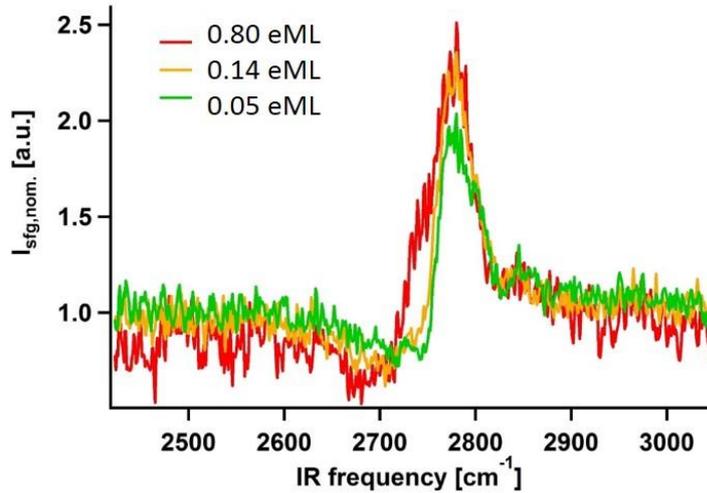
Figure 3. 11 SFG spectra of OD stretching vibrations on α-Al$_2$O$_3$(11-20) surface at coverage 0.80 eML, 0.14 eML and 0.05 eML, respectively.

Analyzing the data using the line shape model in Equation 2.24 is an under constrained minimization problem.

$$\chi_{ijk}^{(2)} = \chi_{nr}^{(2)} + \chi_{r}^{(2)}$$

$$= |A_{nr}|e^{i\theta} + \sum_{q} \frac{|A_q|e^{i\theta_q}}{\omega_{IR} - \omega_q + i\Gamma} \tag{2.24}$$

There are 2 parameters to describe the non-resonant part and 4 parameters (amplitude, line width, center frequency and phase) for each resonance. The fitting is firstly simplified by taking the phase of the non-resonant to be zero and the phase of each resonance can be considered as the relative value as referred to the phase of non-resonance, results are listed in Table 3. 5.

The non-resonant and resonant phases describe their, mutual interference. In the simplest possible description of the resonances their phases, line widths and center frequencies would be independent of surface coverage: all differences between the two spectra shown in Figure 3. 12 could be explained by the difference in OD species population. In practice it was found that this description was not possible: while the data could be well described by a model in which center frequency and phase were independent of coverage, line width appeared to narrow as coverage was decreased for all three resonances. The physical origin of this line width narrowing is not clear. It is possible that each of the resonances at 0.14 eML reflects a degree of inhomogeneous broadening.
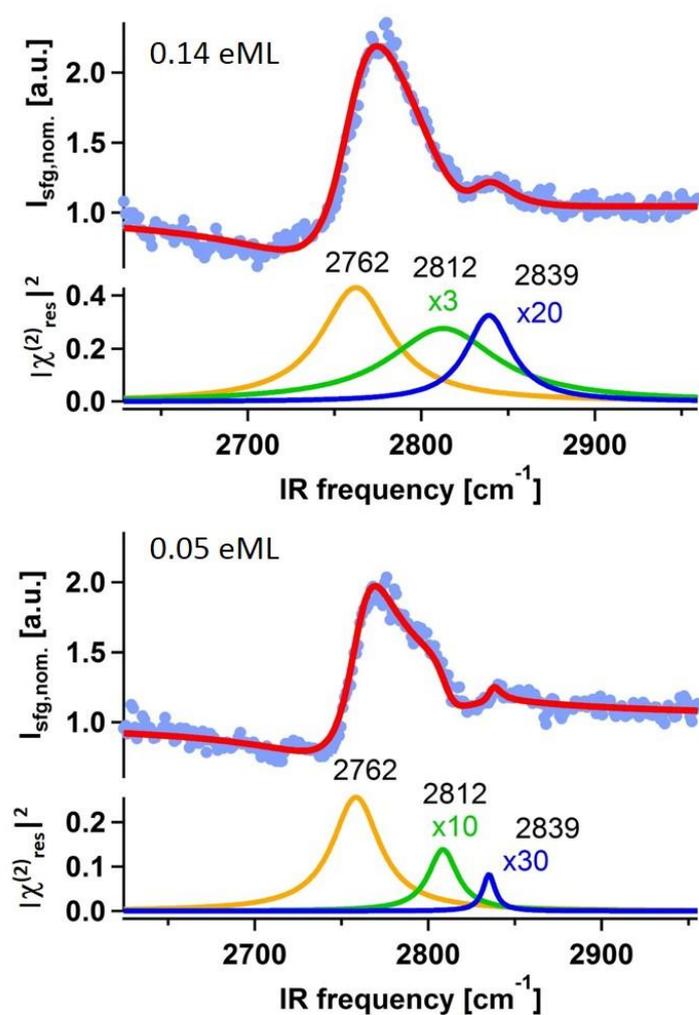
Figure 3. 12 Fitting results of SFG data: top panel data for 0.14 eML and bottom panel data for 0.05 eML, extracted squared modulus of resonance are plotted below each data set.

Given these assumptions, and conducting a global fitting of both data sets, there is a strong resonance centered at 2762 ± 0.4 cm^{-1}, and two weaker resonances 2812 ± 1.4 and 2839 ± 2 cm^{-1} respectively. Each

parameter for this global fitting are shown in Table 3. 5, which are found to be insensitive to initial guesses.

To assign the three experimentally observed spectral resonances, I would like first to focus on the calculated frequencies in Table 3. 4. These frequencies can be put in four groups: the OD_{ads} group from the CUSb/Oμ2 adsorbate configuration is highest at 2785 cm^{-1}, the OD_{ads} group from the inter-CUSa/Oμ2 configuration is somewhat lower at 2731 cm^{-1}, the OD_{surf} group from the inter-CUSa/Oμ2, the OD_{ads} from the inter-CUSb/Oμ2 and the OD_{surf} from the inter-CUSb/Oμ2 range from 2689-2694 cm^{-1}, and the OD_{surf} from CUSb/Oμ2 is lowest in frequency at 1711 cm^{-1} (and well out of our experimental window). It is not immediately clear how the three resonances apparent in the experimental data relate to the left three frequency groups in the calculation.

Table 3. 5 Global fitting results for samples with 0.14 and 0.05 eML water coverage.

			0.14 eML		0.05 eML	
	$\nu(cm^{-1})$	phase	A(arb. u.)	Γ	A(arb. u.)	Γ
Res1	2762±0.4	3.4±0.03	16.1±0.7	24.2±0.7	8.4±0.19	16.6±0.43
Res2	2812±1.4	0.47±0.1	11.5±1.4	37.8±4.2	1.21±0.24	10.2±1.9
Res3	2839±2	-2.0±0.36	2.0±0.7	16±3.9	0.22±0.1	4.3±2.25

Nr	A_{nr}	Phase/nr
	1.006±0.003	0

As mentioned in chapter 2, the intensity of the measured emitted sum frequency field is proportional to the squared number of oscillators. To address the likely contribution of OD oscillators from each adsorbate configuration to our observed SFG spectra, we need to know their relative populations. While kinetic trapping of unstable species cannot be excluded with certainty, we addressed this problem by assuming the surface was at thermal equilibrium and calculating Boltzmann probabilities of the inter-CUSa/Oμ2, CUSb/Oμ2 and inter-CUSb/Oμ2 configurations. This analysis, for temperatures of 130, 300, and 400K is shown in Table 3. 4. Clearly, over the temperature range relevant in experiment we would expect to see only contribution from OD oscillators in the most stable inter-CUSa/Oμ2, and, perhaps, the second most stable CUSb/Oμ2 configurations.

In addition to its dependence on oscillator population squared, SFG intensity is also dependent on the orientation of surface OD species. The details of this relationship have been reviewed in chapter 2 and in previous published work [22, 23]. Given an assumed molecular response from the DFT calculation, it is possible to calculate the variation of SFG intensity with OD species orientation. The results of this

calculation, for the ppp polarization condition with incident angles of 75/70° (Vis/IR) with respect to the surface normal are plotted in Figure 3. 13. Clearly the SFG signal dies off quickly with the angle.

This plot suggests that the OD_{surf} in the CUSb/Oμ2 configuration (θ=60°) and the OD_{ads} in the inter-CUSb/Oμ2 configuration (θ=53°) will be 578 and 33 times less intense than the, most intense, OD_{ads} from the CUSb/O2 (θ=26°) purely as a result of orientation. Clearly we would not expect these OD species, if they occur at the surface, to be visible in our SFG measurements. As noted above, theory suggests that at the low coverages sampled in experiment the great majority population of adsorbed D_2O will be found in the inter-CUSa/Oμ2 configuration with a maximum (at T = 400 K) of about 1/30 of D_2O dissociatively adsorbed in the CUSb/Oμ2 and 1/15000 inter-CUSb/Oμ2 (see Table 3. 4). This population analysis implies, in the same sense that it is quite unlikely that enough OD_{surf} (from the inter-
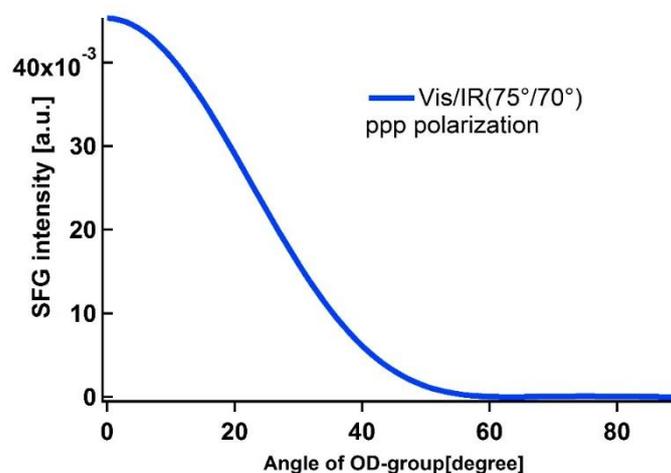
Figure 3. 13 SFG intensity as a function the O-D group orientation relative to the surface normal, under ppp (SFG/Vis/IR) polarization combinations, input beam angle Vis/IR 75°/70°

CUSb/Oμ2) is present to contribute to our measured signal. Taken together these arguments suggest that the three species present in our experimental observables are likely OD_{ads} (inter-CUSa), OD_{surf} (from the inter-CUSa/Oμ2 configuration) and OD_{ads} (from the CUSb/Oμ2) with the last group present with the lowest intensity in our SFG measurement. Comparisons of the frequencies resulting from both experimental data sets and the calculated frequencies are shown in Table 3. 6. Clearly, while the absolute calculated frequencies are a poor match to experiment, relative frequencies are in fair agreement. The agreement of relative, but not absolute, calculated harmonic normal mode frequencies with experiment is well known for molecules. We have observed it to be the case in OD fragments on the α-Al_2O_3(0001)[17] and (1-102)[16] surface previously as well.

Table 3. 6 Assignment of experimental observations to theory predictions.

Assignment		$\theta/\ °$	ν_{cal}	$\Delta\nu_{cal}$	ν_{exp}	$\Delta\nu_{exp}$
Inter-CUSa/Oμ2	OD_{surf}	36	2694		2762	
	OD_{ads}	44	2731	37	2812	50
CUSb/Oμ2	OD_{ads}	26	2785	91	2839	77

In the above, SFG spectra collected from samples with 0.14 and 0.05 eML coverages are discussed and the observed line shape modelled with three resonances characteristic of dissociatively adsorbed water.
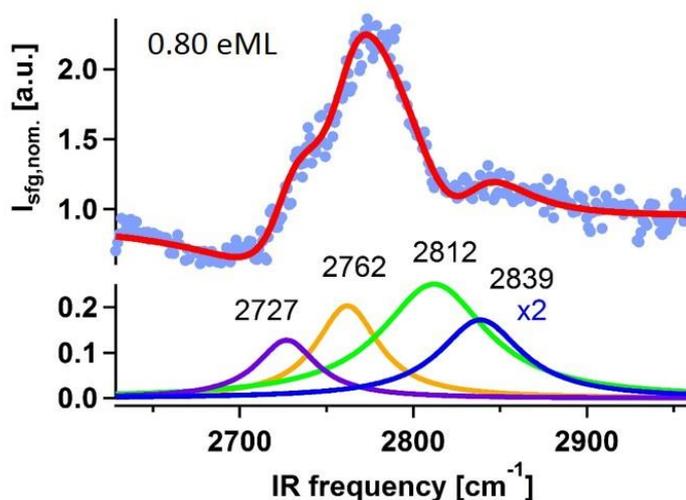
Figure 3. 14 SFG data of α-Al$_2$O$_3$(11-20) prepared with 0.8 ML D$_2$O and the extracted squared modulus of resonances are plotted below.

As discussed previously, both SFG spectra of the sample with a 0.80 eML water coverage as shown in Figure 3. 14 and the bend mode SFG spectra in Figure 3. 10

Figure 3. 10 Probing D2O bending vibrations with SFG on α-Al2O3(11-20) surface., suggest that there is both molecular and dissociative water adsorption at this coverage. As might be expected modelling of this spectrum required the three resonances appropriate for the lower coverages and a fourth, centered at 2727 cm^{-1} with phase=3.4±0.1, A=8.5±1.7 and Γ =29±3.8 characteristic of molecular water (under these conditions the phases and center frequencies of resonance 1, 2 and 3 are as shown in Table 3. 5 while Γ_1= 20.9±3.9, Γ_2= 22±3.4 and Γ_3= 37±2.1 cm^{-1}). The data analysis thus suggests that, at least for the three higher frequency resonances, the SFG spectral response is coverage independent (with the

exception of the amplitudes and the line width of resonance 3) from 0.8 to 0.05 eML. Such a coverage independent spectral response is most easily explained if SFG is probing well defined terrace sites.

3.4 Reactivity of α-Al₂O₃ surfaces towards dissociatively adsorbed water

Descriptions of water/metal oxide surface reactivity from coordination chemistry typically focus on the coordinative under saturation of individual surface metal and oxygen atoms to explain trends in macroscopic water reactivity [24-26]. Taking this work in conjunction with our previous efforts exploring the reactivity of small amounts of water with the α-Al₂O₃ (0001) and (1-102) surfaces allows us an opportunity to evaluate this heuristic for the reaction of small amounts of water with α-Al₂O₃ surfaces. The rate constant for water dissociation k_{diss} is calculated by using Eyring's transition state theory:

$$k(T) = \frac{k_B T}{h} \, e^{-\Delta G_{mol-diss}(T)/k_B T}$$

Here, h and k_B are Planck's and Boltzmann's constants, and $\Delta G_{mol\text{-}diss}$ is the activation free energy for the reaction path from molecular water to dissociative water. As shown in Table 3. 7, calculated rates of D_2O dissociation are higher for the (11-20) than for water on either the (0001) or (1-102) surfaces. From a surface oxygen perspective this trend in reactivity is consistent with textbook expectations: only the (11-20) surface contains $O\mu2$, i.e. doubly coordinated surface oxygens. From a surface aluminum perspective it does not appear to be so: (0001) surface Al atoms have lower coordination number (i.e. 3) than those of the other two surfaces (both are 5).

Table 3. 7 Coordination numbers of surface Al and O atoms, density of CUS Al atoms relative to the (1-102) surface, adsorption energies for the most stable molecularly and dissociatively adsorbed configurations, dissociation rates, and corresponding activation free energies (both at 300 K) for the most favorable terminations of the α-Al2O3 (0001), (1-102) and (11-20) surfaces.

Surface	(0001)	(1-102)	(11-20)
Coordination number Al; O	3; 3	5; 3,4	5; 2,3
Relative CUS density	2.13	1.00	5.45
$E_{ads\text{-}mol}$ (eV)	-1.4	-1.48	-1.78
$E_{ads\text{-}diss}$ (eV)	-1.81	-1.53	-2.3, -2.5
$\Delta G_{mol\text{-}diss}$ (eV)	0.11	0.12	0.002
$k_{diss,300K}$ (s^{-1})	8.0×10^{10}	5.2×10^{10}	5.8×10^{12}

As is clearly shown in Table 3. 7, the (11-20) surface differs from the others in the density of surface aluminum atoms. Crucially, on the one hand this high density of surface Al sites offers more sites for

water dissociative adsorption, on the other it also allows OD fragments to adsorb between two surface aluminums: bidentate adsorption. To summarize the above, only on the (11-20) surface can water dissociatively adsorb at inter-CUS sites. Obviously these inter-CUS sites enable the significant stabilization of the dissociated OD fragment, presumably because this oxygen is now covalently bound to two, rather than one, subsurface Al atoms. This work indicates that the ability of α-Al$_2$O$_3$ surface to form doubly coordinate surface OD fragments is essential to understand its reactivity with water and is highly dependent on crystal face. This insight is important in quantitative understanding of the reactivity of oxide surfaces with water more generally: the reactivity with water is not a linear function of density of uncoordinated surface metal atoms.

3.5 Conclusion

We investigated water adsorption on a stoichiometric oxygen terminated α-Al$_2$O$_3$(11-20) single crystal surface under low-coverage conditions both experimentally and theoretically. On this surface two types of unsaturated Al sites (CUSa and CUSb) and two types of O sites (Oμ2 and Oμ3) give rise to a large variety of structural alternatives for adsorbed water. Computationally we find that at low coverage (one water in 2x2 super cell) one type of molecularly, and six types of dissociatively adsorbed water (nearest neighbors) are possible. Among dissociatively adsorbed types we find that the configurations that keep OH and H fragments in close proximity and those that require Oμ2, rather than Oμ3, protonation are most favorable. In particular, we find the three most stable configurations to be the inter-CUSa/Oμ2 with $E_{ads-diss}$ = 2.50 eV, the CUSb/Oμ2 with $E_{ads-diss}$ = 2.28 eV, and the inter-CUSb/Oμ2 with $E_{ads-diss}$ = 2.09 eV at the PBE+D2 level of theory which is introduced in details in section 2.4 chapter2.

The theory results as previously discussed demonstrate that molecular water adsorption is kinetically unstable, dissociation is barrierless, and thus the dissociative adsorption of water is much more favorable under our experimentally realizable conditions. This prediction is in consistent with measured and computed SFG OD frequencies: resonances at 2766 and 2812 cm^{-1} in experiment, can be assigned to the stretching vibrations of OD$_{ads}$ and OD$_{surf}$ species from inter-CUSa/Oμ2 structure and one third resonance at 2839 cm^{-1} to the OD$_{ads}$ stretching vibration from CUSb/Oμ2 structure. Once formed, these species stay stable over days at low temperatures as 130 K or lower.

The calculation results also suggest the water reactivity of (11-20) is the highest due to its lower coordination number of surface O atoms (2-fold) and the higher density of the adsorption sites CUS Al as discussed above; but the reactivity of the (11-20) surface is dominated by its high adsorption site density which allows a new type of adsorption structure of OD fragments. While on both the (0001) and the (1-102) surfaces OD groups from dissociating water are only bound to a single surface Al (i.e., they

adsorb in a monodentate manner), on the (11-20) they can be bound to two surface Al atoms (i.e., bidentate adsorption), thus dramatically increasing the favorability of water dissociative adsorption.

3.6 References

1. Bolt, P.H., et al., *Interfacial reaction of NiO with Al$_2$O$_3$(11-20) and polycrystalline α-Al$_2$O$_3$.* Applied Surface Science, 1995. **89**(4): p. 339-349.

2. Bolt, P.H., et al., *The interaction of thin NiO layers with single crystalline α-Al$_2$O$_3$(11-20) substrates.* Surface Science, 1995. **329**(3): p. 227-240.

3. Kotula, P.G., et al., *Kinetics of thin-film reactions of nickel oxide with alumina: I, (0001) and (11-20)reaction couples.* Journal of the American Ceramic Society, 1998. **81**(11): p. 2869-2876.

4. Ago, N.I.H., *Crystal plane dependent growth of aligned single-walled carbon nanotubes on sapphire.* Journal of the American Chemical Society, 2008. **130**(30): p. 9918-9924.

5. Ago, H., et al., *Aligned growth of isolated single-walled carbon nanotubes programmed by atomic arrangement of substrate surface.* Chemical Physics Letters, 2005. **408**(4-6): p. 433-438.

6. Ishigami, N., et al., *Crystal plane dependent growth of aligned single-walled carbon nanotubes on sapphire.* Journal of the American Chemical Society, 2008. **130**(30): p. 9918-9924.

7. Shapovalov, V. and T.N. Truong, *Ab initio study of water adsorption on α-Al$_2$O$_3$(0001) crystal surface.* The Journal of Physical Chemistry B, 2000. **104**(42): p. 9859-9863.

8. Kijlstra, W.S., et al., *Inhibiting and deactivating effects of water on the selective catalytic reduction of nitric oxide with ammonia over MnOx/Al2O3.* Applied Catalysis B: Environmental, 1996. **7**(3): p. 337-357.

9. Rabung, T., et al., *Cm(III) sorption onto sapphire (α-Al$_2$O$_3$) single crystals.* The Journal of Physical Chemistry B, 2004. **108**(44): p. 17160-17165.

10. Catalano, J.G., *Relaxations and interfacial water ordering at the corundum (110) surface.* The Journal of Physical Chemistry C, 2010. **114**: p. 6624–6630.

11. Eng, P.J., et al., *Structure of the hydrated α-Al$_2$O$_3$(0001) surface.* Science, 2000. **288**: p. 1029−1033.

12. Sung, J., et al., *Surface structure of protonated R-sapphire (1-102) studied by sum-frequency vibrational spectroscopy.* Journal of the American Chemical Society, 2011. **133**(11): p. 3846-53.

13. Trainor, T.P., et al., *Crystal truncation rod diffraction study of the α-Al$_2$O$_3$(1-102) surface.* Surface Science, 2002. **496**: p. 238-250.

14. Tong, Y., et al., *Optically probing Al-O and O-H vibrations to characterize water adsorption and surface reconstruction on alpha-alumina: an experimental and theoretical study.* The Journal of Chemical Physics, 2015. **142**(5): p. 054704.

15. Wirth, J.S., P., *The chemistry of water on α-alumina: kinetics and nuclear quantum effects from first principles.* The Journal of Physical Chemistry C, 2012. **116**(51): p. 26829-26840.

16. Wirth, J., et al., *Characterization of water dissociation on α-Al$_2$O$_3$(1-102): theory and experiment.* Physical Chemistry Chemical Physics, 2016. **18**(22): p. 14822-32.

17. Kirsch, H., et al., *Experimental characterization of unimolecular ater dissociative Adsorption on α-alumina.* The Journal of Physical Chemistry C, 2014. **118**(25): p. 13623-13630.

18.   Elam, J.W., et al., *Adsorption of H_2O on a single-crystal α-$Al_2O_3(0001)$ surface.* The Journal of Physical Chemistry B, 1998. **102**(36): p. 7008-7015.

19.   Becker, T., et al., *Microstructure of the α-$Al_2O_3(11-20)$ surface.* Physical Review B, 2002. **65**(11).

20.   Hernandez, J., N. Uras, and J.P. Devlin, *Molecular bending mode frequencies of the surface and interior of crystalline ice.* The Journal of Chemical Physics, 1998. **108**(11): p. 4525-4529.

21.   Falk, M., *The frequency of the H-O-H bending fundamental in solids and liquids.* Spectrochimica Acta Part A: Molecular Spectroscopy, 1984. **40**(1): p. 43-48.

22.   Lambert, A.G., et al, *Implementing the theory of sum frequency generation vibrational spectroscopy: a tutorial review.* Applied Spectroscopy Reviews, 2005. **40**(2): p. 103-145.

23.   Zhuang, X., et al., *Mapping molecular orientation and conformation at interfaces by surface nonlinear optics.* Physical Review B, 1999. **59**(19): p. 12632-12640.

24.   Pauling, L., *The principles determining the structure of complex ionic crystals.* Journal of the American Chemical Society, 1929. **51**(4): p. 1010-1026.

25.   Hiemstra, T. and W.H. Van Riemsdijk, *Physical chemical interpretation of primary charging behaviour of metal (hydr) oxides.* Colloids and Surfaces, 1991. **59**: p. 7-25.

26.   Stumm, W., et al., *J. aquatic chemistry: chemical equilibria and Rates in natural waters*. 3rd ed. 1996, New York: Wiley-Interscience: New York.

Chapter 4 The desorption kinetics of water from α-Al$_2$O$_3$

As we have already introduced, the three most thermodynamic stable surfaces of α-Al$_2$O$_3$ are the C(0001), R(1-102) and A(11-20) planes. In chapter 3 we studied the structure of adsorbed water on the (11-20) surface in the low coverage limit both with SFG spectroscopy and theory.
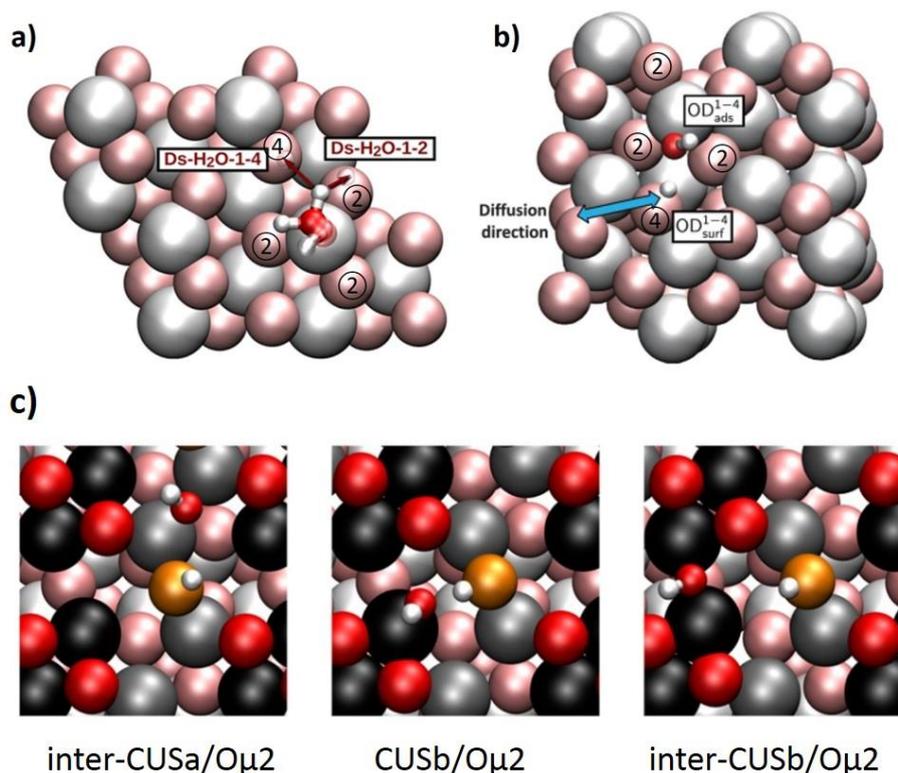
Figure 4. 1 Water adsorption structures on: a) α-Al$_2$O$_3$ (0001), b) α-Al$_2$O$_3$ (1-102) and c) α-Al$_2$O$_3$ (11-20)[1-4].

In both Chapter 3 and our previous studies[1-4] of the (0001) and (1-102) surfaces the same general approach was followed. That is, the structure of dissociatively adsorbed water was investigated experimentally using SFG spectroscopy to probe surface OH(OD) stretching vibrations and DFT calculations and, having demonstrated the self-consistency of theory and experiment, DFT calculations were used to quantify the thermodynamics and mechanism of water dissociative adsorption. For the (0001)[2] surface these efforts demonstrated that in UHV at low coverages water molecularly adsorbed at outmost Al atom sites with free adsorption energy E$_{ads-mol}$ = -1.4 eV and rapidly dissociated (in an essentially barrierless reaction) to the 1-2 and 1-4 adsorption structures (Figure 4. 1a). On the (1-102)[3] surface it was demonstrated by this approach that molecular adsorption was favorable, with E$_{ads-mol}$ = -1.48 eV, and subsequent dissociation, with structure 1-4 geometry (Figure 4. 1b), rapidly. As discussed in Chapter 3, for the O-I terminated (11-20)[1] surface we found water molecular adsorption to CUSb

Al sites to be favorable, $E_{ads-mol} = -1.78$ eV, and subsequent dissociation to three adsorption structures, the inter-CUSa/Oμ2, CUSb/Oμ2 and inter-CUSb/Oμ2, rapid (Figure 4. 1c).

The predicted adsorption structures have been proved to be correct by SFG measurement for all the three surfaces. As estimated by theory, the reactivity with water of these three surfaces is (11-20) > (1-102) > (0001) based on the free adsorption energy of dissociated forms $E_{ads-diss}$ (as listed in table 3.7). Both experiment and theory suggest that, for all surfaces at low coverages, water dissociation is favorable: molecularly adsorbed water tends to dissociate. However, the theoretical approach assumes a particular mechanism of adsorption (the clean surface and the one with adsorbate) which yields different results with varied mechanisms: rather than only one water dissociation is favorable, that with one molecular water catalyzed dissociation is more favorable[5]; besides, there can always be errors in theoretical estimations due to different theories and approximations used in calculation which yield different results in energy(e.g. two different exchange–correlation functions pure PBE and HSE06 result in different transition state for water dissociation). While it is important to experimentally check the validity of theoretical adsorption structure, it's also worthwhile to demonstrate with experiment approaches with respect to the predicted adsorption thermodynamics. In this chapter, we experimentally characterize water adsorption/desorption thermodynamics and kinetics and ask whether experimental observations of these quantities for all three surfaces agree with the estimates from theory.

To address this problem, we applied temperature-programmed desorption (TPD) spectra[6]. With this method, Nelson[7] et al. studied water desorption energy from α-Al$_2$O$_3$ (0001) surface and concluded it ranged from 23 to 41 Kcal/mol due to the possible defects. Perplexingly LEED patterns from their sample showed a well defined 1x1 pattern suggesting such a broad range of structural defects, if they exist, could not greatly perturb surface atomic order. As shown below, when appropriately calibrated TPD allows the determination of adsorbate coverage, desorption order and desorption energies for low water coverages on the α-Al$_2$O$_3$ (0001), (1-102) and (11-20) surfaces. The results of this approach find a trend of desorption energy on the three surfaces the same as theory: (11-20) > (1-102) > (0001). While validating the theoretical approach, this self-consistency also offers strong evidence that the desorption process is controlled by desorption of molecular water for all three surfaces.

4.1 Water coverage definition by TPD

To define the coverage of a sample water is first dosed onto the cleaned samples with our supersonic molecular beam source (MBS) through a nozzle heated to 850 K. We have previously demonstrated that dosing in this manner enhances water dissociative adsorption [8]. Purified D$_2$O was seeded by Helium and the stainless steel tubes between the nozzle and the reservoir heated to 340 K to minimize subsequent adsorption of D$_2$O on the tubes. Dosing was started at a sample temperature of 350 K and was stopped when the sample reached 135 K following cooling at 100 K/min. In this way, an ice multilayer is formed

on the surface of α-Al_2O_3. Differing amounts of water are then removed by flashing the sample to higher temperature with a heating rate of 100 K/min and subsequent cooling to 135 K (by repeating the experiment with different maximum temperatures the water surface coverage is controlled). The TPD measurement was carried out beginning with the cooled sample, and monitoring Mass 20 (D_2O) while the sample is heated to 700 K with a heating rate of 100 K/min.
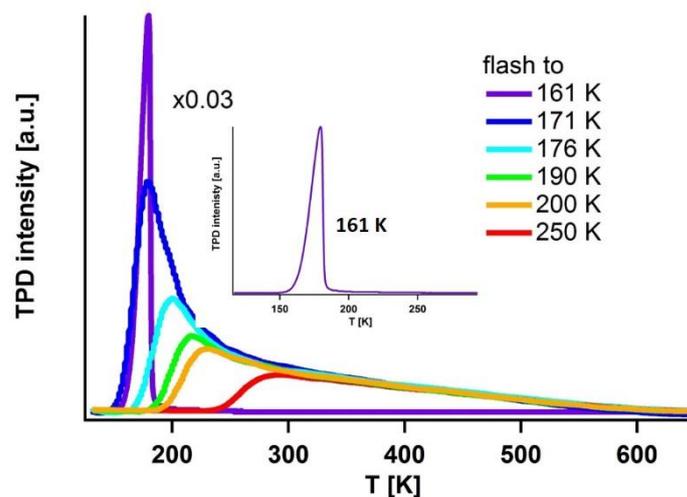
Figure 4. 2 TPD spectra collected on α-Al_2O_3 (11-20) surface, 100 K/min, mass 20

Table 4. 1 Relative coverage of D_2O on α-Al_2O_3 (11-20) that flashed to different temperatures

flash T/K	176	190	200	250
θ/eML	1.00	0.80	0.75	0.50

Figure 4. *2* shows the resulting series of TPD spectra of desorbed D_2O from α-Al_2O_3(11-20) samples that were flashed to maximum temperatures between 161 and 250 K. The TPD curve collected from the sample flashed to 161 K is quite intense and has a shoulder to lower temperature. This should is absent in TPD spectra collected from samples annealed to 171 K and higher. As discussed in chapter 3 and also in our previous work, the TPD 161 K spectrum is dominated by the desorption from D_2O ice multilayers (its asymmetric feature towards lower temperatures is characteristic of the zero[th] order desorption expected in this system). The TPD collected from samples flashed to 171 K and above are much less intense and dominated by a shoulder towards higher temperatures suggesting the desorption order has changed and water is presumably now adsorbed on the surface at ~ monolayer coverages. Closer examination of the TPD spectra of the sample flashed to 171 K suggests that it shows an additional feature centered at 200 K. Incrementally reducing coverage, flashing the sample to 176 K, leads to a

TPD spectrum with a maximum at 200 K and decreased intensity and the same longer shoulder extending to high temperature. These differences are most easily rationalized if the feature at 200 K results from the desorption of multilayer water and flashing the sample to temperatures between 171 and 176 K, although clearly close to 176 K, produces a monolayer. In this study we assumed that the 176 K spectra captures the monolayer (we defined it as 1.0 eML, which is experimentally defined monolayer) of D_2O desorption from α-Al_2O_3 (11-20) surface.

By integrating the area under the TPD spectra and compare it with that of TPD 176 K, we calculate the relative coverage (**θ**) of each sample. As shown in Table 4.1 it is 0.8 eML, 0.75 eML and 0.5 eML for samples annealed to 190 K, 200 K and 250 K.
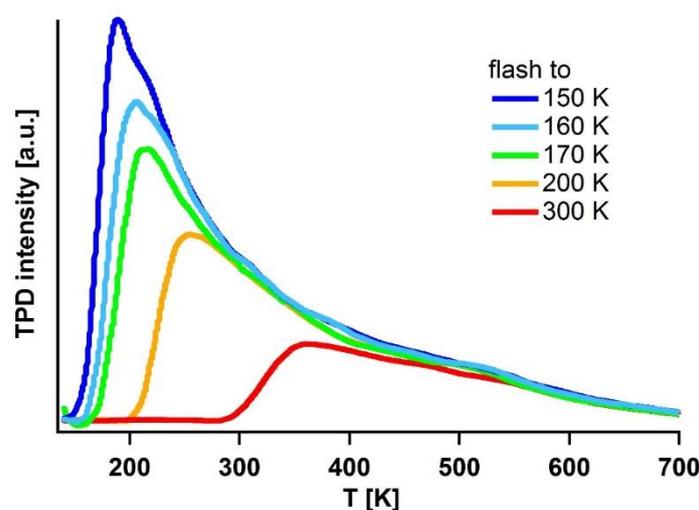
Figure 4. 3 TPD spectra collected on α-Al_2O_3 (1-102) surface, 100 K/min, mass 20

Table 4. 2 Relative coverage of D_2O on α-Al_2O_3 (1-102) flashed to different temperatures

flash T/K	160	170	200	300
θ/eML	1.00	0.87	0.67	0.30

We defined a monolayer of adsorbed D_2O on the α-Al_2O_3 (1-102) surface similarly. Figure 4. 3 shows the TPD results that are collected at flash temperatures 150 K, 160 K, 170 K, 200 K and 300 K. Similarly to samples annealed to 171 K and higher on the (11-20), TPD spectra of samples flashed to 150 K and higher on the (11-02) are all dominated by a long shoulder towards higher temperatures. Additionally, the sample flashed to 150 K has a clear feature centered at 210 K that significantly decreases in intensity for the sample flashed to 160 K and disappears for the sample flashed to 170 K. These observations are most straightforwardly rationalized if the 210 K feature is the result of multilayer desorption and the

samples flashed to 150 K and higher show only monolayer desorption. In this scenario a sample flashed to temperatures between 160 and 170 K, although clearly much closer to 160, results in monolayer coverage of adsorbed water on the (1-102) surface. Therefore we take the 160 K spectrum as the desorption of water monolayer and calculate the initial coverage of samples flashed to 170 K, 200 K and 300 K by integrating the spectra area and normalizing. This approach suggests such temperature treatments result in samples with 0.87 eML, 0.67 MeL and 0.30 eML surface coverages respectively.
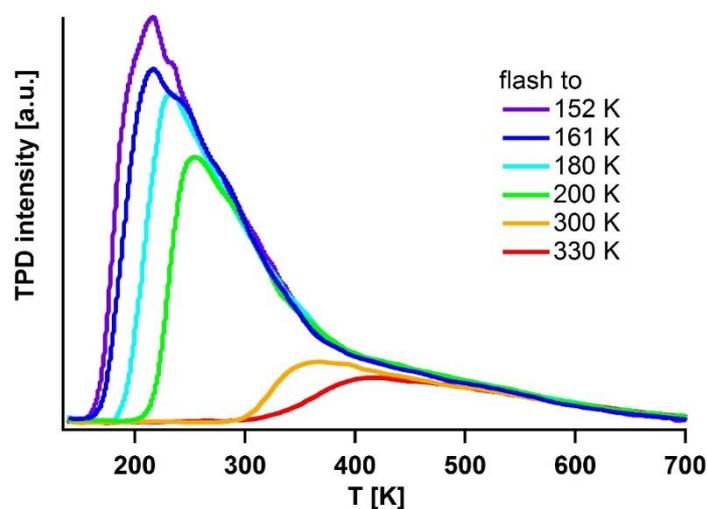
Figure 4. 4 TPD spectra collected on α-Al$_2$O$_3$ (0001) surface, 100 K/min, mass 20

Table 4. 3 Relative coverage of D$_2$O on α-Al$_2$O$_3$ (0001) flashed to different temperatures

flash T/K	180	200	300	330
θ/eML	1.00	0.82	0.26	0.20

Finally, the data shown in Figure 4. 4 were employed to define a monolayer water coverage of D$_2$O on the α-Al$_2$O$_3$(0001). As clearly shown, in the sample flashed to 152 K a shoulder feature appears around 235 K, that presumably originates from the desorption of a water monolayer, while the lower temperature region is from the desorption of water multilayer. Slightly increasing the flashing temperature to 161 K, leads to decrease in TPD intensity as expected but still shows a desorption from both multi- and mono-layer while TPD. The sample flashed to 180 K clearly no longer shows the multilayer desorption feature. The temperature increasing effect is not a constant, thus it is difficult to prepare samples that flashed to temperatures with small difference as 10 K. Due to the delay between the heating set up and feedback of the temperature read out, it is always difficult to flash the sample to

exactly the set point,: e.g. the heating was set up to 170 K, when the heating device stopped its current supply, the sample temperature still increased gradually by several kelvin to 176 or even 180 K. That is the reason why there is no TPD curve of samples that flashed to 165 K, 170 K and 175 K or with even smaller temperature change. Thus we take the spectrum collected of samples that flashed to 180 K as monolayer desorption, and the relative initial coverage of all the other spectrums can be calculated based on this: it is 0.82 eML, 0.26 eML and 0.20 eML water initial coverage of samples that flashed to 200 K, 300 K and 330 K, respectively.

For all the three surfaces, the error of the definition of monolayer should be within ±5% eML due to the mis-assignment of monolayer by 2-5 K (flashing temperature).

4.2 TPD data analysis

As introduced earlier, there are several commonly applied methods for TPD data analysis[6, 7, 9-11]. The suitability of a particular method depends on what kind of data you have (e.g. one spectra or series, heating rate dependence measurement or not) and the extent of your independent knowledge of the mechanism of desorption (i.e. desorption order) you may obtained from approaches other than TPD. In this study we have a series of TPD spectra for each surface, collected from samples, of different coverage and a desorption mechanism that we expect (from theory results) to be unimolecular desorption (the validity of this assumed mechanism in the experimental data analysis is discussed below). Given these results we being our data analysis with the Polyani-Wigner equation in which desorption rate $r(\theta)$ is expressed as:

$$r(\theta) = \frac{\nu(\theta)}{\beta} \theta^n \exp^{(-E(\theta)/RT)} \qquad 4.1$$

and $\beta(K \cdot s^{-1})$ the heating rate for TPD measurement, θ the coverage of adsorbate, n the kinetic desorption order, R the gas constant and $\nu(\theta)$ (s^{-1}) is pre exponential factor which may be a function of coverage, $E(\theta)$ the desorption energy which is also a function of coverage. While fitting our data with this expression suggests and it can be compared to the theory if the desorption process is dominated by one single rate determining step while if not it should be a weighted average energy of all elementary steps.

$E(\theta)$ will linearly decrease with increasing surface coverage for a system in which there are pairwise repulsive interactions between adsorbate species [11-13] while it will increase along coverage if the interaction is pair-attractive. The parameter c in equation *4. 2* presents the interaction strength and is positive for repulsive interaction. Our prior theoretical and experimental work[1-4] suggests water dissociatively adsorbed on the surface at low coverages to form OD_{ads} and OD_{surf} groups (or OH, as described in chapter 3) which possess similar electronic properties, such a model is appropriate for these adsorption systems:

$$E(\theta) = E_0 - c \cdot \theta \qquad\qquad 4.\,2$$

Where E_0 is desorption energy in the limit of zero surface coverage. The coverage dependence of ν can be expressed by the well-known compensation effect[14, 15] which is empirical function extracted by plotting $\ln \nu(\theta)$ vs. $E(\theta)$:

$$\ln \nu(\theta) = \ln\nu_0 + \frac{\Delta E(\theta)}{RT_c} \qquad\qquad 4.\,3$$

where ν_0 is the pre-exponential factor at coverage zero, which is also called 'attempt to escape frequency', and is generally assumed to have a frequency slightly less than that of vibrations of atoms/ions of the medium[16], $\Delta E(\theta)$ is the coverage dependent part of E and T_c is the compensation effect temperature[14] which has a clear physical interpretation that it represents the temperature at which the Arrhenius plots ($\ln r$ vs. $1/T$) for different adsorbate coverages intersect. Since in this work we focused on TPD data collected from samples with quite low initial coverage (<0.1 eML), $\Delta E(\theta)$ is small while T_c is relatively high[14] (~1000 K for some material). Because the resulting surface coverage dependence of ν is expected to be small, we take it as constant in all our data analysis [14, 15].

With the initial guess of all the parameters in equation 4. 1 and 4. 2 (pre-factor ν, desorption order n, constant c and E_0), we globally fit a series of TPD data sets with different initial coverages on the same crystal surface. The fitting optimization is achieved by minimizing the difference between model and data.

4.3 Dissociative water desorption studied with TPD spectra

Previous work [1-4] have shown that water dissociatively adsorbs on the α-Al$_2$O$_3$ (0001), (1-102) and (11-20) surfaces at relatively low coverages in UHV. However the energetics of this adsorption has been substantially less well studied. Here we apply TPD to study water desorption kinetics (and thermodynamics) from the three most thermodynamically stable surfaces α-Al$_2$O$_3$ surfaces.

To study the desorption kinetics and thermodynamics of dissociatively adsorbed water, and to compare more straightforwardly with theory, it would be easiest to prepare samples with only dissociatively adsorbed water. From our groups previous studies [1-4], and the results presented in chapter 3, we know that dissociative water adsorption is favored at coverages below 0.15 eML. To achieve several such low coverage samples, the amount of water adsorption must be carefully controlled. The sample preparation method as described in section 4.1, i.e. water is dosed from 350 K to 135 K and then the surface is heated up to high temperatures, is problematic in this regard because it always creates a small background adsorption signal in the TPD spectra. During the temperature flashing step the sample stage is cold relative to the sample. When a TPD measurement is carried out desorption of this water from the sample stage occurs contributing a background that is noticeable in the high temperature, low signal, part of the

curve. We adopted this dosing procedure because, when performing optics measurements, it is convenient to align our SFG spectrometer on the OH stretch signal from the ice surface. It is further worth noting that this background is not significant for the definition of a monolayer, here the signal is quite intense. However, if we desire, as we do here to perform TPD measurements on samples with low water coverage the size of the background becomes similar to the size of the signal we are trying to measure.
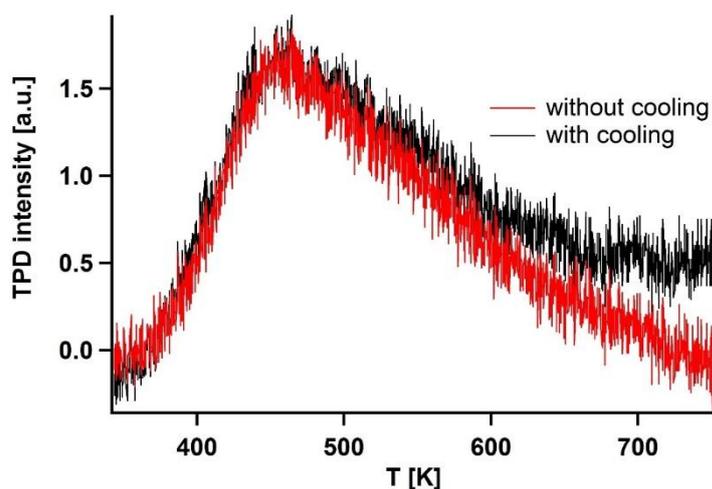
Figure 4. 5 TPD curve of samples that prepared with cooling and without cooling system: both flashed to the same temperature

To solve this problem, we here dosed D_2O on the crystal surface still by MBS with a sample temperature of 300 K (room temperature without LN_2 cooling) for 5 min and then to generate other samples with lower coverage by flashing the sample to temperatures higher than 300 K (stay for 1 min) then let the sample cool down naturally. Without LN_2 cooling, the sample holder is at room temperature and thus very little water adsorbs on it. The difference between TPD results from samples that have been flashed to the same temperature with and without cooling is shown in Figure 4. 5. Clearly the sample prepared at room temperature with LN_2 cooling of the sample holder has a high temperature tail while that with the sample holder at room temperature does not. Because we are interested only in desorption energies from low coverage samples, given the room temperature dosed samples, whose coverage may be decreased further by higher temperature flashing, we then also collect TPD spectra starting from room temperature. After collecting the TPD the initial coverage of each sample is calculated by integrating the spectra area and compare that with the monolayer spectra as defined in section 4.1. As we discussed above that definition of the monolayer area also includes a tiny amount of background adsorption. Comparisons of the sort of data plotted in Figure 4. 5 suggest this leads to an error of less than 2% eML. As we shown in detail below uncertainties in initial coverage of this size (and larger!) do not significantly effect the desorption energies we infer from the data.

Figure 4. 6 shows TPD spectra from three samples low coverage samples prepared using the approach described above for D_2O adsorption on the α-Al$_2$O$_3$(11-20) surface. The initial coverage of these three TPD curve are 0.09 eML (green), 0.06 eML (yellow) and 0.05 eML (red), respectively. Clearly, the peak maximum shifts to higher temperatures with decreasing initial coverage. Such a shift is opposite that expected from a 0th order desorption process (e.g. multilayer adsorption)[17]. It is also not expected for desorption that is 1st order where the peak maximum is expected to be independent of initial coverage[18]. As discussed above, at the initial water coverages of the samples from which TPD spectra are collected in Figure 4. 6, we expect adsorbed water to be dominated by dissociatively adsorbed species. In the TPD process, water desorbs molecularly (mass 20 of D_2O is detected in this work): the dissociated water species will combine into molecular water and then desorb from the surface and the desorption rate might be expected to be proportional to the square of the coverage ($D(\theta)+OD(\theta)=D_2O(\theta)$). For such a second order desorption, the TPD peak maximum shifts to higher temperatures with decreasing initial coverages [19] and all the curves share the edge at high temperature. This qualitative shape of the TPD signal is clearly observed in Figure 4. 6 for desorption from the (11-20) surface and below for desorption from the (1-102) and (0001). We thus assume, for all modeling of the TPD data, the desorption order is two.
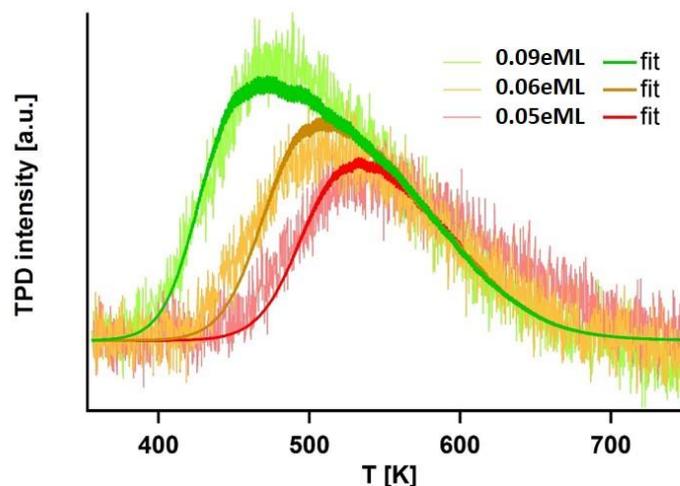
Figure 4. 6 TPD spectra of D_2O desorbed from α-Al$_2$O$_3$(11-20) surface, β=1 K/s, mass 20

Within our model E_0 is, defined to be, independent of surface coverage. While both the constant factor c and pre exponential factor ν may in principle be coverage dependent we are interested in simultaneously describing TPD spectra whose initial coverages differ by only 0.05 eML. For such small ranges of surface coverage we expect neither the type of interaction between adsorbates, c, or the mechanism of desorption, related to ν, to change. We thus assume all three quantities are independent of coverage and globally fit the three TPD curves. The fitting results are plotted in thick solid line in Figure 4. 6 where a good overlapping between TPD spectra and fitting is obtained. The fitting result is not smooth because we solve the model numerically with changing coverage at each temperature:

essentially the fit result inherits some of the experimental noise. As a result of this global fitting, the desorption energy at coverage zero, i.e. the unimolecular desorption energy of D_2O from α-Al$_2$O$_3$(11-20), is found to be 1.52 eV -- and pre exponential factor after optimization equals to 1.05×10^{13} s^{-1} as listed in Table 4.4.
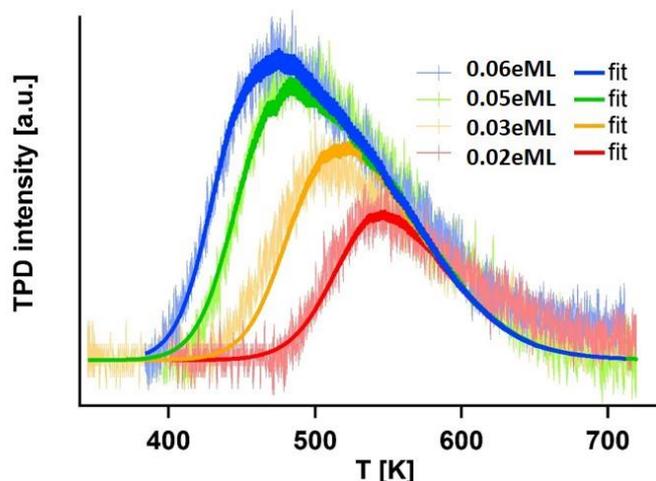
Figure 4. 7 TPD spectra of D_2O desorbed from α-Al$_2$O$_3$(1-102) surface, β=1 K/s, mass 20

TPD spectra of D_2O adsorbed α-Al$_2$O$_3$(1-102) surfaces with low initial coverages are shown in Figure 4. 7. Clearly the TPD curves also show a distinct shift to higher temperatures with decreasing surface coverage: desorption is likely 2nd order. By integrating the area under the curves and comparing it with the monolayer definition for this surface discussed above, we find the initial coverage of each sample to be 0.06 eML (blue), 0.05 eML (green), 0.03 eML (yellow) and 0.02 eML (red). Again, all the four data sets are globally fit with equation 4. 1 and 4. 2.The fit results (in thick lines) follow the shape of TPD data well, converging as expected at high temperatures. The resulting E_0 is 1.42 eV for unimolecular D_2O desorbed from α-Al$_2$O$_3$(1-102) while the pre frequency factor is 0.47×10^{13} s^{-1} as listed in Table 4. 4.
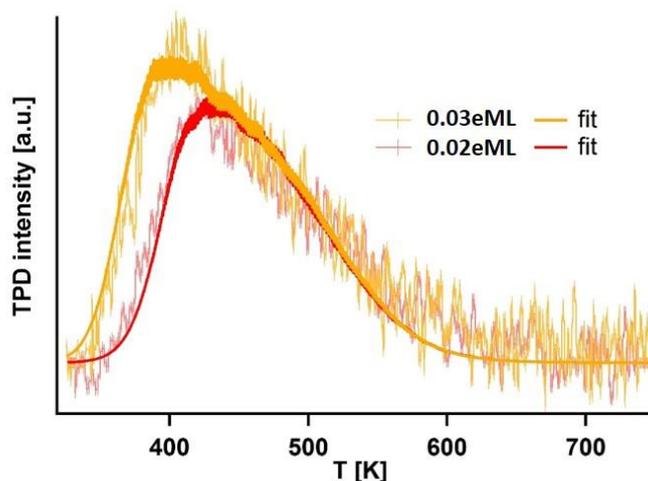
Figure 4. 8 TPD spectra of D_2O desorbed from α-Al$_2$O$_3$(0001) surface, β=1 K/s, mass 20

Dosing at 300 K on the α-Al$_2$O$_3$(0001) produces much smaller amount of adsorbed water than for the α-Al$_2$O$_3$(11-20) and (1-102) surfaces. This observation is consistent with theory and our prior experimental work that suggests the (0001) is the most unfavorable surface for water adsorption[1, 20]. These lower reactivity makes creating a series of low coverage samples substantially more challenging: following the approach described above, and given the limitations of fine sample temperature control in our system, we cannot flash the sample to a series of higher temperatures and still retain significant adsorbed water mass. Therefore, on this surface only two TPD data sets with initial coverage 0.02 and 0.03 eML are collected each with relatively low maximum intensity and relatively low signal to noise (see Figure 4. 8). However, it still suggests a second order desorption of water from this surface with peak maximum temperature shifts towards higher temperature at lower initial coverage. By applying the Polanyi-Wigner equation for simulation of these two data sets again, E_0 is found to be 1.28 eV (Table 4. 4) for water desorption from α-Al$_2$O$_3$(0001), the lowest among these three surfaces.

Table 4. 4 Simulation parameters for all the three surfaces

	α-Al$_2$O$_3$(11-20)	α-Al$_2$O$_3$(1-102)	α-Al$_2$O$_3$(0001)
ν/s^{-1}	1.05 e+13	0.47 e+13	1.00e+13
c/eV	3.68	4.23	10.42
E_0/eV	1.52	1.42	1.28

Since the definition of monolayer will affect the calculation results of initial coverage which may change the fitting results, it is necessary to evaluate any uncertainty in E_0 whose origin lies in this definition. We did so by defining a monolayer whose total area varied by $\pm 10\%$ of that defined in section 4.1, which is both much larger than the error caused by background desorption (less than 2%) and larger than the error by mis-assignment of the monolayer (within $\pm 5\%$ eML). With this assumption, we re-do the global fitting of TPD over each of the three surfaces with the same simulation procedure as applied above.

Table 4. 5 Simulated parameters of TPD data on α-Al$_2$O$_3$(11-20)

α-Al$_2$O$_3$ (11-20)			
monolayer	176K as eML	+10% as eML	-10% as eML
ν /s^{-1}	1.05 e+13	1.01 e+13	0.93 e+13
c	3.53 e+5	3.49 e+5	3.62 e+5
E_0 /eV	1.52	1.50	1.54

Table 4. 6 Simulated parameters of TPD data on α-Al$_2$O$_3$(1-102)

α-Al$_2$O$_3$ (1-102)			
monolayer	160K as eML	+10% as eML	-10% as eML
ν /s^{-1}	0.47 e+13	0.55 e+13	0.43 e+13
c	4.06 e+5	4.05 e+5	4.08 e+5
E$_0$ /eV	1.42	1.40	1.44

Table 4. 7 Simulated parameters of TPD data on α-Al$_2$O$_3$(0001)

α-Al$_2$O$_3$ (0001)			
monolayer	180K as eML	+10% as eML	-10% as eML
ν /s^{-1}	1.00e+13	0.98 e+13	0.66 e+13
c	10 e+5	9.49 e+5	10.74 e+5
E$_0$ /eV	1.28	1.25	1.31

The results of this reanalysis are shown in Table 4. 5, Table 4. 6 and Table 4. 7 for the α-Al$_2$O$_3$(11-20), α-Al$_2$O$_3$(1-102) and α-Al$_2$O$_3$(0001) surfaces, respectively. It is clear that the uncertainty such errors introduce in the desorption energies inferred from the TPD analysis is small. In particular, we estimate that E$_0$ is 1.52±0.02 eV on α-Al$_2$O$_3$ (11-20), 1.42±0.02 eV on α-Al$_2$O$_3$ (1-102) and 1.28±0.03 eV on α-Al$_2$O$_3$ (0001).

4.4 Compare E$_0$ with theory prediction
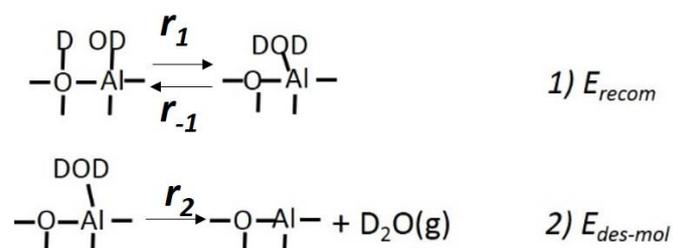
Figure 4. 9 Sketch of the steps of 2nd order desorption of dissociated water species from α-Al$_2$O$_3$

A lot of effort has been made on theoretical prediction of water adsorption on α-Al$_2$O$_3$[1, 3, 4, 21, 22]. In particular, previous studies[1-4] from our group have found by performing periodic first-principles total energy calculation at PBE+D2 level of theory, that a single water molecule adsorption energy $E_{ads-mol}$ is 1.78, 1.48 and 1.40 eV on α-Al$_2$O$_3$ (11-20), (1-102) and (0001) surface, respectively. Using a nudged elastic band with Climbing Image (CI) method, this work find that the dissociation of surface bound molecular water is essentially barrierless (especially on (11-20)) with $E_{ads-diss}$ is 2.27, 1.53 and 1.45 eV on these three surfaces, respectively. In the desorption process for the dissociated water from α-Al$_2$O$_3$, it is a 2nd order desorption process as already being discussed previously based on the TPD peak shift vs. initial coverage. During desorption one might imagine three possible reactions: (i) the dissociated water species recombined into molecularly adsorbed water (with rate r_1) (ii) this molecular water dissociates (with rate r_{-1}) and (iii) this molecularly adsorbed water desorbs (with rate r_2). In this view r_2 is the desorption rate $r(\theta)$ in equation 4. 1 that (since as being discussed in chapter 2, the pump speed is fast enough to pump away the water in gas phase once it formed, thus we assume there is no re-adsorption of desorbed water from the gas phase). The dissociated water species get recombined into water molecule firstly where it needs to overcome the energy difference from dissociated state to transition state that we name it as E_{recom}; at the same time, the newly formed molecular water on the surface will get dissociated with energy barrier E_{diss} which is quite tiny[1-3] that could be considered as 0; for the step that the molecular water desorbs from the surface to the gas phase it needs to overcome the energy difference (we label it as $E_{des-mol}$) between molecularly adsorbed structure to the free water in gas phase and the bare surface of α-Al$_2$O$_3$ (because there is no transition state for this transformation). Therefore the desorption mechanism can be written:

$$r_1 = \nu(\theta)\theta^2 e^{-E_{recom}/RT}$$

$$r_{-1} = \nu(\theta)M e^{-E_{diss}/RT}$$

$$r_2 = r(\theta) = \nu(\theta)M e^{-E_{des-mol}/RT}$$

4. 4

Where M is the coverage of molecularly adsorbed D$_2$O. At the beginning of desorption process, $r_1 \gg r_{-1}$ (and r_2) due to the small M. Thus M is accumulated and r_{-1} and r_2 goes up. When $r_{-1} \approx r_1 \gg r_2$ (we assume step 1 was close to be equilibriumed), it can solve for $r(\theta)$ with equation 4. 5:

$$r(\theta) = \nu(\theta)\theta^2 e^{-(E_{recom}+E_{des-mol}-E_{diss})/RT} \qquad 4. 5$$

which shows the desorption energy should be comparable with the theory predicted value $E_{recom}+E_{des-mol}-E_{diss}$.

Table 4. 8 lists the theoretical $E_{des-mol}$, E_{recom} and E_{diss} in eV of water desorption from α-Al$_2$O$_3$(11-20), (1-102) and (0001) surface, respectively. $E_{recom}+E_{des-mol}-E_{diss}$ is 2.27, 1.53 and 1.45 eV on these three surfaces, respectively. This indicates in the theory water dissociative adsorption on (11-20) surface is the most stabilized, following by that on (1-102) surface while water on (0001) is easiest to desorb. Thus in the following discussion, I compare the experimentally observed desorption energy for uni-molecular water E_0 with this theoretically predicted value $E_{recom}+E_{des-mol}-E_{diss}$.

Table 4. 8 Theoretically predicted recombination energy E_{recom} (energy difference between dissociated structure to transition state of this step) and the molecular desorption energy $E_{des-mol}$ of water from α-Al$_2$O$_3$ and E_{diss} the energy barrier to overcome to dissociated (for the calculation, uni-molecular water was put onto 2x2 supercell) [1, 3, 4]

surface	$E_{des-mol}$ /eV	E_{recom} /eV	E_{diss} /eV	$E_{recom}+E_{des-mol}-E_{diss}$ /eV
(0001)	1.40	0.17	0.12	1.45
(1-102)	1.48	0.1	0.05	1.53
(11-20)	1.78	0.5	0.01	2.27

The unimolecular water desorption energy E_0 obtained through TPD experiment by employing Polanyi-Wigner equation for data simulation as discussed in section 4.3 is 1.52, 1.42 and 1.28 eV on α-Al$_2$O$_3$(11-20), (1-102) and (0001) surface. There is a good consistence on the order from the highest to the lowest desorption energy between theory and experiment as plotted in Figure 4. 10. Both TPD experiment and DFT calculation suggest water dissociative adsorption at low coverage on (11-20) is the most thermodynamically and kinetically favored while (0001) surface is the last.

The desorption energy obtained in experiment agrees well with theory especially on (1-102) and (0001) surfaces. However, it seems the difference between experiment and theory of desorption energy on (11-20) surface is relatively large. Because on this surface, besides structure CUSb/Oμ2 for water dissociation, water even more favorably dissociated at structure inter-CUSa/Oμ2, but the adsorption kinetics of which is unclear in theory. Theory predicted water adsorption kinetics on (11-20) surface does not exactly reflect the desorption kinetics, or say desoption kinetics doesnot necessarily follow the adsorption way(more details see section 3.2 and 3.4).
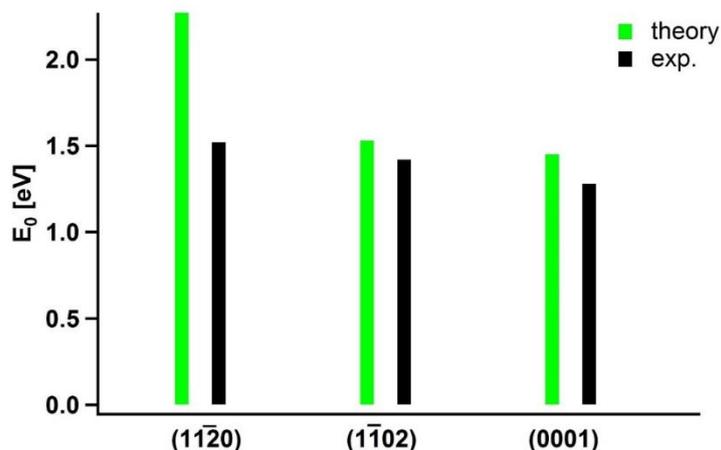
Figure 4. 10 Comparison of desorption energy E_0 and calculated unimolecular adsorption energy E_{ads}

4. 5 Conclusion

The thermodynamics of dissociated water desorption form α-Al_2O_3(11-20), (1-102) and (0001) surfaces, were investigated by TPD. With careful evaluation the drawbacks on different popular ways for data simulation, a procedure based on Polanyi-Wigner equation is conducted to TPD data sets in this work. It gives more reliable results on the desorption energy as it accounts for each data point with global fitting to several data sets and behaves well for a second order desorption process where desorption energy E is a function of coverage. The unimolecular water desorption energy, E_0, obtained by analysis of TPD data in this manner is 1.52, 1.42 and 1.28 eV from the α-Al_2O_3(11-20), (1-102) and (0001) surfaces, respectively. This result is consistent with prior theoretical efforts that find desorption energies of water from the three surfaces are in the order (11-20)>(1-102) >(0001).

The results of this study of desorption thermodynamics and kinetics of water from α-Al_2O_3 with TPD, are experimental conformation of qualitative reactivity trends predicted from theory, i.e. the O-I terminated (11-20) is the most reactive, followed by the O-terminated (1-102) followed by the Al-I terminated (0001) surface, for low water coverages on the three most thermodynamically stable α-Al_2O_3 surfaces. More quantitatively the close correspondence between the E_0 extracted from experiment and the desorption energy of molecular water is consistent with the general picture of water reactivity presented by theory on all surfaces. That is, molecular water adsorbs and rapidly dissociates. While dissociation is favorable the energy gain on dissociation is small relative to the adsorption energy of molecular water.

In particular, the close correspondence between our measured desorption energy and the theoretical values predicted for the ideal (0001) surface place tight limits on the effect of surface structural defects on water reactivity for the well prepared 1x1 clean α-Al_2O_3 surface. In Nelson's work[7], they concluded

that water desorption energy dropped in the range 23-41 Kcal/mol due to the adsorption at defects on the surface by simulation the TPD data with Reahead's peak maximum method which is applicable for 1st order desorption data analysis. They observed a series of TPD spectra with peak maximum shifting to higher temperatures as the coverage decreased which should be the feature of 2ed order desorption process thus could not be analyzed with Reahead's peak maximum method.

One of the challenges in quantitative interpretation of TPD data is that it is typically collected over a wide range of surface coverages. As a result comparison of peaks observed in TPD to theory requires the, often computationally expensive, structure of high coverages systems and the phase transitions that occur as coverage is decreased. Here we avoid this problem by collecting TPD spectra only for samples with relatively low initial coverages where theoretical descriptions of surface structure are straightforward. Nevertheless we demonstrate that, because we collect several independent TPD spectra for each surface, extraction of model parameters with relatively high certainty just from experiment is possible. The resulting self-consistency of experiment and theory suggests one might confidently proceed to higher coverages and more complex solid/water interactions. Since the problem of water reactivity with relatively complex dielectric materials is quite general we expect this approach to offer quite valuable foundations for a wide variety of solid/water studies.

4.6 References

1.   Heiden, S., et al., *Water dissociative adsorption on α-Al$_2$O$_3$(11-20) is controlled by surface site undercoordination, density, and topology.* The Journal of Physical Chemistry C, 2018. **122**(12): p. 6573-6584.

2.   Kirsch, H., et al., *Experimental characterization of unimolecular water dissociative adsorption on α-alumina.* The Journal of Physical Chemistry C, 2014. **118**(25): p. 13623-13630.

3.   Wirth, J., et al., *Characterization of water dissociation on α-Al$_2$O$_3$(1-102): theory and experiment.* Physical Chemistry Chemical Physics, 2016. **18**(22): p. 14822-32.

4.   Wirth, J.S., P., *The chemistry of water on α-alumina: kinetics and nuclear quantum effects from first principles.* The Journal of Physical Chemistry C, 2012. **116**(51): p. 26829-26840.

5.   Hass, K., et al., *The chemistry of water on alumina surfaces: reaction dynamics from first principles.* Science, 1998. **282**: p. 265-268.

6.   de Jong, A.M. and J.W. Niemantsverdriet, *Thermal desorption analysis: comparative test of ten commonly applied procedures.* Surface Science, 1990. **233**(3): p. 355-365.

7.   Nelson, C.E., et al., *Desorption of H$_2$O from a hydroxylated single-crystal α-Al$_2$O$_3$(0001) surface.* Surface Science, 1998. **416**(3): p. 341-353.

8.   Kirsch, H., *Chemical reactions on surfaces-a SFG study*. 2014, Freie Universitaet Berlin.

9.   Elam, J.W., et al., *Adsorption of H$_2$O on a single-crystal α-Al$_2$O$_3$(0001) surface.* The Journal of Physical Chemistry B, 1998. **102**(36): p. 7008-7015.

10.   Tokora, Y., et al., *Analysis of thermal desorption curves for Heterogeneous Surfaces: a liear variation of the energy of desorption.* Bulletin of the chemical society of Japan, 1978. **51**: p. 85-89.

11.   Chan, C.M., R. Aris, and W.H. Weinberg, *An analysis of thermal desorption mass spectra. I.* Applications of Surface Science, 1978. **1**(3): p. 360-376.

12.   Falconer, J.L., et al., *Flash desrption activation energies: DCOOH decompositon and CO desorption from Ni (110).* Surface Science 1975. **48**: p. 393-405.

13.   Koppers, J., et al., *Evaluation of flash desorption spectra.* Surface Science 1984. **138**: p. L147-L150.

14.   Niemantsverdriet, J.W., K. Markert, and K. Wandelt, *The compensation effect and the manifestation of lateral interactions in thermal desorption spectroscopy.* Applied Surface Science, 1988. **31**(2): p. 211-219.

15.   Niemantsverdriet, J.W., et al., *Thermal desorption of strained monoatomic Ag and Au layers from Ru(001).* Journal of Vacuum Science & Technology A, 1987. **5**(4): p. 875-878.

16.   Sunta, C.M., *Unraveling thermoluminescence.* 2014: Springer.

17.   Hendewerk, M., M. Salmeron, and G.A. Somorjai, *Water adsorption on the (001) plane of Fe2O3: an XPS, UPS, Auger, and TPD study.* Surface Science, 1986. **172**(3): p. 544-556.

18.   D'Evelyn, M.P., et al., *Surface π bonding and the near-first-order desorption kinetics of hydrogen from Ge(100)2×1.* The Journal of Chemical Physics, 1993. **98**(4): p. 3560-3563.

19.   Stirniman, M.J., et al., *The adsorption and desorption of water on single crystal MgO(100): the role of surface defects.* The Journal of Chemical Physics, 1996. **105**(3): p. 1295-1298.

20.   Tong, Y., et al., *Optically probing Al-O and O-H vibrations to characterize water adsorption and surface reconstruction on alpha-alumina: an experimental and theoretical study.* The Journal of Chemical Physics, 2015. **142**(5): p. 054704.

21.   Shapovalov, V. and T.N. Truong, *Ab initio study of water adsorption on α-Al$_2$O$_3$(0001) crystal surface.* The Journal of Physical Chemistry B, 2000. **104**(42): p. 9859-9863.

22.   Thissen, P., et al., *Water adsorption on the α-Al2O3(0001) surface.* Physical Review B, 2009. **80**(24): p. 245403.

Chapter 5 Surface phonon of α-Al2O3 (11-20) surface in both UHV and ambient conditions

Alumina (α-Al_2O_3) is one of the most commonly applied technological materials in industry where it plays an important role as a substrate for semiconductor thin film growth and as a catalyst support in heterogeneous catalysis[1-4]. Over the last several decades a number of workers have studied the performance of α-Al_2O_3 within these applications and found that its structure and termination strongly effect the growth of thin films or nano-materials [5] and the activity of the supported catalyst[6-11] in both experiment and theory.

For example, Naoki Ishigami et al. found that aligned carbon nano-tubes could be grown on both the A and R planes while growth on the C plane resulted in only random orientation. Based on SEM and Raman results they attributed this phenomenon to the surface atomic arrangements[5]. As one model catalyst for CO oxidation, Rh was deposited with similar particle size and density on α-Al_2O_3 (0001), (1-102) and (11-20) surfaces to evaluate the substrate effects on catalyst activity by Nehasil et al.[6]. The CO TDS results suggested the activation energy of adsorption obviously depended on the crystallographic orientation of the support but *how* the surface structure affected the interaction between CO and Rh was not clear. In principle one might imagine that the surface structure of α-Al_2O_3 could influence the interaction between catalyst and reactant, either unfavorably or favorably, or react with the catalyst leading to deactivation. One example of such a loss of activity is the Ni/α-Al_2O_3 system (Ni is a common catalyst for methane-steam reforming). In this case NiO was found to react with the substrate forming the relatively inactive $NiAl_2O_4$[7, 8]. Bolt et al.[9] investigated the mechanism of activity decrease by comparing the reactivity of NiO with polycrystalline α-Al_2O_3 and α-Al_2O_3 (11-20) single crystals into $NiAl_2O_4$ by XRD and Rutherford Backscattering Spectrometry and found the reaction rate was much higher on α-Al_2O_3 (11-20) than on polycrystalline alumina due to the higher grain boundary density of the NiO on the smooth single crystal support.

All the above discussion indicate that the surface structure and termination of substrate can affect the catalyst reactivity. To further understand this effect, Gutekunst et al.[11] characterized the atomic structure of Nb epitaxial films on sapphire substrates by high resolution transmission electron microscopy(HRTEM). These studies revealed a unique building principle for the atomic structure of the interfaces. Nb atoms or ions occupied Al lattice sites at the surface (the Al atom sites as the bulk lattice extended) to form the first layer while the Nb atoms of the second layer adjacent to the interface were positioned as close as possible to the Al lattice sites of a continued Al lattice of the sapphire. Some others found that artificially addition of aluminum on the substrate surface (before growing the thin film) would

affect rotational domain alignment of CdTe thin film on α-Al$_2$O$_3$ (0001) in theory[10]. These results indicate that the change of termination would dramatically change the growing of thin films at the interface which will finally cause change in its reactivity (as catalyst). Therefore to obtain the knowledge of surface structure and termination on atomic level is a pre-requisite to understand the different behaviors and to control and improve the related process and reactions.

As we already know, the termination of α-Al$_2$O$_3$ surfaces varies with the environment including the temperature and oxygen pressure which have been well studied by Kurita[12] and Yang Liu[13] with DFT first principle calculations. Because water is ubiquitous in environmental and most technological applications it seems reasonable to ask how it's adsorption affects the termination, and structure, of α-Al$_2$O$_3$ surfaces[14-16]. In this chapter I address these questions for the α-Al$_2$O$_3$ (11-20) surface and water pressures ranging from UHV to ambient atmosphere. This surface is one of the three most stable surfaces of alumina but both less studied, and more reactive towards water, than the (0001) and (1-102).

But it is challenging. Electron probes like low energy electron diffraction (LEED) and X-ray photoelectron spectroscopy (XPS) are restricted to UHV conditions and can also cause de-protonation on the surface[17]. X-ray scattering is capable to explore the surface termination information but not sensitive with the light H atoms[18, 19]. A surface specific technique that is applicable to both UHV and ambient conditions and sensitive to H atoms is required. The all-photon technique Sum-Frequency Generation (SFG) spectroscopy has become increasingly popular because it is both surface specific for materials with bulk inversion symmetry (like α-Al$_2$O$_3$) and is sensitive to de/protonated species vibrations [20]. There has been some work done with SFG spectra on the interaction of α-Al$_2$O$_3$ (11-20) with bulk water [21-23]. Sung[21] proposed a structure model for the protonated α-Al$_2$O$_3$ (11-20) surface prepared in ambient where the surface is terminated by Al$_3$O, Al$_2$OH and AlOH$_2$ with a ratio of 1:1:1 while the protonation state of each kind of oxygen was determined with the bonding satisfaction of the oxygens which is 2. Based on the bonding theory, AlOH$_2$ could only be formed given both of the two hydrogen formed hydrogen bond with the nearby oxygen but this is conflicted with what they interpreted of their SFG spectra of this surface: one peak around 3670 cm^{-1} appeared in the spectra which they argued should be assigned to the dangling OH stretching vibration from both Al$_2$OH and AlOH$_2$ (only one H formed H-bond and with the nearby singly coordinated O). Boulesbaa[22] et al. reported that the OH stretching mode at this region (3700 cm^{-1}) was contributed both by free OH of interfacial water and one type of aluminum hydroxyl group based on their free induction decay sum frequency generation measurement at pH 13. This conclusion conflicts with Sung's work where they argued that at high pH (>12) the surface should be negatively charged so that interfacial water would easily form H-bond thus no free OH at the interface. Tuladhar[23] studied also this interface with liquid water under different pH with SFG (which behaves similar as other's that a broad strong peak at ~3200 cm^{-1} while a weak and narrow centered ~3700 cm^{-1}) and focused his discussion on the interfacial water side which he thought

was strongly hydrogen bonded to alumina but with little discussion on the termination of alumina side. Until now, almost all the works that investigate the water/α-Al$_2$O$_3$ (11-20) interface with SFG spectroscopy are probing the OH stretching vibrations region. This makes understanding of the termination of alumina difficult: to do the assignment of OH vibrations is challenging since its vibration could be influenced significantly by the water side at the interface especially with liquid water (it is difficult to distinguish aluminum hydroxyl from that of water) and hydrogen bond could be formed between them which makes the OH stretching spectra broad and overlapped.

To get insight into the termination of α-Al$_2$O$_3$ (11-20) in equilibrium with water, it is helpful to directly probe the substrate involved vibrations—surface phonons. Therefore in this chapter, we probe SFG response in the region of Al-O or Al-OH vibrations under both UHV and ambient conditions: clean (11-20) surface under UHV (measured also in UHV), dissociative water adsorbed (11-20) surface (measured in UHV), and fully protonated (11-20) surfaces in ambient (measured in ambient, one sample is cleaned in UHV and another cleaned by following Sung's work[21]). DFT calculations are also done for better interpreting SFG results. By doing so, we hope to be able to learn the termination change from clean to fully protonated cases.

To better understand the following results and discussion, it is necessary to briefly introduce the sample preparation first.

5.1 Sample preparation

All the α-Al$_2$O$_3$(11-20) samples used in this work were round single crystals with a diameter of 15 mm, one side polished to a roughness <0.5 nm, the other unpolished, and were purchased from MaTeck. GmbH. To understand the surface reconstruction induced by water adsorption, it is a prerequisite to obtain the SFG response of the (11-20) surface in the absence of water. This has previously been suggested to be the O-I termination (as previously introduced in Figure 1.2 chapter 1) both by theory[12] and experiment[16] under UHV conditions. To obtain the O-I terminated clean α-Al$_2$O$_3$(11-20) surface [12], the crystal was treated in the same way as described in our previously published recipe [16, 24]: the as-received sample was sonicated in ethanol and in Milli-Q water, each for 15 min. After drying in N$_2$, it was mounted in our sample stage and then transferred into a UHV chamber where the sample surface was sputtered with argon at 1000 eV for 36 min at multiple points, followed by annealing first to 1200 K under UHV conditions, and then annealing in oxygen at 1200, 1100, and 950 K each for 10 min. After such a routine, the sample was confirmed to be carbon-free in Auger spectroscopy and to have a well-defined 1x1 lattice pattern in low energy electron diffraction.

To prepare a sample with sub-monolayer water adsorbed, H$_2$O is dosed onto the surface through molecular beam source in UHV chamber to form ice on top and then flashed to higher temperatures to

reduce the coverage to sub-monolayer as described in detail in chapter 4. The coverage is defined based on the TPD measurement as introduced in chapter 4, and we label the experimentally defined monolayer as eML, to be different from that as defined in theory calculations which we label as tML. SFG measurement was carried out when it was cooled down to 125 K (with Liquid N_2).

For the sample that reacted with water in ambient, we prepared two samples in different way: sample 1 is cleaned in the UHV chamber as introduced above and move it to ambient for SFG measurement; sample 2 is cleaned following the procedure applied in Sung's work and others[21, 25, 26]: the purchased crystal is cleaned in ultrasonically with acetone, methanol and Milli-Q water (18.3 MΩ cm) for 10, 10 and 45 min, respectively, and then being etched in 15 mM HNO_3 solution for 30 min, rinsed thoroughly with deionized water and blow-dried by nitrogen gas. SFG measurement is carried out on this two samples in ambient at room temperature.

5.2 SFG measurement geometry

To compare the surface phonon response of clean and water adsorbed α-Al_2O_3(11-20), SFG is carried out to samples that prepared differently: the O-I terminated clean (11-20) surface under UHV (measured also in UHV), dissociative water adsorbed (11-20) surface (~0.14 ML, measured in UHV), exposed to air (measured in ambient) and fully protonated (11-20) surfaces after air drying (measured in ambient). Figure 5. 1 is the sketch of the measurement geometry where x, y, z are the lab axes and a, b, c the crystallographic. Here azimuthal angle ϕ is defined as the angle between x axis and (0001) crystal direction(c axis). The surface normal, i.e. the (11-20) direction, is parallel to the z axis.

As shown in Figure 5. 1, the IR pulse and the 800 nm pulse propagated in the x-z plane and the incident angles are 62°± 0.5° and 45 °± 0.5°, respectively, for the ambient SFG measurement and 54°± 0.5° and 61 °± 0.5° for the measurement in UHV. The measurement in ambient is taken at room temperature while under UHV conditions, data are collected at 125 K (the sample is cooled with liquid nitrogen). SFG spectra are collected under both the ppp (SFG/Vis/IR, where p indicates parallel to the x-z plane) and ssp (SFG/Vis/IR, where s indicates perpendicular to the x-z plane) polarization combinations in this work.

In the beginning of this work, a CaF_2 window was mounted on the UHV chamber and both Vis and IR beam were propagated through this material and then focused on the sample. But this window generated a lot of problems due to its absorption of IR beam at long wavelength which will cause the chirping of the pulse thus affect the generated SFG signal. We tried to compensate for this chirp in the data analysis using the phase retrieval algorithm[27-29] which seemed to be able to solve this problem. However, we finally failed to get the data normalized by the non-resonance signal and the reason will be discussed in detail later. Therefore, to avoid this problem, KBr window was used to replace the CaF2 window, which

has little absorption of IR pulse. The normalization problem was solved in the end. So in the following, SFG results with CaF_2 window will be introduced first and then comes SFG results with KBr window.
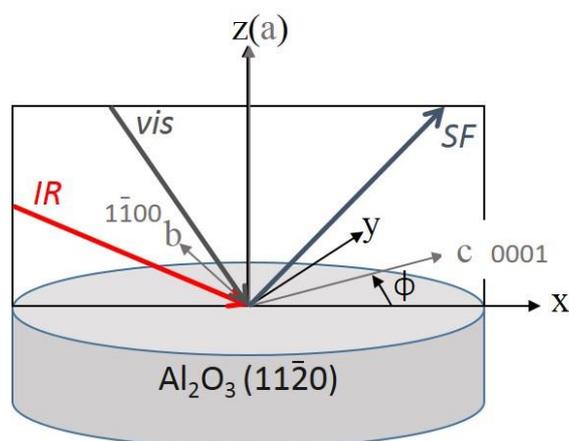

Figure 5. 1 Sketch of laboratory geometry for SFG measurement. Both incident and generated beams (reflected direction) are in x-z plane. Azimuthal angle (φ) is defined as the angle between c axis (0001) and the x axis.

5.3 SFG Al-O response with CaF_2 window under UHV conditions

5.3.1 IR pulse chirping

SFG measurement was carried out firstly in UHV chamber of α-Al_2O_3(11-20). With CaF_2 window, it was found the generated signal was chirped seriously. Figure 5. 3 is a two dimensional plot of SFG spectra that collected at different delay timing from -1000 to 1500 fs (y axis), in the frequency range 0-1500 cm^{-1} (x axis). It clearly shows within such a long delay timing scale, SFG signal did not disappear as it should be: SFG could be only generated when IR and Vis pulse overlapped with each both in space and time, when the timing delay between the two input is far away from time 0, the signal would vanish; in this work, the duration of the input pulses are in the scale of ~ 300 fs which is much shorter than what was observed in Figure 5. 3). The shape of this 2D plot is quite distorted that at different delay time the spectra response with different shape. Since CaF_2 window has good transmission for IR at shorter wavelength but obviously absorbs IR at longer wavelength above 10 μm which was the wavelength that applied in this work. The absorption of IR by the window causes two problems: the energy of IR beam decreased due to the absorption in fact it had been already as low as 10 μJ at this long wavelength in air and due to the scattering along the beam path and absorption by this window less than 3 μJ (only 30% transmission at 10 μm for one 5 mm thickness CaF2 window as shown in Figure 5. 2) could reach the sample; the absorption of IR will induce the chirping of the pulse which means different frequencies of the pulse travels through the window at different speed[30, 31]. To our measurement, the low energy of IR pulse was not a big problem (SFG is proportional to both intensities of IR and visible, the loss on IR could be compensated by increasing visible energy somehow) but the chirping of IR will be. To better

understand the problem that SFG generated with a chirped IR, the following simulates the process by comparing two cases one with un-chirped IR while the other with chirped IR.
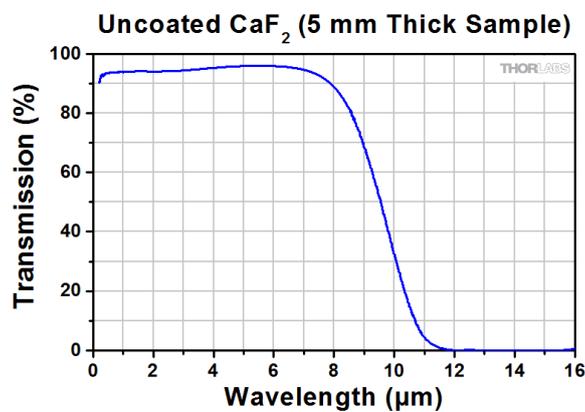

Figure 5. 2 Transmission curve of uncoated CaF2 window (5 mm thickness) from Thorlabs
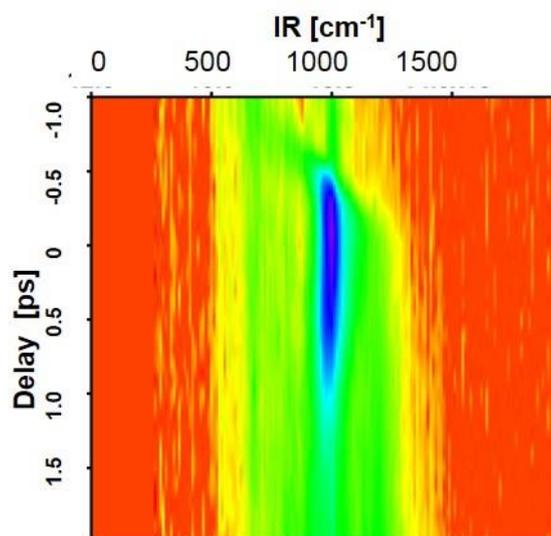

Figure 5. 3 Two dimensional plot of SFG signal of surface Al-O vibrations collected on α-Al$_2$O$_3$ (11-20) at different time delays between the Vis and IR pulses: the color from red to violet indicates the intensity increasing.
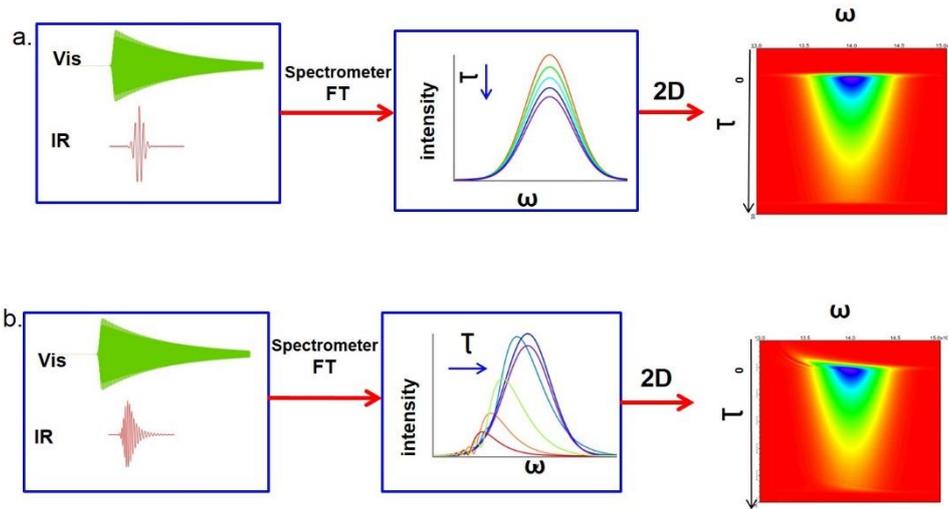
Figure 5. 4 Simulation of SFG generated by Visible and IR pulse with changing delay time: a) with un-chirped IR pulse; b) with chirped IR pulse through ZnSe window of thickness 4 mm.

In Figure 5. 4a, one visible beam and one un-chirped IR beam in time domain overlapped on the sample spatially, the generated SFG spectra was collected by a time domain spectrometer where the signal is Fourier transformed after data collection to produce a spectrum as a function of frequency. At time zero SFG spectra show the highest intensity while the intensity gradually decreased as the delay increased but all the spectra maintained the same shape with no shift of the center frequency. The 2D plot clearly shows the signal reach its intensity maximum at delay 0 and decreases gradually as the delay becomes larger and larger until the signal dies. However, the situation was different with a chirped IR pulse. As shown in Figure 5. 4b, SFG spectra collected at time zero still are the most intensive, but as delay time increases not only the intensity but the center frequency and shape of the spectra changedramatically and result in a distorted 2D plot.

5.3.2 Phase retrieval algorithm

In the case of this work, Figure 5. 3 shows that there is obvious spectral shape change at different delay time which is the feature of chirped situation of our IR pulse. How to obtain useful information from such kind of SFG spectra is the question one would like to address. Some groups [27-29] had worked with a mathematic approach-phase retrieval algorithm which seems to be able to solve our problems. Now I would like to briefly introduce the theory behind this algorithm. In principle, given an initial guess (the starting point) and two solutions satisfying constraints, one can gradually be closer and closer to the correct solution by computing as shown in the left panel of Figure 5. 5. Taking an example (the right panel of Figure 5. 5) to describe the process in details, given an initial guess of the input IR pulse (Visible can be known from experiment) in the form of electric field E(t), the generated signal electric field can be calculated as a function of time(t) and delay(τ) which is then Fourier transformed into

frequency domain as $E_{sig}(w, \tau)$. Here by applying the experimentally obtained SFG data, the amplitude could be corrected the first time where we get $E'_{sig}(w, \tau)$. With inverse Fourier transform, we get the time domain $E'_{sig}(t, \tau)$ where the SFG generation as described in Equation 5. 1 and Equation 5. 1 will be applied as the second constraint, we get a corrected E(t). Repeating this cycle many times, we are able to find the solution which is much closer to the 'real' value of E(t) finally.
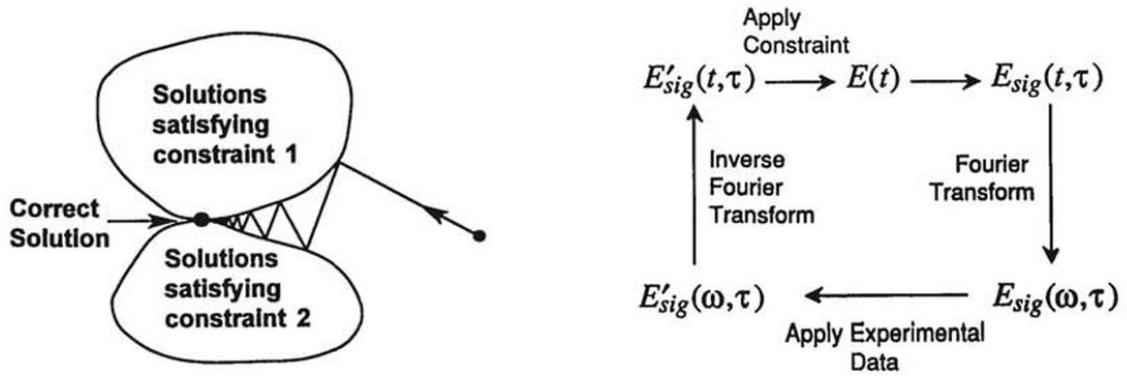
Figure 5. 5 Theory behind phase retrieval algorithm[27]

In the case of SFG spectra analysis with this phase retrieval algorithm, the signal electric field is proportional to the electric field of visible beam and the IR induced polarization P_{IR}, as shown in Equation 5. 1. Therefore, by applying this phase retrieval algorithm the solution of P_{IR} could be extracted. As a result, Figure 5. 6a displays the extracted P_{IR} of three samples that prepared in UHV chamber: the clean (11-20) surface, with small amount of dissociatively adsorbed water (0.14 eML, experimentally defined monolayer) and with higher water coverage (0.7 eML). All the three curves follow a similar shape where there seems to be one resonance centered around 1000 cm^{-1}, to know more detailed resonance information the data should be normalized by the non-resonance signal (generated on Au). However, we failed to normalize the data since during the measurement process the SFG signal was partially contributed by the window and this window generated SFG contributed differently on Au and sample (due to the different setup of data collection). One simple way to get rid of the unexpected contribution from either the non-resonance or noise from the window of the chamber is to look at the spectra difference, therefore we subtract the extracted P_{IR} of water adsorbed sample by that of the clean as displayed in Figure 5. 6b. Since the data below 800 cm^{-1} is noisy, we could only tell the resulted P_{IR} difference of two water adsorbed samples (with respect to clean sample) behaves similar with each other in the region 800-1200 cm^{-1}.

$$I_{SF} \propto \left| P_{IR}^{(2)} : E_{vis} \right|^2 \qquad\qquad 5.\ 1$$

$$P_{IR}^{(2)} = \chi^{(2)} : E_{IR} \qquad\qquad 5.\ 2$$
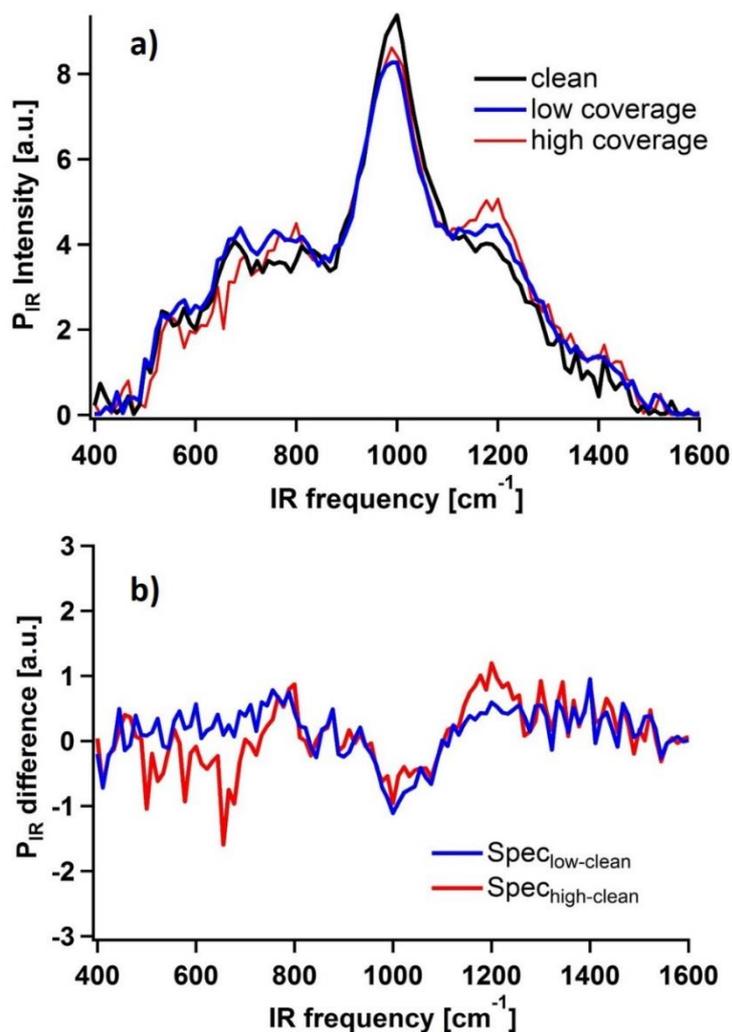
Figure 5. 6 Extracted IR induced polarization P_{IR} with phase retrieval algorithm

To obtain and compare resonance information of Al-O vibrations of water/α-Al$_2$O$_3$(11-20) interfaces in detail, it is necessary to replace the CaF$_2$ window with another material that has no SFG effect thus contributes nothing to the signal of the sample. KBr window that has as high transmission of IR as 90% in the wavelength above 10 μm will be applied with which we can get rid of the window SFG effect on one hand and remove the IR chirp problem on the other hand. And the SFG results with this window will be discussed in the following section.

5.4 SFG Al-O response with KBr window under UHV conditions

With KBr window, the signal decreased fast to zero within delay time 300 fs and no chirping happened to the IR pulse any more. By collecting SFG signal at different azimuthal angle, both the clean and with dissociative water adsorbed α-Al$_2$O$_3$(11-20) surfaces that prepared in UHV chamber present a 2-fold symmetry structure as shown in Figure 5. 7.
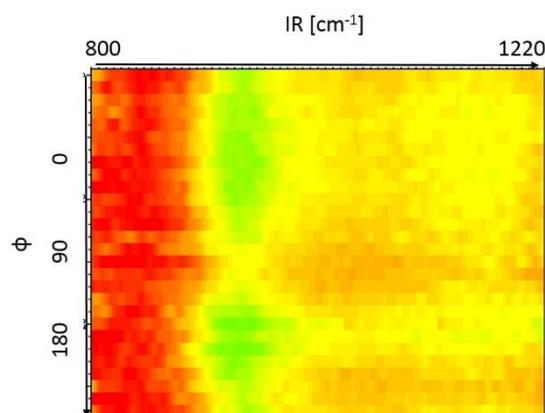
Figure 5. 7 2D plot of SFG collected at different azimuthal angle in UHV chamber with KBr window: $\phi = 0°$ when incident plane is parallel to (0001) direction of α-Al$_2$O$_3$; the color presents for the signal intensity increased from red to green.

Under UHV conditions, we prepared both the O-I terminated α-Al$_2$O$_3$(11-20) surface and water adsorbed surface with sub-monolayer 0.14 and 0.7 eML. The SFG measurement is carried out at 125 K (sample temperature) where the surface and the adsorbed water are stable for weeks. SFG spectra are collected at azimuthal angle $\phi=0°$ (the definition of azimuthal angle see the above) under different polarization combinations ppp and ssp for both the clean (Figure 5. 8a) and water adsorbed α-Al$_2$O$_3$(11-20) surfaces (Figure 5. 8b). In Figure 5. 8a for the O-I terminated clean surface, an apparent broad feature appears at around 980 cm^{-1} under ppp polarization combination while we see a different feature that shows up at 1040 cm^{-1} under ssp polarization combination. For the water adsorbed surface as shown in Figure 5. 8b, SFG spectra collected for the sample with 0.14 eML water almost overlap with spectra of 0.7 eML water adsorbed sample, the higher water coverage under UHV conditions does not cause obvious spectra change in the Al-O vibration region. In addition, the SFG spectra collected under ppp polarization for both the two samples behave quite similar to that of the clean surface while ssp spectra look significantly different, the feature shifts to lower frequency region (centered around 1000 cm^{-1}). It seems that SFG response under ppp polarization is not sensitive to water adsorption while that under ssp polarization is.
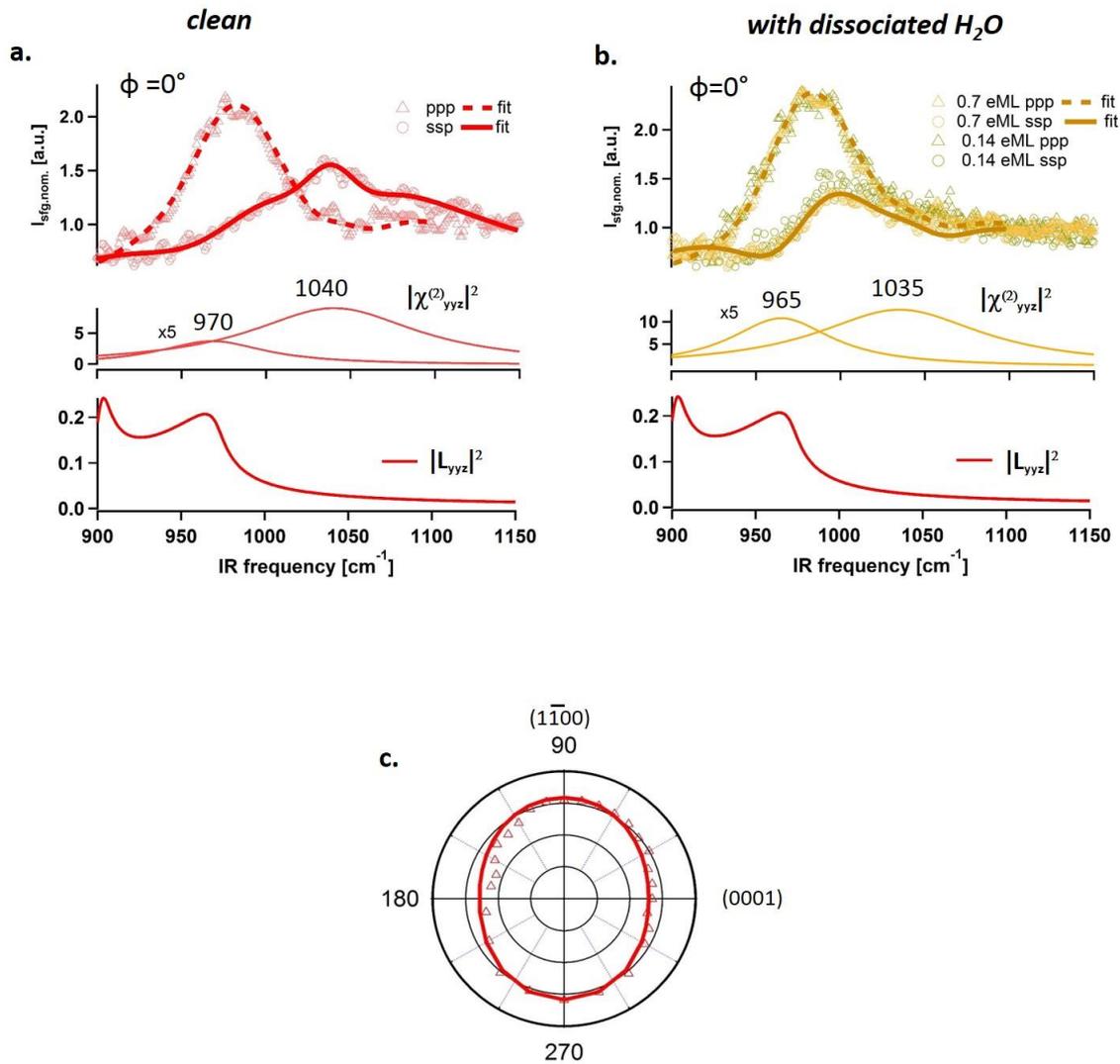
Figure 5. 8 Spectrascopy of phonon vibrations of α-Al$_2$O$_3$(11-20) under UHV conditions: a) O-I terminated clean surface; b)with sub-monolayer water adsoption (0.14 eML in green and 0.7 eML in brown); All the spectra are collected at azimuthal angle ϕ=0° at 125 K(thick solid line- ssp spectra, thick dashed line-ppp spectra). Bottom panel of both figures show the components of second order nonlinear susceptibility extracted from data fit and the Fresnel facor for data simulation; c) I$_{SF}$ vs. azimuthal angle (by integrating the ppp spectra in the range 1010~1090 cm^{-1}, more detail see below)

To find the origin of the spectra change especially under ssp polarization combination, we fit the data by applying the line shape model as discussed in detail in chapter 2 and plotted the obtained resonances of ssp spectra (with Equation 2.19) in Figure 5. 8a: two resonances contributed to the ssp spectra which are centered at 970 cm^{-1} and 1040 cm^{-1} for the clean surface, respectively, while after water adsorbed they slightly shifted to lower frequency centered at 965 cm^{-1} and 1035 cm^{-1}, respectively. The Fresnel

factor (L_{yyz} and L_{xxz} follow the same shape) displayed in the bottom part of Figure 5. 8a and Figure 5. 8b clearly shows a peak centered around 970 cm^{-1}, which indicates the significant feature of ppp spectra at around 970 cm^{-1} also is contributed by Fresnel factor which is the feature of the substrate itself. Since we want to know how the resonance part of SFG responses with azimuthal angle, thus we integrated the SFG intensity in the region 1010~1090 cm^{-1} in Figure 5. 8c which indicates the Al-O vibration modes in this region carry a weak 2-fold symmetry feature in SFG response. Besides, we mentioned earlier that ppp spectra seemed to be quite insensitive with water adsorption (not like that of ssp spectra which is sensitive), the possible reason could be the phase of the resonance at higher frequency (~1040 cm-1) was off the phase of the non-resonance which will be convinced by the data in ambient that is going to be discussed later. All the fitting parameters with the uncertainty is listed in Table 5. 1.

Table 5. 1 Fitting parameters of SFG spectra of samples prepared in UHV.

	χ_{yyz} clean	χ_{yyz} H$_2$O
A$_{nr}$	4.4 ±0.9	4.6±0.2
θ	0.15±0.02	0.35±0.05
A$_i$	33.5±107	54±10
ω$_i$	970±1.5	965±0.9
Γ$_i$	38.8±2.4	36.8±4.2
A$_{ii}$	181.7±110	213±19
ω$_{ii}$	1040.3±2.6	1035±2.6
Γ$_{ii}$	63.7±3.6	65.1±3.2

As already being discussed a lot, α-Al$_2$O$_3$ has inversion symmetry in bulk so that there is no bulk modes are both IR and Raman active[32, 33]. For the clean α-Al$_2$O$_3$(11-20), the surface is composed by Al$_2$O and Al$_3$O species with a ratio of 1:2 (as introduced in chapter 3, also see Figure 5. 11b). It is reasonable to say the two resonances observed under ssp polarization of the clean surface origins in Al$_2$O and Al$_3$O vibrations, respectively. Also there can be other possibilities like the two resonances in SFG are from different vibration modes of one group (Al$_2$O or Al$_3$O). The consistence between SFG experiment and theory in our previous study indicated that at low coverage range under UHV conditions water favorably dissociates on (11-20) surface via. structure inter-CUSa/Oμ2 where Al$_2$O sites rather than Al$_3$O sites will get protonated thus results in the formation of Al$_2$OH on α-Al$_2$O$_3$ (11-20) surface. Therefore after water adsorption the vibrational feature of surface phonon might be changed due to the formation of Al$_2$OH (also including that formed between two Al atoms) which supports the observed ssp spectra change from clean to water adsorbed surfaces in Figure 5. 11. When comparing the ssp spectra of samples with 0.14 and 0.7 eML water adsorption in Figure 5. 8b, it is found the spectra have no obvious change which suggests once the (11-20) surface is water adsorbed Al-O SFG response becomes insensitive with water coverage (at least in the range 0.14 to 0.7 eML). Further discussion on the

interpretation of SFG spectra will be given in section 5.6 by comparing with the theory results of the normal modes of the surface phonon vibrations.

To investigate the surface structure change of (11-20) with even higher water pressure, we prepared samples in ambient conditions where the surface was exposed to 10^{-2} bar water pressure, at least 8 orders higher that that prepared in UHV chamber (it is $\sim 10^{-10}$ bar during water dosing). SFG results in Al-O vibration region and its dependence on the azimuthal angle are discussed below.

5.5 SFG Al-O response of α-Al₂O₃ (11-20) in ambient

As discussed in the sample preparation in the beginning of this chapter, two samples were prepared and measured in ambient conditions: sample 1 is cleaned in UHV and taken out to ambient while sample 2 is cleaned by being etching in HNO_3 solution. We measured the SFG response in Al-O vibrational region of both the two samples to see whether they have the same termination when being placed in ambient. Figure 5. 9 displays both ppp and ssp spectra collected of sample 1(fit curve in solid blue line) and 2 (fit curve in solid green line) at azimuthal angle $\phi=0°$. ppp and ssp spectra are fitted with equation 2.18 and 2.17 (see below) as discussed in detail in chapter 2, respectively. For ppp spectra, both the two samples present a broad feature centered at ~ 970 cm^{-1} and the spectra almost overlap with each other (the blue and green); as for ssp spectra, both of the two samples again behave quite similar: two separated resonant features are observed at ~ 980 cm^{-1} and ~ 1050 cm^{-1}, respectively, only the intensity of the signal of sample 2 slightly decreased compared with that of sample 1. Since SFG signal is both dependent on the population squared and the functional group types, it is reasonable to argue the termination of the two samples both acted with water in ambient (via either reaction with humid lab air or in aqueous solution) are similar. Since we know for the sample 2 that cleaned by etching is hydrophilic and easily get fully wet[21], which means the clean O-I terminated surface once was exposed to ambient, will get fully protonated soon (we measured this sample around one hour after being exposed to ambient from UHV chamber).
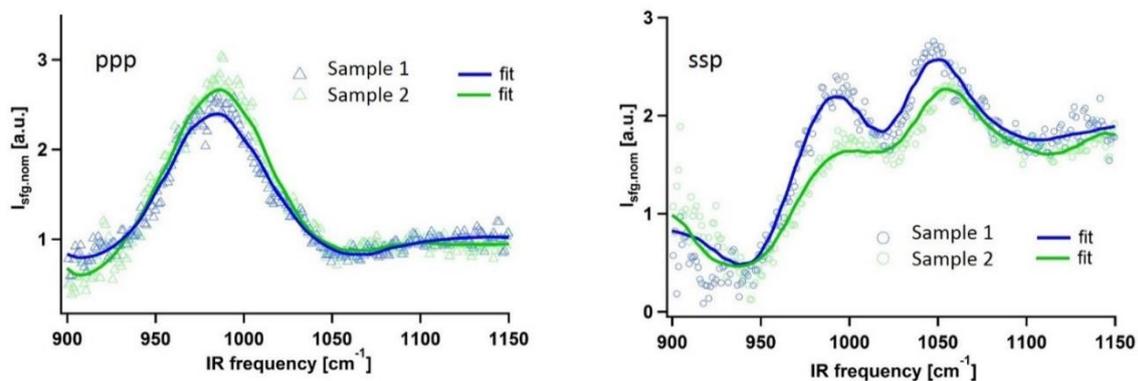
Figure 5. 9 SFG spectra of α-Al$_2$O$_3$(11-20) that acted directly with water in ambient (sample 1 cleaned in UHV shown in blue, while sample 2 cleaned with etching method is in green) under ppp (left panel) and ssp (right panel) polarization combinations: all collected at φ=0°.

Since the two samples behave quite similar (see *Figure 5. 9*) in the following part of this chapter we will discuss only the SFG results of the sample 1 which is cleaned in UHV before moved to ambient. Figure 5. 10 displays the spectral response at azimuthal angle (with respect to (0001) direction see Figure 5. 1) φ=0° and φ=90° of α-Al$_2$O$_3$(11-20) in ambient. For the ppp spectra at φ=0° (Figure 5. 10a), it looks similar to that observed from samples prepared under UHV conditions with a broad peak centered at 970 cm^{-1}. However, for the ssp spectra at φ=0°, it behaves absolute different with neither the clean surface nor water dissociatively adsorbed surface (see *Figure 5. 8*): two apparent features shows up that one is centered around 980 cm^{-1} while the other at 1050 cm^{-1}. In Figure 5. 10b when the crystal was rotated by 90°, it is found that the signal intensity becomes smaller for both ppp and ssp spectra but that the ssp spectra still shows two distinct peaks. The interesting thing is that if we compare the ssp and ppp spectra in Figure 5. 10b, we find in the region of the higher frequency peak of ssp from 1010 cm^{-1} to 1090 cm^{-1}, ssp signal intensity is above 1.0 (non-resonance position) while ppp signal is below 1.0 which indicates the ppp resonance at this region is out of the phase of non-resonance. This can be further convinced when we compare ppp spectra at φ=0° and φ=90°, the trough becomes deeper at φ =90° which means ppp resonance is stronger than that at φ=0° while ssp spectra is stronger at φ=0°. Since the calculated Fresnel factor of both ssp and ppp polarization also centered around 980 cm^{-1} which could also contribute to the signal so that the resonance at higher frequency 1050 cm^{-1} is of our interest regarding to dependence on azimuthal angle.
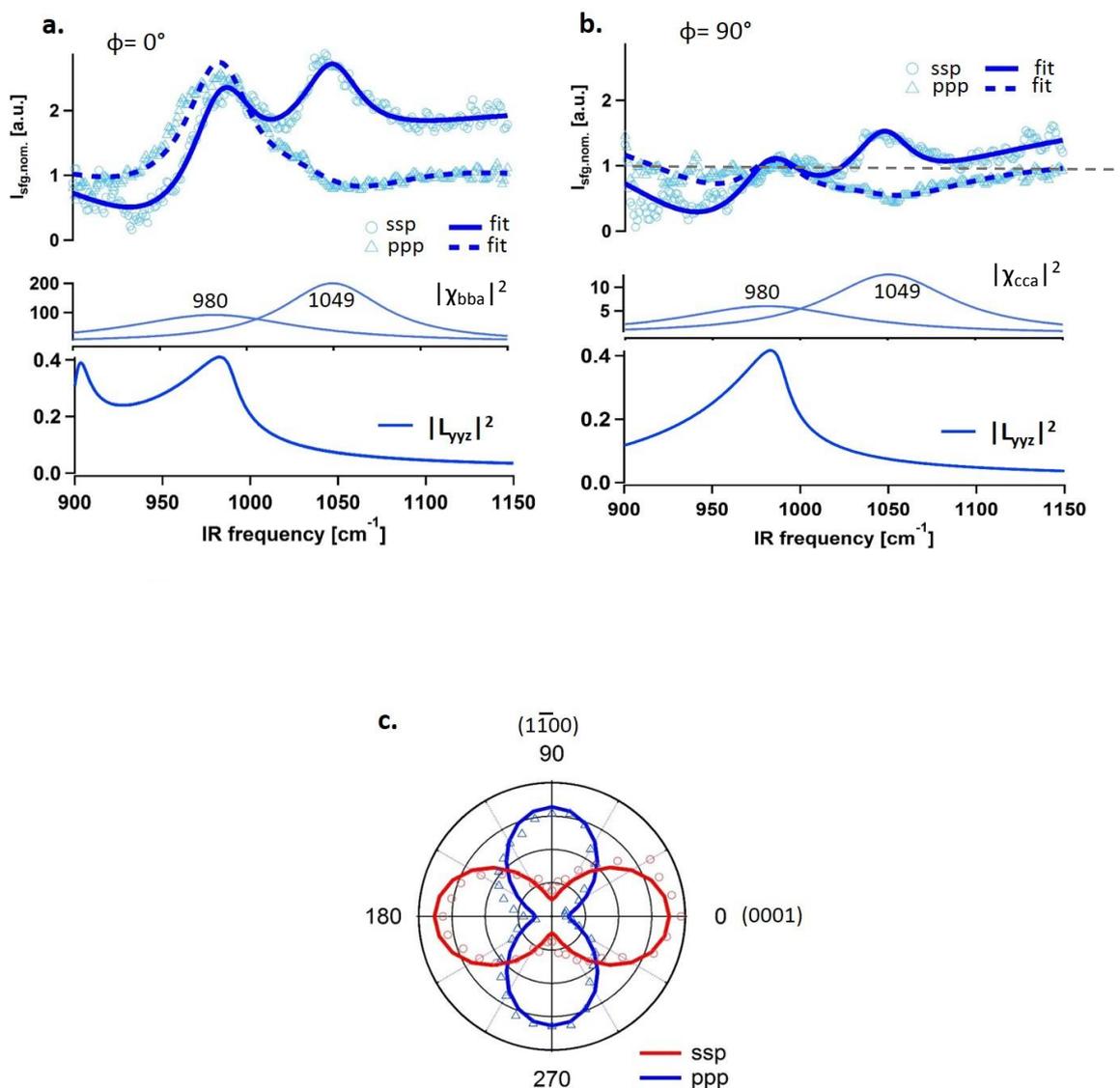
Figure 5. 10 SFG spectra of Al-O vibrations of α-Al$_2$O$_3$(11-20) in ambient of sample 1: a) both ppp and ssp spectra collected at azimuthal angle ϕ=0°; b) both ppp and ssp spectra collected at azimuthal angle ϕ=90°; c) integrated I$_{sfg}$ versus azimuthal orientation ϕ of the sample for the feature at higher frequency (region from 1010 cm^{-1} to 1090 cm^{-1}) in both ssp (red) and ppp (blue) spectra; All the spectra are collected at room temperature in ambient.

Therefore, we integrated the area between SFG spectra and the non-resonance line 1.0 for both ssp and ppp situations from 1010 cm^{-1} to 1090 cm^{-1} and plot them vs. ϕ. As presented in Figure 5. 10c, the SFG response of Al-O vibrations clearly has a 2-fold symmetry of α-Al$_2$O$_3$(11-20) prepared in ambient. Besides, ssp signal reaches the maximum at ϕ=0° ((0001) direction) and minimum at ϕ=90° ((1-100) direction) while ppp spectra behaves in contrast, this could be clearly understood when looking into Equation 2.17 and 2.10. Up until now, both the dramatic change in ssp spectra (two separated peak

features) and the Al-O vibrational symmetry (strong 2-fold rather than weak 2-fold) suggest, the interface structure of sample that acted with water in ambient is different from that prepared under UHV conditions.

To extract the information of resonance from the above SFG spectra (especially center frequency and amplitude), we employed the line shape model as introduced earlier in chapter 2 to fit the spectra in Figure 5. 10. Fitting ssp spectra with Equation 2.17 and 2.24 allows us to determine the second order nonlinear susceptibility component χ_{bba} at $\phi=0°$ while to extract another component χ_{cca} at $\phi=90°$. For the fitting of ppp spectra with Equation 2.18 it is much more complex since all the 13 non-vanishing components contribute:

$$\chi_{eff,ssp}^{(2)} = sin\beta_{ir}\, L_{yy}(\omega_{SF})L_{yy}(\omega_{vis})L_{zz}(\omega_{ir})\, (\chi_{bba}\cos^2\phi + \chi_{cca}\sin^2\phi\,)$$
$$-sin\beta_{ir}\, L_{yy}(\omega_{SF})L_{yy}(\omega_{vis})L_{zz}(\omega_{ir})(\chi_{cba}\cos\phi\sin\phi + \chi_{bca}\sin\phi\cos\phi\,)$$

<div align="right">2.17</div>

$$\chi_{eff,ppp}^{(2)}$$
$$= -cos\beta_{SF}cos\beta_{vis}sin\beta_{ir}\, L_{xx}(\omega_{SF})L_{xx}(\omega_{vis})L_{zz}(\omega_{ir})\, (\chi_{cca}\cos^2\phi$$
$$+ \chi_{bba}\sin^2\phi - \chi_{cba}\cos\phi\sin\phi - \chi_{bca}\sin\phi\cos\phi\,)$$
$$+ sin\beta_{SF}cos\beta_{vis}cos\beta_{ir}L_{zz}(\omega_{SF})L_{xx}(\omega_{vis})L_{xx}(\omega_{ir})(\chi_{acc}\cos^2\phi$$
$$+ \chi_{abb}\,\sin^2\phi - \chi_{acb}\cos\phi\sin\phi - \chi_{abc}\sin\phi\cos\phi)$$
$$- cos\beta_{SF}sin\beta_{vis}cos\beta_{ir}L_{xx}(\omega_{SF})L_{zz}(\omega_{vis})L_{xx}(\omega_{ir})(\chi_{cac}\cos^2\phi$$
$$+ \chi_{bab}\,\sin^2\phi - \chi_{cab}\cos\phi\sin\phi - \chi_{abc}\sin\phi\cos\phi)$$
$$+ sin\beta_{SF}sin\beta_{vis}sin\beta_{ir}L_{zz}(\omega_{SF})L_{zz}(\omega_{vis})L_{zz}(\omega_{ir})\chi_{aaa}$$

<div align="right">2.18</div>

With Fresnel factor corrected, we can model the experimental SFG data with susceptibility $\chi^{(2)}_{ijk}$, which can be described as a coherent superposition of a non-resonant background and Lorentzian resonance(s) as in equation 2.24:

$$\chi_{ijk}^{(2)} = \chi_{nr}^{(2)} + \chi_{r}^{(2)}$$

<div align="right">2. 24</div>

$$= |A_{nr}|e^{i\theta} + \sum_q \frac{|A_q|e^{i\theta_q}}{\omega_{IR} - \omega_q + i\Gamma}$$

with the non-resonant contribution being denoted by the amplitude $|A_{nr}|$ and phase**θ** , and the resonant contribution assumed to be capable of being approximated by discrete vibrational resonances with amplitude $|A_q|$ and phase θ_q, resonant frequencies ω_q and line width Γ. To simplify, we only focused on two ppp spectra that collected at $\phi=0°$ and $\phi=90°$. At $\phi=0°$, only 4 components of $\chi^{(2)}$ contribute: χ_{cca}, χ_{cac}, χ_{acc} and χ_{aaa}. Since χ_{cac} and χ_{acc} have similar strength but opposite sign, we fit ppp spectra with two components χ_{cca} and χ_{aaa} at $\phi=0°$ while it is χ_{bba} and χ_{aaa} dominating at $\phi=90°$. Therefore, a global fitting procedure is applied for ssp spectra at $\phi=0°$ (90°) and ppp spectra at $\phi=90°$ (0°) where they share the same parameters (non-resonance amplitude and phase, resonance amplitude, frequency, line width and

phase, the sign of each mode is embedded in phase while amplitude for all modes we assume is always positive) for χ_{bba} and χ_{cca} components (assuming rotating the sample changes only the azimuthal angle ϕ and not the resonant or nonresonant response, more details in appendix). With this method, both ppp and ssp spectra can be well fitted by two resonances centered at 980 cm^{-1} and 1049 cm^{-1} respectively, As plotted in the middle panel, it is the fitting results of ssp spectra and clearly it shows χ_{bba} (Figure 5. 10a) is much stronger than χ_{cca} (Figure 5. 10b) this is consistent with that ssp spectra is contributed by χ_{bba} while ppp spectra is dominated by χ_{cca} at $\phi=0°$ thus ssp spectra resonance is strongest while ppp is the weakest in the selected region (Figure 5. 10c). The fitting parameters with uncertainty are listed in Table 5. 2.

Table 5. 2 Fitting parameters of SFG spectra of α-Al$_2$O$_3$(11-20) prepared in ambient.

	χ_{bba}	χ_{cca}	χ_{aaa}
A_{nr}	3.57±0.3	2.69±0.2	2.75±0.5
θ	-0.25±0.02	0.46±0.05	-2.1±0.15
A_i	577±107	147±10	322.7±17
ω_i	980.7±0.9	980.7±0.9	980.7±0.9
Γ_i	60	60	60
A_{ii}	498±110	156.3±19	329.17±42
ω_{ii}	1050.6±2.6	1050.6±2.6	1050.6±2.6
Γ_{ii}	35±3.6	43.8±3.2	43.8±2.6

Note: we employ the Levenberg-Marquart algorithm, as implemented in the data analysis program Igor Pro (Wavemetrics) to actually fit the data. For the analysis of the low frequency Al-O (H) response of one sample in this work, we have assumed that the center frequency and line width of one resonance are the same for all the components of $\chi^{(2)}$ because all components of the $\chi^{(2)}$ sample the same underlying resonance.

5.6 Comparison with calculated normal modes
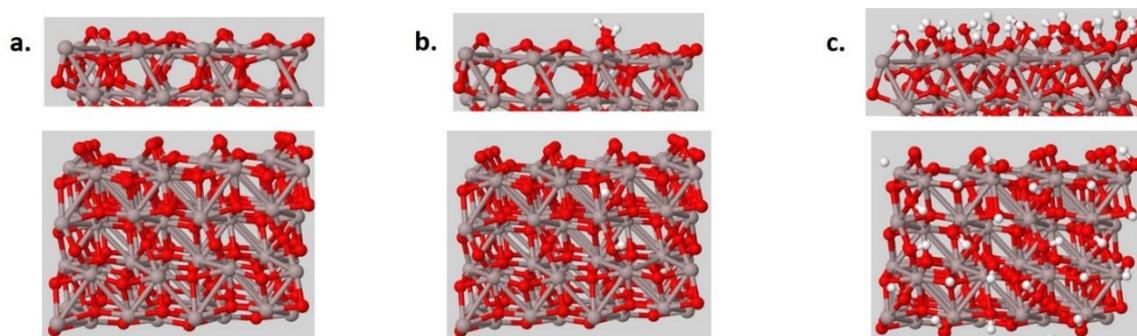
Figure 5. 11 (a) Model used to calculate O-terminated α-Al$_2$O$_3$(11-20) clean surface; (b) Slab used to calculate UHV-prepared dissociative water adsorbed α-Al$_2$O$_3$(11-20) surface properties(one water dissociated on 2x2 supercell); (c) Slabs used to calculate fully protonated α-Al$_2$O$_3$(11-20) surface properties; top panel the side-view of the 2x2 supercell and bottom panel the top-view of it; O atom in red, Al atom in grey and H atom in white.

From UHV conditions to ambient environment, the SFG response especially with ssp polarization combination in the surface phonon region of α-Al$_2$O$_3$(11-20) changed significantly. To do assignment of SFG resonances to the related surface Al-O vibrations is urgently required when we want to understand how the surface termination changes from UHV to ambient conditions. For this purpose, our coorperator Dr. Sophia Heiden from University of Potsdam calculated the surface normal modes of three cases with first principle DFT and the results are briefly introduced in the following part.

For the UHV prepared clean surface, it is indicated to be O-I termination (terminated by Al$_2$O and Al$_3$O in 1:2), both by the theoretical work of Kurita et al.[12] and of Becker [34], and also in our SFG experiment study on water dissociative adsorption on (11-20) in chapter 3. Figure 5. 11 shows the side (top panel) and top views (bottom) of the 25 atom layers thick and 2x2 super cell structures of this clean (Figure 5. 11a), with one water dissociated (Figure 5. 11b, 0.08 tML as 12 H$_2$O on 2x2 is defined as 1 tML, monolayer defined in theory) and fully protonated (Figure 5. 11c) α-Al$_2$O$_3$(11-20) surfaces. The atomic layer sequence of 1x1 unit cell is OO2Al4O2O-R of the O-I terminated clean surface in UHV and the top outmost O layer is doubly coordinated with surface Al (Al$_2$O) which are most active sites for water dissociation as suggested by both theory and experiment in chapter 3 and work[16]; the second layer is triply coordinated O (Al$_3$O) which is not active to water dissociation at low coverage. In this work we take one water dissociated on this 2x2 super cell as the model to evaluate the phonon vibrations of samples prepared with low water coverage under UHV conditions. The structure with high water population adsorption in ambient is very complex, there are numerous possibilities for it. In this work, a fully protonated surface structure (Figure 5. 11c) which is one simplified case is applied in theory calculation to mimic the structure in ambient conditions, where all 12 water molecules are dissociatively adsorbed on this 2x2 super cell with no consideration of forming hydrogen bond. The resulted atomic sequence of this fully protonated model is O2OOO2Al4O2O-R, while the out most layer is singly coordinated O (AlO) followed by two layers of Al$_2$O and Al$_3$O the fourth layer. The top most two layers of oxygen, singly coordinated AlO and doubly coordinated Al$_2$O, are from water while the third and fourth oxygen layers, doubly coordinated Al$_2$O and triply coordinated Al$_3$O are from alumina substrate.

Based on this, we calculated the phonon normal modes with the dipole square intensity along z direction (surface normal) since we have P polarized IR pulse and SFG intensity is proportional to the square of the derivative of the transition dipole moment (of the vibrational ground state and a vibrational excited state). Vibrational modes are treated in harmonic approximation and the z component is expanded until the second order (dipole squared where the population of the modes also included, as comparable to the second order emission of SFG). The total dipole spectrum is then given as a sum of all individual intensities.
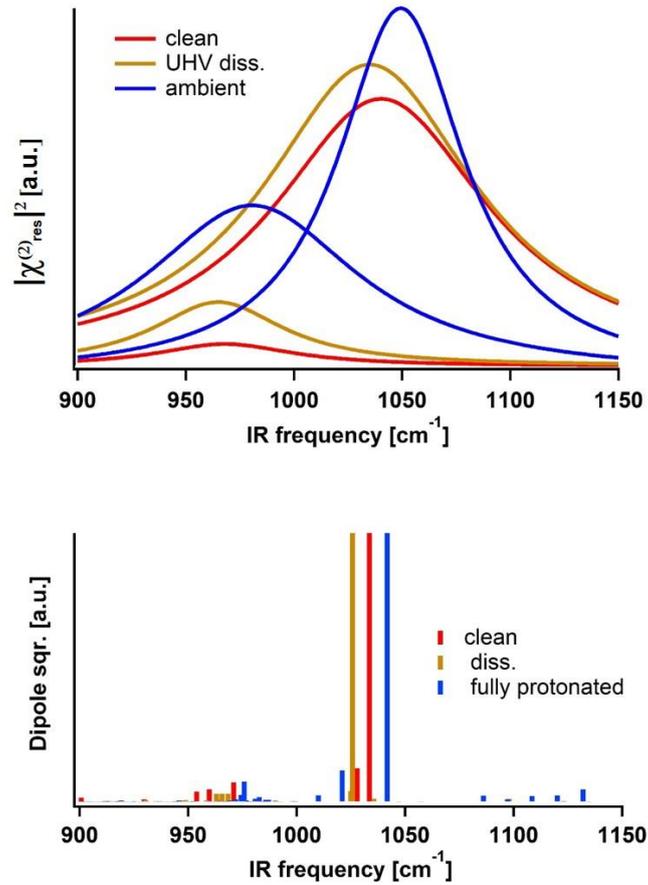
Figure 5. 12 Top panel, extracted resonances $|\chi_{res}^{(2)}|^2$ for the UHV prepared clean (red) , water dissociatively adsorbed(yellow) and fully protonated (blue) α-Al$_2$O$_3$(1120) surfaces, ssp polarization, ϕ=0°; bottom panel, the simulated dipole squared of the phonon normal modes for O-I terminated clean, one water dissociated (0.14 ML) and fully protonated α-Al$_2$O$_3$(1120) surfaces, respectively.

As introduced in Figure 5. 11c, we use a structure model where all the active sites for water adsorption on the surface are saturated to simulate the structure of α-Al$_2$O$_3$(11-20) in ambient: 12 water molecules are dissociatively adsorbed on 2x2 super cell and all the surface oxygen atoms (both Al$_2$O and Al$_3$O) are protonated with one hydrogen atom. Also, the idealized O-I terminated clean surface (Figure 5. 11a) and the surface with dissociative water adsorption (Figure 5. 11b) model are built for the phonon calculation. The calculated phonon normal mode frequencies and corresponding approximate intensities are presented in the bottom panel of Figure 5. 12. Calculated results of the fully protonated surface are shown in blue, that of water dissociatively adsorbed surface in yellow and the clean surface in red. On the clean surface this approach finds the highest frequency phonon mode located at 856 cm^{-1} and the next with a significant intensity at 837 cm^{-1}. However we observed the highest resonance of UHV prepared clean surface in experiment at ~1040 cm^{-1}. Thus the calculated phonon vibrations are multiplied by a factor 1.235, to account for model error like anharmonicity in vibration which is not considered in this calculation (the offset between theory and experiment has been discussed in detail previously [16]).

The scaled frequencies clearly suggest there are two vibrational regions that should display modes with significant intensity on all three surfaces: 950 cm^{-1} - 980 cm^{-1} and 1020 cm^{-1} - 1050 cm^{-1} with modes in the former generally weaker. To do the assignment of our observations in SFG response, the ssp resonances obtained with the line shape model in Equation 2.17 and 2.24 are shown in *Figure 5. 12* the top panel: clean surface and low water coverage under UHV conditions are in red and yellow while the resonances extracted from the SFG spectrum of fully protonated surface in ambient. If we look at the SFG results of all the three cases, it is not difficult to observe that there are two resonances contributed to the signal for all the three surfaces: one is centered at ~ 975 cm^{-1} with lower intensity and the other located at ~ 1050 cm^{-1}. In addition, both the two resonances shifts towards higher frequencies for the fully protonated sample compared with that of the clean surface. This observation in SFG experiment is well supported by the theory predictions as shown in the bottom panel of *Figure 5. 12*. As in theory, the dipole square of normal modes is calculated for the three surfaces. There are two vibrational regions for the normal modes that are of relatively high intensity: one in lower frequency ~950 cm^{-1} and the other in higher frequency ~1030 cm^{-1}. Given the vibrational modes in one region are pretty close to each other, dipole-dipole coupling may happen and also two neighboring normal modes (less than 10 cm^{-1}) beyond our SFG spectral resolution. So that one resonance as exacted from SFG should be possibly contributed by multiple modes. Therefore, the two resonances in SFG could be assigned to the two vibrational regions of normal modes.

Given our confidence that scaled normal mode frequencies reasonably reproduce the data (as shown in Figure 5. 12). We next use them to develop a microscopic view of surface structure. The assignment of the responsible modes is done in *Figure 5. 13* with a sketch of α-Al$_2$O$_3$(11-20) surface in three cases. For the O-I terminated clean surface, the experimentally observed resonance centered at ~1040 cm^{-1} is contributed by vibrations of the Al$_2$O group while vibration of Al$_3$O contribute to the lower frequency resonance centered at ~970 cm^{-1}. For the UHV prepared water adsorbed surface, the dissociated water fraction OH forms Al$_2$OH with two surface Al atoms (the most favorable adsorption structure inter CUSa/Oμ2) which is the origin of the resonance at ~1035 cm^{-1} in ssp spectra and the lower frequency resonance at ~965 cm^{-1} is due to the inactive Al$_3$O vibrations. For the fully protonated sample, there are two kinds of Al$_2$OH. One is the result of protonation of surface 2-fold O and the other bidentate adsorption of an OH fragment originating from dissociatively adsorbed water. Both structural features appear to contribute to the higher frequency resonance centered around 1050 cm^{-1} of α-Al$_2$O$_3$(11-20) in ambient while both protonated Al$_3$OH and other vibrational modes of Al$_2$OH contribute to the resonance observed at 980 cm^{-1}.
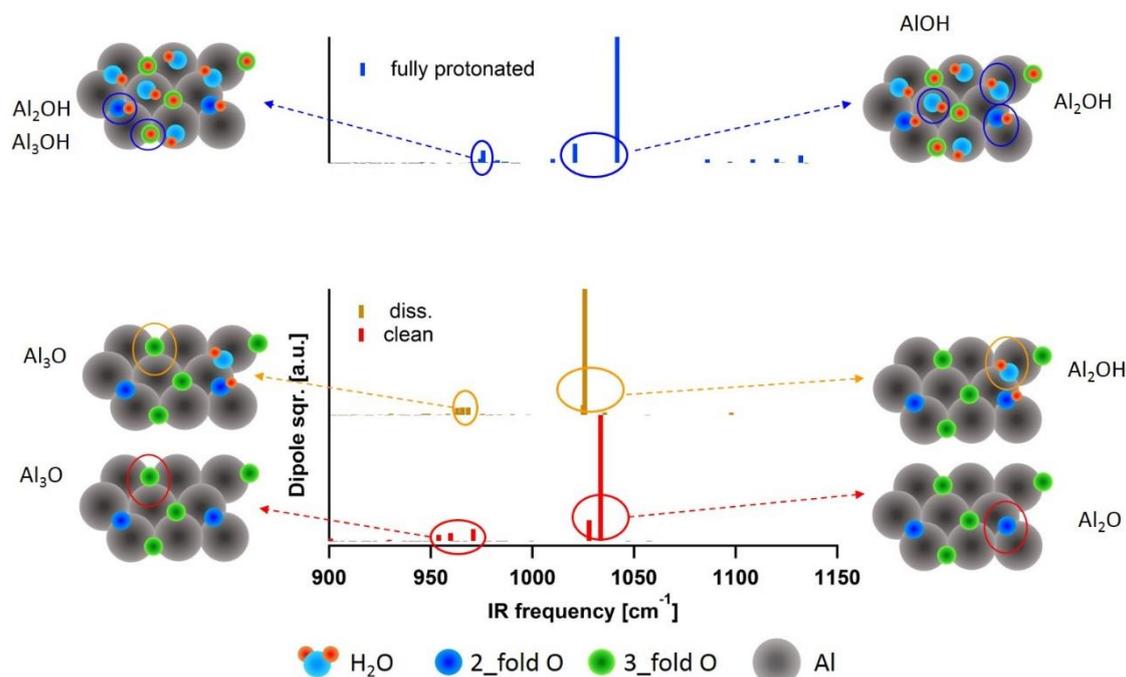
Figure 5. 13 The surface functional groups (top view) that are responsible for the normal modes as observed in SFG measurement of clean O-I termination (bottom), water dissocatively adsorbed (medium) and fully protonated α-Al$_2$O$_3$(11-20) surface structures (top); Al atom in large grey ball, 3-fold O in green, 2-fold O in blue, O from dissociated water in light blue and H in orange.

The above assignment based on the agreement between SFG and DFT calculations, permits us to look into the termination change of α-Al$_2$O$_3$(11-20) from UHV to ambient conditions: the clean surface in UHV chamber is O-I termination, which is composed of Al$_2$O and Al$_3$O functional groups in a ratio 1:2; for the fully protonated surface in ambient, it is composed of AlO, Al$_2$O and Al$_3$O in a ratio 1:1:1. To compare this fully protonated termination with previous study by Kurita[12], we try to plot this structure in the same way as he did, as shown in *Figure 5. 14*.

As being reported by Kurita[12], α-Al$_2$O$_3$(11-20) has five possible terminations in theory including 4 kinds of O-termination (O-I/II/III/IV) and one kind of Al-termination (Al-I) as shown in *Figure 5. 14*a. The O-I termination of the clean surface is labeled in color (Al$_3$O in green, and Al$_2$O in blue). As shown in *Figure 5. 14*b, it is the termination in the side view fo fully protonated (11-20) which is composed by three kinds of groups AlO, Al$_2$O and Al$_3$O with the ratio 1:1:1, and the atomic sequence is O2OOO2Al4O2O-R which is just the same as O-III termination as shown in *Figure 5. 14*a. Our conclusion is consistant with previous report by Catalano[35] that he studied the termination of the fully protonated α-Al$_2$O$_3$ (11-20) with X-ray reflectivity method.
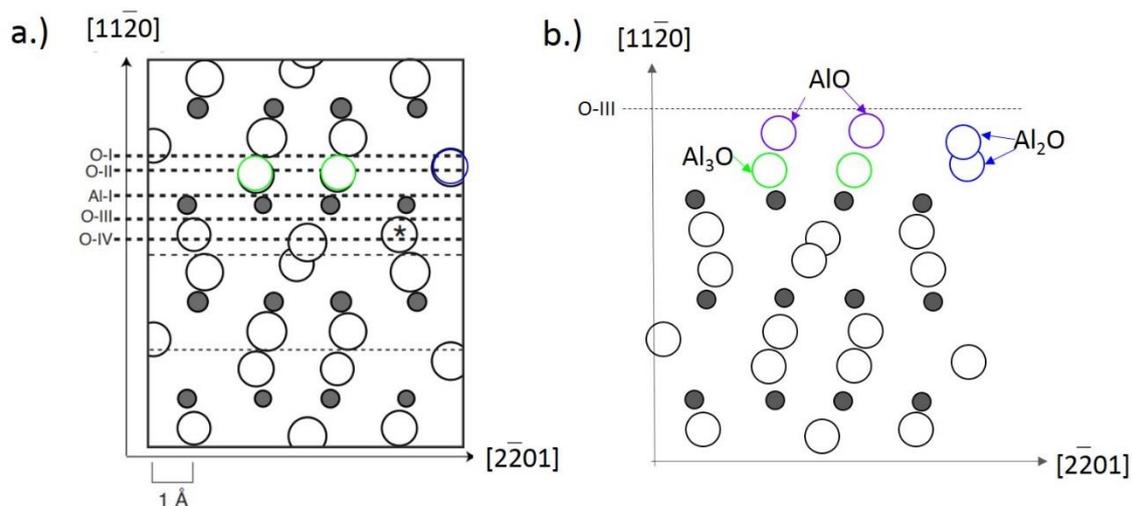
Figure 5. 14 Possible terminations of α-Al$_2$O$_3$(11-20) by Kurita[12] where O-I termination is the termination of UHV prepared clean surface in our study (a); termination of fully protonated α-Al$_2$O$_3$(11-20) in ambient (b).

To come to our conclusion with the above discussion, it is a O-I termination of clean (11-20) surface in UHV, and it changes to a O-III termination when the surface is exposed to ambient with high water pressure as 10^{-2} bar. One thing interesting is that surface prepared in UHV with water sub-monolayer (even 0.7 eML) does not present with O-III termination, the SFG spectra behaves different from that prepared in ambient. The background water pressure in UHV during dosing is around 10^{-10} bar, which is much lower than that in ambient. We consider the water adsorption on (11-20) surface is an equilibrium process between the surface and the gas phase, the resulted adsorption structure also the coverage in UHV chamber should be different from that prepared in ambient. Our work suggest that water adsorption will induce surface reconstruction of (11-20), and the transfer of O-I termination of (11-20) to O-III termination only happens at high water pressure like in ambient.

Another issue we are interested to discuss is the activity of surface oxygen towards protonation. In UHV chamber, for the O-I termination, our study with SFG-DFT combined approach both by probing hydroxyl stretching vibration in chapter 3 and surface Al-O vibration in this chapter suggest that only Al$_2$O is active with water dissociation at low coverage thus Al$_2$OH forms on the surface while Al3O stays without being protonated. This could be understood by noting the bigger negative charge and smaller basicity of O bound to two Al atoms, also the distance between 2-fold O and Al is smaller than that between 3-fold O and Al which also help the dissociation happen at Al$_2$O site and the neibouring Al. For the O-III terminated fully protonated α-Al$_2$O$_3$(11-20) in ambient, our study propose a possible situation that Al3O is protonated and the surface is composed by AlOH, Al$_2$OH and Al$_3$OH in 1:1:1. In Sung's work[21], they argued the Al$_3$O was difficult to get protonated except possibly under very acidic conditions while AlOH$_2$ existed given both the two H forming H-bond with the neighboring O which disagreed with what he interpreted about their SFG results.

5.7 Summary and conclusion

The surface structure and termination of α-Al$_2$O$_3$ plays a key role in its performance as substrate to grow other materials and catalyst support as discussed earlier. The termination could be affected by many environmental factors like O$_2$ pressure, temperature and so on. In this work, we are interested in how water adsorption will affect the termination of α-Al$_2$O$_3$(11-20) which is one of the three most thermodynamic stable cuttings but less studied.

With SFG technique, we successfully probed the spectra change in the Al-O vibrations at the range 900-1200 cm^{-1} of samples that prepared in UHV (clean and water dissociatively adsorbed) and in ambient. By probing the surface phonon vibration rather than OH stretching vibrations as most people did in previous work, the signal takes advantage of being not influenced by the interfacial water side which always makes the assignment SFG response of OH much difficult. We are able to obtain the vibrational information purely from the substrate involved side and learn the termination of alumina. By combining the SFG results (the resonance information extracted by global fitting) and theoretical calculations of normal modes of three surfaces, we are able to make such a conclusion as: it is O-I termination for UHV prepared clean α-Al$_2$O$_3$(11-20) where the surface is composed by Al$_2$O and Al$_3$O with ratio 1:2, while in ambient the fully protonated surface is O-III terminated which is composed of AlO, Al$_2$O and Al$_3$O with ratio 1:1:1. This dramatical change of surface termination happens fast when clean α-Al$_2$O$_3$(11-20) is transformed from UHV to ambient conditions which also suggests the O-I terminated (11-20) surface is very hydrophilic and active with water adsorption in ambient with water pressure 10^{-2} bar. Sample that acted with water in UHV chamber under pressure 10^{-10} bar won't result in O-III termination. Therefore, the reconstruction from O-I to O-III of (11-20) surface is water pressure dependent.

Before, people who investigated water/α-Al$_2$O$_3$(11-20) always focused on the already fully protonated surface (in ambient or with liquid water) and found that it was terminated by AlO, Al$_2$O and Al$_3$O. Our work study the termination of α-Al$_2$O$_3$(11-20) from UHV to ambient conditions, which allows an insight into how the O-I terminated clean surface gets reconstructed into O-III termination in ambient. Now we know that O-III termination is the product of reaction between O-I and water adsorption: the top most two O layers of O-III are from water.

The above findings of α-Al$_2$O$_3$(11-20) termination is of crucial importance when we want to discuss the surface macro-properties like charges which further affect the reactions with other species; what is more, the termination change from water free environment to ambient should be much considered especially when it is used as substrate to grow thin films or catalyst in inductry since this may change the growth of the first atomic layer of the film due to the lattice change.

In addition, the SFG approach as implemented in this work to probe the surface phonon vibrations can be extended to other surfaces of α-Al$_2$O$_3$ and other metal oxides/water interfaces to learn their termination change or reconstruction that induced by water adsorption.

5.8 References

1.   S.H. Behrens; Borkovec, M., *Electrostatic interaction of colloidal surfaces with variable charge.* The Journal of Physical Chemistry C, 1999. **103**: p. 2918-2928.

2.   Kosmulski, M., *pH-dependent surface charging and points of zero charge. III. Update.* J Colloid Interface Sci, 2006. **298**(2): p. 730-41.

3.   Finne, A.P., et al., *An intrinsic velocity-independent criterion for superfluid turbulence.* Nature, 2003. **424**(6952): p. 1022-5.

4.   Henrich, V.E.C., P. A. , *The surface science of metal oxides* 1996, england: Cambridge University Press.

5.   Ago, N.I.H., *Crystal plane dependent growth of aligned single-walled carbon nanotubes on sapphire.* Journal of the American Chemical Society, 2008. **130**(30): p. 9918-9924.

6.   Nehasil, V., et al., *The interaction of carbon monoxide with Rh/α-Al$_2$O$_3$ model catalysts: influence of the support structure.* Surface Science, 1999. **433-435**: p. 215-220.

7.   Bolt, P.H., et al., *The interaction of thin NiO layers with single crystalline α-Al$_2$O$_3$(11-20) substrates.* Surface Science, 1995. **329**(3): p. 227-240.

8.   Kotula, P.G., et al., *Kinetics of thin-film reactions of nickel oxide with alumina: I, (0001) and (11-20)reaction couples.* Journal of the American Ceramic Society, 1998. **81**(11): p. 2869-2876.

9.   Bolt, P.H., et al., *Interfacial reaction of NiO with Al$_2$O$_3$(11-20) and polycrystalline α-Al$_2$O$_3$.* Applied Surface Science, 1995. **89**(4): p. 339-349.

10. Meinander, K. and J.S. Preston, *A DFT study on the effect of surface termination in CdTe (111)/α-Al$_2$O$_3$(0001) heteroepitaxy.* Surface Science, 2015. **632**: p. 93-97.

11. Gutekunst, G., et al., *Atomic structure of epitaxial Nb-Al2O3 interfaces I. Coherent regions.* Philosophical Magazine A, 1997. **75**(5): p. 1329-1355.

12. Kurita, T., K. Uchida, and A. Oshiyama, *Atomic and electronic structures of α-Al$_2$O$_3$ surfaces.* Physical Review B, 2010. **82**(15).

13. Liu, Y., et al., *Termination, stability and electronic structures of α-Al$_2$O$_3$(0114) surface: An ab initio study.* Applied Surface Science, 2014. **303**: p. 210-216.

14. Wirth, J., et al., *Characterization of water dissociation on α-Al$_2$O$_3$((1-102): theory and experiment.* Physical Chemistry Chemical Physics, 2016. **18**(22): p. 14822-32.

15. Kirsch, H., et al., *Experimental characterization of unimolecular water dissociative adsorption on α-alumina.* The Journal of Physical Chemistry C, 2014. **118**(25): p. 13623-13630.

16. Heiden, S., et al., *Water dissociative adsorption on α-Al$_2$O$_3$(11-20) is controlled by surface site undercoordination, density, and topology.* The Journal of Physical Chemistry C, 2018. **122**(12): p. 6573-6584.

17. Li, F., et al., *X-ray radiation induces deprotonation of the bilin chromophore in crystalline d. radiodurans phytochrome.* Journal of the American Chemical Society, 2015. **137**(8): p. 2792-2795.

18. Trainor, T.P., et al., *Crystal truncation rod diffraction study of the α-Al$_2$O$_3$(1-102) surface.* Surface Science, 2002. **496**: p. 238-250.

19. Tanwar, K.S., et al., *Surface diffraction study of the hydrated hematite surface.* Surface Science, 2007. **601**(2): p. 460-474.

20. Shen, Y.R., *Surface properties probed by second-harmonic and sum-frequency generation* Nature, 1989. **337**: p. 519-525.

21. Sung, J., Y.R. Shen, and G.A. Waychunas, *The interfacial structure of water/protonated α-Al$_2$O$_3$(11-20) as a function of pH.* Journal of Physics: Condensed Matter, 2012. **24**(12): p. 124101.

22. Boulesbaa, A. and E. Borguet, *Vibrational dynamics of interfacial water by free induction decay sum frequency generation (FID-SFG) at the α-Al$_2$O$_3$(11-20)/H$_2$O Interface.* The Journal of Physical Chemistry Letters, 2014. **5**(3): p. 528-533.

23. Tuladhar, A., et al., *Spectroscopy and ultrafast vibrational dynamics of strongly hydrogen bonded OH species at the α-Al$_2$O$_3$(11-20)/H$_2$O interface.* The Journal of Physical Chemistry C, 2016. **120**(29): p. 16153-16161.

24. Kirsch, H., et al., *Experimental characterization of unimolecular ater dissociative Adsorption on α-alumina.* The Journal of Physical Chemistry C, 2014. **118**(25): p. 13623-13630.

25. Sung, J., et al., *Surface structure of protonated R-sapphire (1-102) studied by sum-frequency vibrational spectroscopy.* Journal of the American Chemical Society, 2011. **133**(11): p. 3846-53.

26. Tong, Y., et al., *Optically probing Al-O and O-H vibrations to characterize water adsorption and surface reconstruction on alpha-alumina: an experimental and theoretical study.* The Journal of Chemical Physics, 2015. **142**(5): p. 054704.

27. DeLong, K.W., et al., *Frequency-resolved optical gating with the use of second-harmonic generation.* Journal of the Optical Society of America B, 1994. **11**(11): p. 2206-2215.

28. Kane, D.J., *Real-time measurement of ultrashort laser pulses using principal component generalized projections.* IEEE Journal of Selected Topics in Quantum Electronics, 1998. **4**(2): p. 278-284.

29. Kane, D.J., et al., *Simultaneous measurement of two ultrashort laser pulses from a single spectrogram in a single shot.* Journal of the Optical Society of America B, 1997. **14**(4): p. 935-943.

30. Doll, A. and G. Jeschke, *Fourier-transform electron spin resonance with bandwidth-compensated chirp pulses.* Journal of Magnetic Resonance, 2014. **246**: p. 18-26.

31. Elu, U., et al., *High average power and single-cycle pulses from a mid-IR optical parametric chirped pulse amplifier.* Optica, 2017. **4**(9): p. 1024-1029.

32. Porto, S.P.S.K., R. S., *Raman effect of corundum.* The Journal of Chemical Physics, 1967. **47**(3): p. 1009-1012.

33. Hirose, C.E., Naotoshiakamatsu ; Kazunaridome, *Formulas for the analysis of the surface spectrum and transformation coefficients cartesian SFG tensor components* Applied Spectroscopy, 1992. **46**.

34. Becker, T., et al., *Microstructure of the α-Al$_2$O$_3$(11-20)surface.* Physical Review B, 2002. **65**(11).

35. Catalano, J.G., *Relaxations and interfacial water ordering at the corundum (110) surface.* The Journal of Physical Chemistry C, 2010. **114**: p. 6624–6630.

Chapter 6 Surface phonon of α-Al$_2$O$_3$(0001) surface in both UHV and ambient conditions

The properties of α-alumina's most stable surface, i.e. the (0001), have been extensively studied [1-6]. The reactivity of this surface toward water dissociative adsorption has been the subject of considerable debate. Many theoretical calculations[7-9] suggest that dissociative adsorption of water on (0001) is more favorable than molecular adsorption. However, our previous study showed that by storing the UHV prepared clean sample in ambient conditions it took ~ 1 month to see clear evidence for water dissociative adsorption [10]. The relative low reactivity we observed has been confirmed by Kimmel and co-workers[11] in UHV that even at low coverage they observed no dissociative water but molecular ones with IR spectra. Virtually all prior workers have concluded that for α-Al$_2$O$_3$ (0001) surfaces prepared in ambient and characterized in ambient or contact with liquid water, extensive hydroxylation takes place [12-16]. However, beyond this limited consensus extensive disagreement exists regarding surface properties such as the isoelectric point (IEP) [13, 17] and OH stretching spectral response of the water/α-Al$_2$O$_3$ (0001) interface[10, 12, 14, 15, 17, 18]. One possible explanation for these discrepancies is that the different preparation methods lead to different surface structures even for the surface in contact with liquid water. In this chapter, by comparing UHV and ambient prepared samples in a controlled manner, we hope to be able to get insight into the surface structures and water reactivity of each and help resolve these prior disagreements.

To characterize the reactivity of differently prepared surfaces in UHV and ambient, a tool that can measure the molecular level structure of the surface in both conditions and is sensitive to the chemical identities of the surface moieties is required. SFG is one of such tools. Based on 2nd order nonlinear optical process, SFG can provide structural and chemical properties of oxide surfaces both in UHV and at buried solid/liquid interface in ambient, and has been widely applied in surface science[10, 19-24]. SFG has already been employed to study the α-Al$_2$O$_3$ (0001) surface in ambient by different groups[10, 12, 14, 15, 17, 18]. In those work through probing the OH stretching vibration, relative populations of surface hydroxyl groups and the structure of water in contact with the surface were investigated. However, the spectral response for the seemingly the same terminated surfaces were found to be different. For instance, Florsheimer et al.[12], Shen et al.[15], and Tong et al.[10] observed a resonance associated with a weakly or non-hydrogen bonded OH group that centered around 3680 cm^{-1}; while Yeganeh et al.[17] and Tuladhar[18] et al., reported hardly any such feature. Braunschweig et al [14] found the presence of this free OH stretching mode depended on sample preparation (although they did not characterize the relationship between sample preparation and surface structure).

In addition to differences in sample preparation between these studies, contradictory conclusions may also be a consequence of the difficulty in interpreting the spectral response of interfacial OH. When alumina surface contacts with liquid water or solutions, OH stretch of adsorbed water molecules or that from solution side also contributes to the observed OH signals in SFG[25, 26]. Therefore, unambiguous assignment of OH stretch spectral features, and their correspondence to particular structural types of interfacial water or aluminols, is difficult. In our previous studies[10], it has been demonstrated that this challenge can be circumvented by probing Al-O(H) vibrations from the solid side, i.e. the surface phonon resonances of the oxide. Because surface phonons are spectrally well separated from bulk vibrations, the connection of spectral response and interfacial structure can in principle be more straightforwardly established.

In this work, we prepared and measured the Al-O SFG spectra of both clean surface and with sub-monolayer water adsorbed in UHV chamber, and of sample that prepared in ambient to understand how the surface structure change with different amount of water adsorption. To illustrate structural changes on exposure to ambient air we also characterize a partially hydroxylated sample in ambient. Additionally, by measuring the azimuthal dependence of the spectral response of all samples we characterize the symmetry of the surface Al-O vibrations we observe. To reduce uncertainties in line shape analysis all data analysis globally fits spectra collected as a function of azimuthal angle and under different polarization conditions.

Before proceeding to the results and data analysis, in the next section I briefly introduce the sample preparation.

6.1 Sample preparation and measurement geometry

I follow the same method as described in our previous work [10] to prepare α-Al$_2$O$_3$(0001) samples that are fully and partially hydroxylated under ambient conditions. In brief, to prepare the fully hydroxylated surface, the as-received crystal (purchased from Princeton Scientific) was cleaned in a sonication bath with acetone for 15, ethanol for 15, and Milli-Q water (18.3 MΩ cm) for 45 min. The sample was then mildly acid etched using a 15 mM solution of HNO$_3$ under sonication for 30 min and, after thorough rinsing with Milli-Q water, dried with blown nitrogen gas. The partially hydroxylated surface, based on our previous observations[10], could be obtained by baking the fully hydroxylated sample at 500 K for 30 min. SFG OH stretch spectra show that such treatment leads to a decreasing density of surface aluminols in air, that only recovers with weeks to months of exposure in ambient. While this treatment clearly results in a partially hydroxylated surface quantifying the extent of dihydroxylation is not possible without additional information. For our purposes here it is sufficient to compare the fully hydroxylated and partially hydroxylated responses.

In order to obtain a clean, water free α-Al$_2$O$_3$(0001) sample under UHV conditions, the as-received crystal was first washed in a sonication bath with acetone for 15, ethanol for 15 and then Milli-Q water for 45 min. After dying with nitrogen gas, it was installed in our UHV chamber, pumped down, sputtered with Argon plasma (1 KeV) at multiple points, annealed under UHV conditions at 950 K for 15 minutes twice, and in the end, annealed in oxygen at 1.0x10^{-6} mbar at 1000 K for 15 min to get rid of any oxygen vacancies induced the sputtering. After this procedure the surface is carbon-free, within the sensitivity of our Auger spectrometer, and has a well-defined 1x1 lattice pattern in low energy electron diffraction (see section 2.1.2 chapter 2). Given a clean, water-free surface, we prepared samples in UHV with dissociatively adsorbed H$_2$O through MBS with the same method as introduced in section 4. Samples are dosed until multilayers are generated, sub-monolayer coverages of water are creating by flash heating the multilayer sample to higher temperatures after deposition. In this work, we prepared samples in UHV that were flashed to 250 and 300 K after water dosing which yield a water adsorption of 0.5 eML and 0.26 eML which is experimentally defined coverage as discussed in chapter 4.
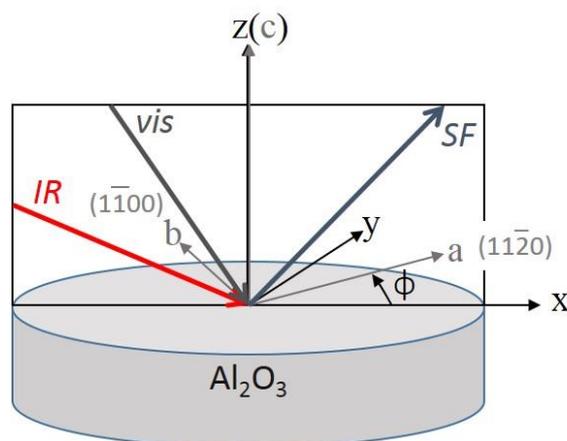
Figure 6. 1 Experimental geometry. All beams are in the x-z plane. The incident angles for IR/Vis are 60°/36° in ambient measurements and 54°/61° in the UHV chamber. SFG spectra were collected at different angles between the x-z plane and a-c plane of the α-alumina sample. This angle is defined as the azimuthal angle (ϕ, clockwise rotation is positive).

As shown in *Figure 6. 1*, the IR pulse and the 800 nm pulse propagated in the x-z plane and the incident angles are 60°± 0.5° and 36 °± 0.5°, respectively, for the ambient SFG measurement and 54°± 0.5° and 61 °± 0.5° for the measurement in UHV. The measurement in ambient is taken at room temperature while under UHV conditions, data are collected at 125 K (the sample is cooled with liquid nitrogen). SFG spectra are collected under both the ppp (SFG/Vis/IR, where p indicates parallel to the x-z plane) and ssp (SFG/Vis/IR, where s indicates perpendicular to the x-z plane) polarization combinations in this work.

6.2 Features of Fresnel factor

Since we are probing the surface phonon response of the birefringent crystal α-Al$_2$O$_3$, the effects of crystal anisotropy on the SFG response should be carefully considered especially we are going to measure the azimuthal angle dependence of the signal. As discussed in Chapter 2, the Fresnel factor relates the induced polarization to the emitted SFG electric field (accounting for the wave vector conservation requirement of the SFG process). The effects of crystal birefringence on the Fresnel factors for the α-Al$_2$O$_3$(0001) surface can be expressed in equation 2.22:

$$L_{xx} = \frac{2k_{2z,e}}{\epsilon_\perp \, k_{0z} + k_{2z,e}}$$

$$L_{yy} = \frac{2k_{0z}}{k_{0z} + k_{2z,o}} \qquad 2.22$$

$$L_{zz} = \frac{\epsilon_\perp}{\epsilon_\parallel} \frac{2k_{0z}}{\epsilon_\perp \, k_{0z} + k_{2z,e}}$$

While the wave vectors can be obtained with equation 2.23

$$k_{2z,o} = \frac{2\pi\omega}{c_0} \sqrt{\epsilon_\perp - \sin^2 \beta}$$

$$k_{2z,e} = \frac{2\pi\omega}{c_0} \sqrt{\epsilon_\perp - \frac{\epsilon_\perp}{\epsilon_\parallel} \sin^2 \beta} \qquad 2.23$$

Where β is the incident angle of one beam (refer to surface normal). The components of the Fresnel factor that contribute to the measured SFG signal are a function of surface symmetry and field polarization as shown in Equation 2.19-2.21 below (here we re-show these equations which are discussed more in details in chapter 2). If the surface is assumed to have C$_{\infty v}$ symmetry and is measured in the ppp polarization condition the relevant componets are L$_{xxz}$ and L$_{zzz}$ as shown in Equation 2.21. The expression of the nonlinear susceptibility under this condition is shown in Equation 2.21 and the dependence of the two Fresnel factor components on infrared photon energy (assuming incident angles of the UHV experiment) are plotted in Figure 6. 2(a). If, the surface has C$_{3v}$ symmetry the L$_{yyz}$ and L$_{yyx}$ Fresnel factor components contribute to spectra collected in the ssp polarization condition (see equation 2.19) while the L$_{xxz}$, L$_{zzz}$ and L$_{xxx}$ contribute to those collected under ppp (see equation 2.20). The dependence of all five Fresnel factor components, given the beam incident angles of the ambient experiment, on infrared photon energy are plotted in Figure 6. 2(b). As we will show below for the α-Al$_2$O$_3$(0001) surface in UHV and confirm (consistent with our prior study [10]) for the α-Al$_2$O$_3$(0001) surface in ambient, within our photon energy window the surface spectral response appears to have C$_{\infty v}$ symmetry for samples prepared and measured in UHV while it is C$_{3v}$ symmetry for samples measured in ambient.

$$\chi^{(2)}_{\text{eff,ssp}} = L_{yy}(\omega_{SF})L_{yy}(\omega_{vis})L_{zz}(\omega_{ir})\sin\beta_{ir}\chi^{(2)}_{yyz} + L_{yy}(\omega_{SF})L_{yy}(\omega_{vis})L_{xx}(\omega_{ir})\cos\beta_{ir}\chi^{(2)}_{yyx}$$

<div align="right">2.19</div>

$$= L_{yy}(\omega_{SF})L_{yy}(\omega_{vis})L_{zz}(\omega_{ir})\sin\beta_{ir}\chi^{(2)}_{aac} - L_{yy}(\omega_{SF})L_{yy}(\omega_{vis})L_{xx}(\omega_{ir})\cos\beta_{ir}\chi^{(2)}_{aaa}\cos3\phi$$

$$\chi^{(2)}_{\text{eff,ppp}} = -L_{xx}(\omega_{SF})L_{xx}(\omega_{vis})L_{zz}(\omega_{ir})\cos\beta_{SF}\cos\beta_{vis}\sin\beta_{ir}\chi^{(2)}_{xxz}$$

$$- L_{xx}(\omega_{SF})L_{xx}(\omega_{vis})L_{xx}(\omega_{ir})\cos\beta_{SF}\cos\beta_{vis}\cos\beta_{ir}\chi^{(2)}_{xxx}$$

$$- L_{xx}(\omega_{SF})L_{zz}(\omega_{vis})L_{xx}(\omega_{ir})\cos\beta_{SF}\sin\beta_{vis}\cos\beta_{ir}\chi^{(2)}_{xzx}$$

$$+ L_{zz}(\omega_{SF})L_{xx}(\omega_{vis})L_{xx}(\omega_{ir})\sin\beta_{SF}\cos\beta_{vis}\cos\beta_{ir}\chi^{(2)}_{zxx}$$

$$+ L_{zz}(\omega_{SF})L_{zz}(\omega_{vis})L_{zz}(\omega_{ir})\sin\beta_{SF}\sin\beta_{vis}\sin\beta_{ir}\chi^{(2)}_{zzz}$$

$$= -L_{xx}(\omega_{SF})L_{xx}(\omega_{vis})L_{zz}(\omega_{ir})\cos\beta_{SF}\cos\beta_{vis}\sin\beta_{ir}\chi^{(2)}_{aca}$$

$$- L_{xx}(\omega_{SF})L_{xx}(\omega_{vis})L_{xx}(\omega_{ir})\cos\beta_{SF}\cos\beta_{vis}\cos\beta_{ir}\chi^{(2)}_{aaa}\cos3\phi$$

$$- L_{xx}(\omega_{SF})L_{zz}(\omega_{vis})L_{xx}(\omega_{ir})\cos\beta_{SF}\sin\beta_{vis}\cos\beta_{ir}\chi^{(2)}_{aca}$$

<div align="right">2. 20</div>

$$+ L_{zz}(\omega_{SF})L_{xx}(\omega_{vis})L_{xx}(\omega_{ir})\sin\beta_{SF}\cos\beta_{vis}\cos\beta_{ir}\chi^{(2)}_{caa}$$

$$+ L_{zz}(\omega_{SF})L_{zz}(\omega_{vis})L_{zz}(\omega_{ir})\sin\beta_{SF}\sin\beta_{vis}\sin\beta_{ir}\chi^{(2)}_{ccc}$$

$$\approx -L_{xx}(\omega_{SF})L_{xx}(\omega_{vis})L_{zz}(\omega_{ir})\cos\beta_{SF}\cos\beta_{vis}\sin\beta_{ir}\chi^{(2)}_{aac}$$

$$- L_{xx}(\omega_{SF})L_{xx}(\omega_{vis})L_{xx}(\omega_{ir})\cos\beta_{SF}\cos\beta_{vis}\cos\beta_{ir}\chi^{(2)}_{aaa}\cos3\phi$$

$$+ L_{zz}(\omega_{SF})L_{zz}(\omega_{vis})L_{zz}(\omega_{ir})\sin\beta_{SF}\sin\beta_{vis}\sin\beta_{ir}\chi^{(2)}_{ccc}$$

$$\chi^{(2)}_{\text{eff,ppp}} = -L_{xx}(\omega_{SF})L_{xx}(\omega_{vis})L_{zz}(\omega_{ir})\cos\beta_{SF}\cos\beta_{vis}\sin\beta_{ir}\chi^{(2)}_{xxz}$$

$$- L_{xx}(\omega_{SF})L_{zz}(\omega_{vis})L_{xx}(\omega_{ir})\cos\beta_{SF}\sin\beta_{vis}\cos\beta_{ir}\chi^{(2)}_{xzx}$$

$$+ L_{zz}(\omega_{SF})L_{xx}(\omega_{vis})L_{xx}(\omega_{ir})\sin\beta_{SF}\cos\beta_{vis}\cos\beta_{ir}\chi^{(2)}_{zxx}$$

<div align="right">2.21</div>

$$+ L_{zz}(\omega_{SF})L_{zz}(\omega_{vis})L_{zz}(\omega_{ir})\sin\beta_{SF}\sin\beta_{vis}\sin\beta_{ir}\chi^{(2)}_{zzz}$$

$$\approx -L_{xx}(\omega_{SF})L_{xx}(\omega_{vis})L_{zz}(\omega_{ir})\cos\beta_{SF}\cos\beta_{vis}\sin\beta_{ir}\chi^{(2)}_{aac}$$

$$+ L_{zz}(\omega_{SF})L_{zz}(\omega_{vis})L_{zz}(\omega_{ir})\sin\beta_{SF}\sin\beta_{vis}\sin\beta_{ir}\chi^{(2)}_{ccc}$$

With Fresnel factor corrected, we can model the experimental SFG data with susceptibility $\chi^{(2)}_{ijk}$, which can be described as a coherent superposition of a non-resonant background and Lorentzian resonance(s) as in equation 2.24 as previously introduced in Chapter 2:

$$\chi^{(2)}_{ijk} = \chi^{(2)}_{nr} + \chi^{(2)}_{r}$$

$$= |A_{nr}|e^{i\theta} + \sum_q \frac{|A_q|e^{i\theta_q}}{\omega_{IR} - \omega_q + i\Gamma}$$

<div align="right">2.24</div>

<div align="center">117</div>

with the non-resonant contribution being denoted by the amplitude $|A_{nr}|$ and phase **θ**, and the resonant contribution assumed to be capable of being approximated by discrete vibrational resonances with amplitude A_q, resonant frequencies ω_q and line width Γ.
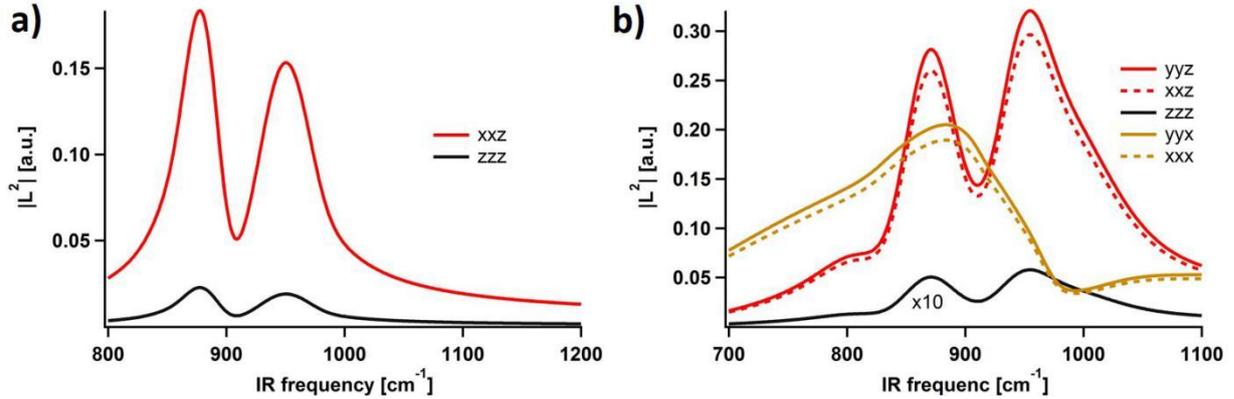
Figure 6. 2 Calculated local Fresnel factor of α-Al$_2$O$_3$(0001): a) under UHV measurement geometry (Vis/IR) 60°/36° and b) under ambient measurement geometry(Vis/IR) 54°/61°

6.3 SFG results of surface phonon of α-Al₂O₃(0001)

6.3.1 SFG results under UHV conditions

To understand the manner in which surface reconstruction induced by water adsorption is reflected in water induced changes in the surface phonon spectral response, it is a prerequisite to know the surface phonon spectral response of the water free α-Al$_2$O$_3$(0001) surface. Both theory[8, 27] and experimental observations suggest that the so-called Al-I termination is the most thermodynamically stable structure for UHV prepared α-Al$_2$O$_3$(0001) and that surface preparation using Ar$^+$ sputtering and annealing in oxygen at high temperatures recovers this termination (see section 2.1.2 in chapter 2 for more details).

Figure 6. 3 displays SFG spectra collected from samples preparared in and analyzed under UHV conditions: the α-Al$_2$O$_3$(0001) Al-I terminated clean surface and this surface with sub-monolayer water coverages (that flashed to 250 and 300 K with coverage 0.5 and 0.26 eML respectively, as discussed in chapter 4). The ppp spectra collected at different azimuthal angles (see the polar plot in Figure 6. 3a of integrated I$_{sfg}$ under ppp polarization in the region 920 cm^{-1} ~1040 cm^{-1}) clearly demonstrate a C$_{\infty v}$ symmetry of the SFG Al-O response of UHV prepared α-Al$_2$O$_3$(0001). Figure 6. 3b shows the ppp spectra of all the three UHV prepared samples (clean and with dissociative water adsorbed surfaces) where an intensive peak appeared at around 980 cm^{-1} appears for all of them. In addition, ppp spectra does not change after water adsorption and the shape overlaps with each other of the three samples. The same response of SFG in Al-O vibration of both clean and water dissociated surfaces suggests UHV prepared water dissociative adsorption on the Al-I terminated surface does not cause obvious changes

in SFG response in Al-O phonon vibration region. Since in this work we measured SFG spectra under different geometries between UHV and ambient which result in different Fresnel factor, it is necessary to analyze the data with Fresnel factor corrected fitting method with equation 2.21 together with equation 2.24. As for the $C_{\infty v}$ symmetry for the samples prepared in UHV, the ppp SFG spectra is contributed by two components χ_{aac} and χ_{ccc}. As a result of the fitting procedure, there are two resonances centered at 853 ± 17 cm^{-1} and 956 ± 8 cm^{-1} contributed to the SFG spectra for the UHV prepared samples.
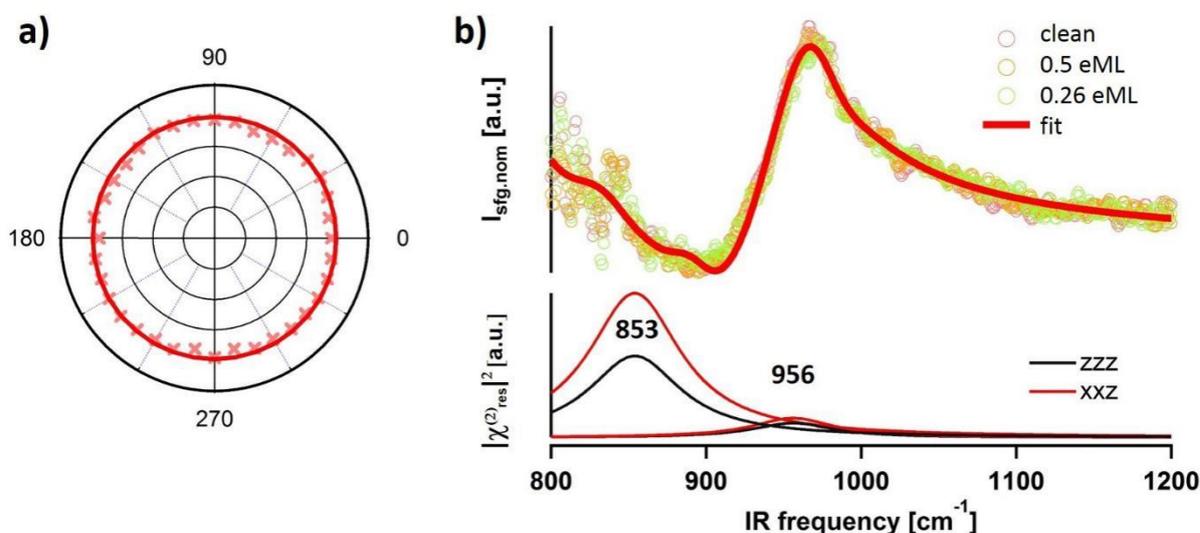
Figure 6. 3 SFG spectroscopy of UHV prepared α-Al2O3(0001): a) integrated I_{sfg} (under ppp polarization combination) versus azimuthal orientation ϕ (region from 920 cm^{-1} to 1040 cm^{-1}); b) ppp spectra collected at azimuthal angle $\phi = 0°$ for both the clean (in red circle) and sub-monolayer water adsorbed (0.26 eMLin green circle and 0.5 eML in yellow circle) and the fitted curve in solid line with equation 2.21 and 2.24, while the extracted $\chi^{(2)}_{res}$ is plotted in the bottom panel.

Table 6. 1 Fitting parameters of SFG data of UHV prepared samples

	χ_{aac}	χ_{ccc}
A_{nr}	0.56 ± 0.21	1.7 ± 0.04
θ_{nr}	0.54 ± 0.09	-0.42 ± 0.12
A_2	151 ± 50.1	154 ± 28.3
ω_2	853 ± 17	
Γ_2	35 ± 13	
θ_2	0.14 ± 0.06	-1.28 ± 0.02
A_1	48.8 ± 17.3	48.2 ± 18.8
ω_3	956 ± 8	
Γ_3	32 ± 4	
θ_3	1.04 ± 0.15	3.1 ± 0.25

Note: we employ the Levenberg-Marquart algorithm, as implemented in the data analysis program Igor Pro (Wavemetrics) to actually fit the data. For the analysis of the low frequency Al-O (H) response of one sample in

this work, we have assumed that the center frequencies and line widths of each resonance are the same for all the components of $\chi^{(2)}$ because all components of the $\chi^{(2)}$ sample the same underlying resonance.

6.3.2 SFG results in ambient conditions

In the previous study, it was demonstrated there was a 3-fold surface symmetry of Al-O SFG response for the fully hydroxylated α-Al$_2$O$_3$ (0001) surface in ambient. To quantitatively understand the surface reconstruction over different water coverage, both partially and fully hydroxylated surface were prepared in ambient and measured by SFG in ambient. Such an approach is possible because, as discussed above and in our previous work, surface (re)hydroxylation in air following mild heating takes weeks to month(s). As mentioned earlier, SFG spectra under both ppp and ssp polarization combinations are collected for both fully and partially hydroxylated surfaces. As shown below the information content of the two types of spectra is plainly different suggesting any appropriate line shape model must self-consistently fit both types of data.
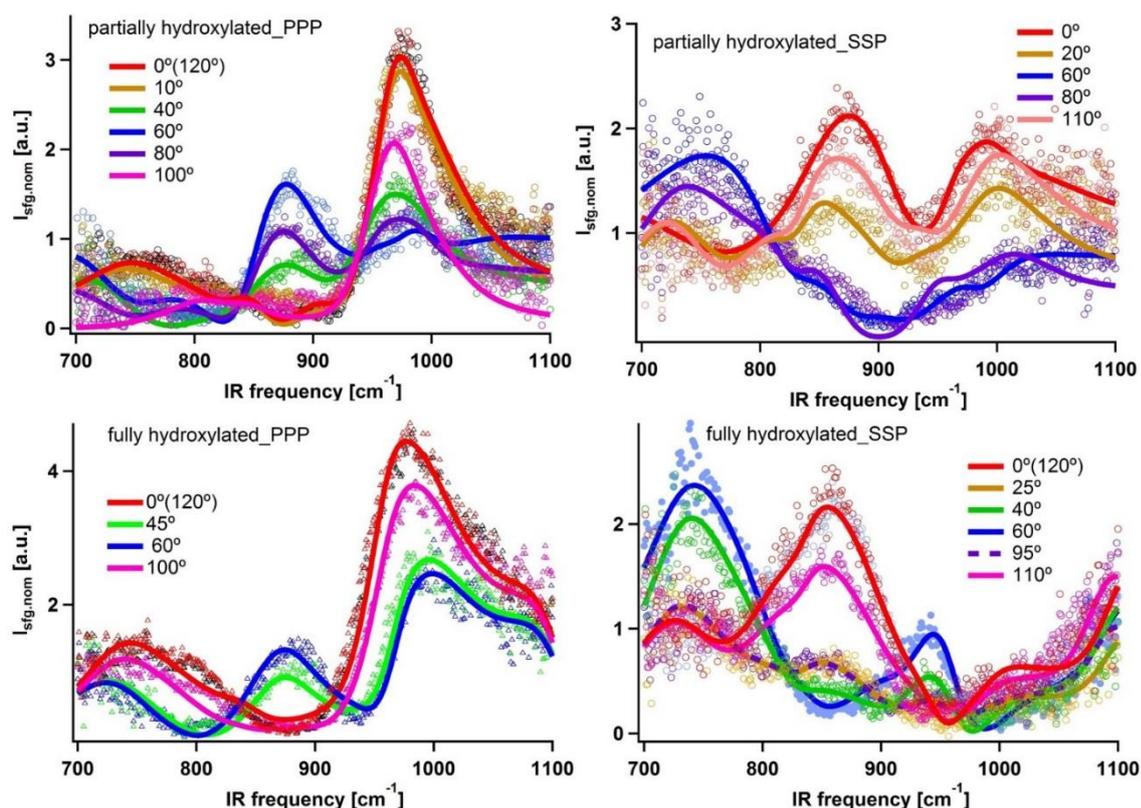
Figure 6. 4 Fitting results of SFG spectra at different azimuthal angle: top panel of partially hydroxylated surface; bottom panel of fully hydroxylated surface. The solid thick line is the fit curve with equation 2.19, 2.20 and equation 2.24 while the thin and noisy line is the data.

In order to know the symmetry of the surface phonon modes of the partially and fully hydroxylated surface, SFG spectra were collected as a function of azimuthal angle ϕ for both samples (see Figure 6.

4 for the data). Both the spectra response under ssp and ppp conditions can be most easily understood as having three fold symmetry at all infrared photon energies as the spectra collected at azimuthal angle 0 and 120 degrees overlap.
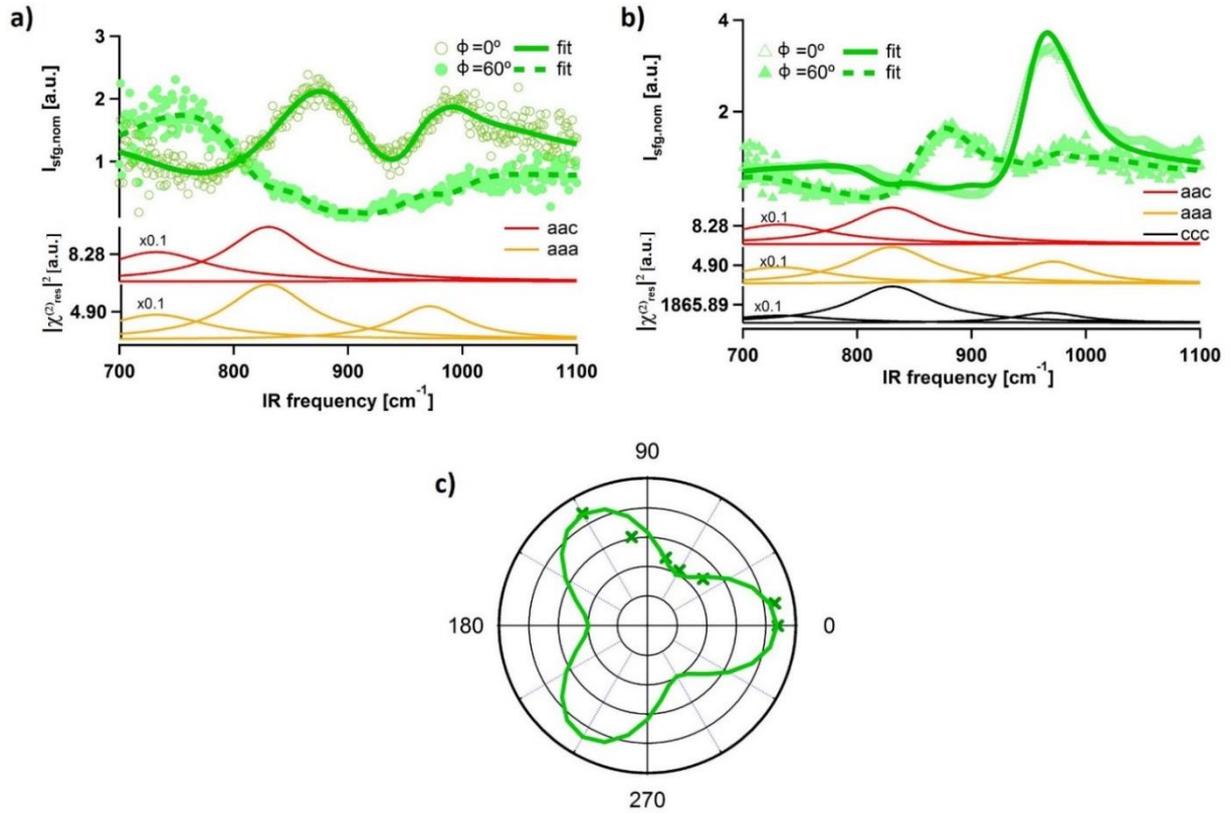
Figure 6. 5 SFG spectrascopy of phonon vibrations of partially hydroxylated α-Al$_2$O$_3$(0001): a) ssp spectra collected at azimuthal angle ϕ=0° and 60°; b) ppp spectra collected at azimuthal angle ϕ=0° and 60°; c) integrated I$_{sfg}$ versus azimuthal angle ϕ (fit data in solid line, region from 920 cm^{-1} to 1040 cm^{-1}).

Since in the region 920 cm^{-1} to 1040 cm^{-1} both from the Fresnel factor plot in Figure 6. 2 (one peak feature) and the following SFG data analysis, the SFG spectra should be dominated by one resonance not by multiple ones (for data fitting the least number of resonances should be applied because numerically there is no up-limitation of how many resonances used for fitting). While the C$_{3v}$ symmetry is suggested by the spectra plotted above it can be more straightforwardly illustrated if we once again, as above, construct a polar plot of the integrated SFG intensity of the spectra collected under the ppp polarization condition between 920 cm^{-1} and 1040 cm^{-1} in infrared photon energy. The result of this analysis is plotted in Figure 6. 5c, it indicates that for the partially hydroxylated surface it carries out again a 3-fold symmetry for the Al-O surface phonon vibrations as we learned for the fully hydroxylated ones in previous study. We do not make the polar plot again for the fully hydroxylated sample, as the ppp spectra in the region 920 cm^{-1} and 1040 cm^{-1} shows the same dependence on ϕ as that of partially hydroxylated surface (the intensity max. at ϕ=0° (120°) and min. at ϕ=60°). The solid thick lines in

Figure 6. 4 are the results of fits to the data using equations 2.19 (ssp), 2.20 (ppp) and 2.26 (line shape model). All spectra, i.e. different polarizations and azimuthal angles, from the same type of sample, i.e. partially or fully hydroxylated, are fit simultaneously. The resonances extracted from the fit for SFG spectra collected at azimuthal angle $\phi=0°$ under the ssp polarization condition and $\phi=60°$ under ppp are shown in Figure 6. 5.

Table 6. 2 Fitting parameters of SFG on partially hydroxylated α-Al$_2$O$_3$(0001)

	χ_{aac}	χ_{aaa}	χ_{ccc}
A_{nr}	2.88 ± 0.297	3.6 ± 0.163	17.28 ± 1.13
θ_{nr}	-2.99 ± 0.09	-1.39 ± 0.12	2.72 ± 0.078
A_1	532 ± 103	372.5 ± 42.1	4853 ± 62.7
ω_1		732.42 ± 6.09	
Γ_1		56 ± 6.31	
θ_1	-1.8 ± 0.08	0.4 ± 0.06	-1.9 ± 0.08
A_2	179 ± 41.7	137 ± 30.1	2691 ± 76
ω_2		830.32 ± 5.31	
Γ_2		44 ± 4.12	
θ_2	2.14 ± 0.058	-0.6 ± 0.015	2.35 ± 0.04
A_1	17.8 ± 3.33	89.3 ± 7.83	1179 ± 22.6
ω_3		971.2 ± 2.36	
Γ_3		36.9 ± 1.92	
θ_3	-0.18 ± 0.031	-0.01 ± 0.012	1.9 ± 0.028

Above we discussed the Al-O vibration symmetry of samples prepared in ambient by measuring SFG vs ϕ. In the following we are going to discuss the fitting results of the extracted resonances. For the ssp spectra of partially hydroxylated surface, the extracted second order nonlinear susceptibility χ_{aac} and χ_{aaa} are plotted below the spectra (with equation 2.19 and 2.24) in Figure 6. 5a. Similarly, ppp spectra collected as a function of azimuthal angle from the partially hydroxylated surface were globally fit with Equation 2.20 and 2.24. Since we could obtain all parameters for both χ_{aac} and χ_{aaa} from ssp data fitting, the χ_{ccc} component can be reliably obtained from ppp data fitting (shown in Figure 6. 5b). The results of this analysis suggest our data can be understood as the result of resonances centered at 732 ± 6 cm^{-1}, 830 ± 5 cm^{-1} and 971 ± 2 cm^{-1} that each contributes to both ssp and ppp spectra. Since the resonance at 732 cm^{-1} lies in the edge of the spectrum of our infrared source, and thus at these IR wavelengths the resulting measured SFG intensity is relatively noisy, we will focus on the resonances located at 830 and 971 cm^{-1}. Both of these resonances contribute to χ_{aaa} while χ_{ccc} and χ_{aac} are dominated by the former. All the parameters resulting from the fitting are listed in Table 6. 2.

Again we apply the same data analysis approach to understand the fully hydroxylated surface. Figure 6. 6 shows the SFG spectra in the Al-O vibrational region of ambient prepared fully hydroxylated α-Al$_2$O$_3$(0001). As already shown above in Figure 6. 4 the SFG response in the phonon region shows 3-fold symmetry. Here we present spectra collected at $\phi = 0°$ and $60°$ for discussion under both ssp (Figure 6. 6a) and ppp (Figure 6. 6b) polarization combinations. SSP spectra at $\phi = 0°$ show an obvious peak at

around 860 cm^{-1} that disappears in spectra collected at $\phi = 60°$. In contrast spectral features at 750 cm^{-1} and 940 cm^{-1} appear to have a minimum at 0° and a maximum at 60°. PPP spectra seem much similar to that of the partially hydroxylated surface (as shown in Figure 6. 5b). At $\phi=0°$ a strong peak appears around 1000 cm^{-1} while a dip is present at 880 cm^{-1}. But clearly the 1000 cm^{-1} feature (a peak centered at 980 cm^{-1} in the fitting) becomes much broader and develops a shoulder at higher frequencies as one moves from the partially to the fully hydroxylated surface. While three resonances were sufficient to describe the partially hydroxylated surface spectral response, 4 resonances, in equations 2.24 are required for global fitting of the fully hydroxylated surface (the additional resonance is necessary to capture the high frequency shoulder). The result of this analysis suggests the four resonances are centered at 716±10 cm^{-1}, 825±6 cm^{-1}, 940±5 cm^{-1} and 1090±5 cm^{-1}. All other parameters of the fit are shown in Table 6. 3. The spectral change for both ssp and ppp data with the amount of adsorbed water species on the surface (from partially to fully hydroxylated) also demonstrates we are probing surface Al-O vibrations.
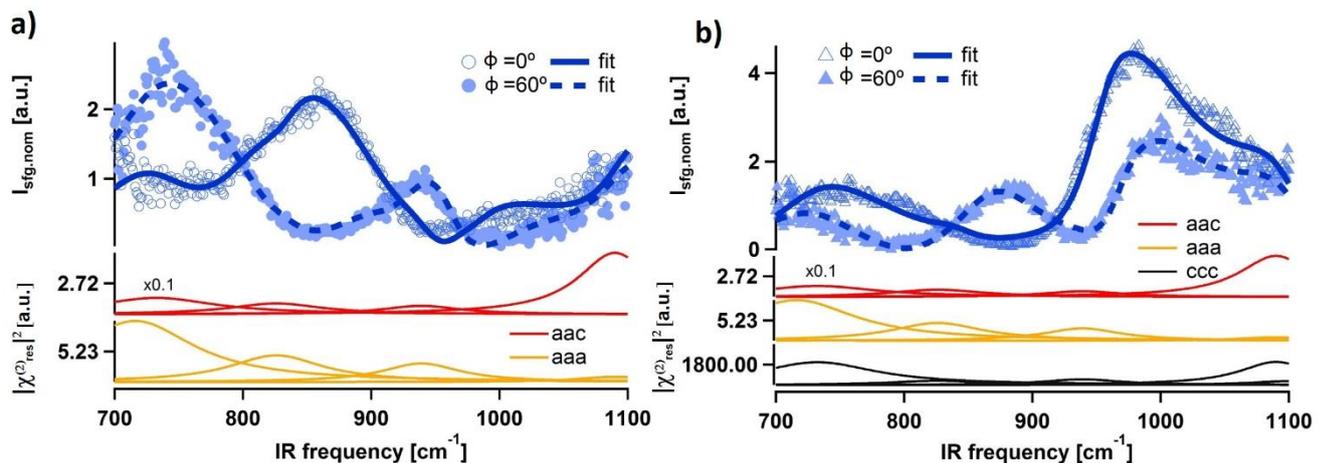
Figure 6. 6 SFG spectroscopy of phonon vibrations of fully hydroxylated α-Al$_2$O$_3$(0001): a) ssp spectra collected at azimuthal angle $\phi = 0°$ and 60°; b) ppp spectra collected at azimuthal angle $\phi = 0°$ and 60°.

Since the laser system used for ambient SFG measurement has a limitation to 700 cm^{-1} (low wavenumber side), we would properly like to focus our discussion mainly on the resonances that located at higher frequency region >800 cm^{-1}. To sum up the above SFG observations for all the samples: the fully hydroxylated, partially hydroxylated and UHV prepared surfaces, we can easily find that both the surface symmetry and the spectra appearance change dramatically between them: i. for the ambient prepared surfaces (both fully and partially hydroxylated), it is found to be 3-fold symmetry in Al-O SFG response while the UHV prepared and UHV measured samples Al-O phonon vibrations displays $C_{\infty v}$ symmetry in the SFG response; ii. the spectra with the ppp polarization combination clearly show that there is an additional resonance at higher frequency around 1090 cm^{-1} that appears only on the fully hydroxylated surface. Besides these differences, all SFG spectra exhibit two resonance features: one in the region 825

cm^{-1} ~ 850 cm^{-1} and the other in 940 cm^{-1} ~ 970 cm^{-1}. To better understand the surface reconstruction, I assign the experimentally observed resonances to the surface structures by referring to theoretical calculated phonon vibrations of both clean and hydroxylated surfaces in the following section.

Table 6. 3 Fitting parameters of SFG data on fully hydroxylated α-Al$_2$O$_3$(0001)

	χ_{aac}	χ_{aaa}	χ_{ccc}
A_{nr}	-2.47 ± 1.03	-1.12 ± 0.59	-41.8 ± 0.46
θ_{nr}	0.96 ± 0.05	0.83 ± 0.08	0.5 ± 0.03
A_1	336 ± 84	-181.5 ± 40	5900 ± 119
ω_1		716 ± 10	
Γ_1		56 ± 5	
θ_1	3.43 ± 0.065	2.22 ± 0.102	4.2 ± 0.02
A_2	-43 ± 10.25	-94.7 ± 20	-845 ± 47
ω_2		825.7 ± 6	
Γ_2		44.2 ± 5	
θ_2	1.97 ± 0.058	0.84 ± 0.06	0.14 ± 0.05
A_3	-32 ± 12.7	-66 ± 22	-821.8 ± 27
ω_3		939.4 ± 5	
Γ_3		35 ± 4	
θ_3	2.38 ± 0.015	3.32 ± 0.02	2.16 ± 0.03
A_4	81.5 ± 16	33 ± 15	-1579 ± 41
Ω_4		1090 ± 5	
Γ_4		35 ± 7	
θ_4	1.96 ± 0.02	0.91 ± 0.01	-0.07 ± 0.03

6.4 Comparison of the experimental observations with the theory

Our collaborator Giacomo Melani from Peter Saalfrank's group in Postdam University followed the theoretical method as applied in our previous work [19] and in chapter 2: periodic density functional theory in the Kohn−Sham scheme and supercell models were employed to describe the adsorption of water on α-Al$_2$O$_3$ (0001). The DFT calculations [28] were carried out with the Vienna Ab Initio Simulation Program, version VASP5.2, employing the Projector Augmented Wave (PAW) method[29, 30]. Exchange and correlation were treated in the Generalized Gradient Approximation (GGA) using the Perdew-Becke-Ernzerhof (PBE) function[31]. A plane-wave cutoff of 400 eV and Grimme's D2 correction [28], to account for dispersion interactions, were adopted. These settings were applied for a slab model of the (0001) surface. For the structure of clean surface, Al-I termination was chosen as this was shown to be the most stable both in prior theoretical [5, 32] and experimental studies [4, 6, 27].

Figure 6. 7a shows the side (top panel) and top views (bottom) of the 25 atom layers thick and 2x2 super cell structures of the water free Al-I termination of α-Al$_2$O$_3$(0001). Two water molecules dissociated (Figure 6. 7b, in a 2x2 super cell, there are 4 active Al sites for water adsorption, which is defined as 1 tML, when 2 water molecules dissociated on this super cell, it is 0.5 tML)) to mimic the partially hydroxylated surface prepared in ambient and fully hydroxylated (Figure 6. 7c) α-Al$_2$O$_3$(0001) surfaces. The atomic layer sequence of the 1x1 unit cell of the Al-I terminated clean surface is AlO3AlAlO3-R; while for the fully hydroxylated surface, the atomic layer sequence of 1x1 unit cell is (H)O3AlAlO3-R where the outmost Al layer is missed compared with Al-I termination. To compare experimentally observed surface Al-O resonances with theory, normal modes are calculated in the harmonic approximation by diagonalizing the dynamical matrix at the Γ-point of all the three cases. For the normal modes that vibrate below 800 cm^{-1}, they are contributed mainly by the bulk while the surficial Al-O vibrates above that can be clearly seen in the animation file provided by our cooperator.
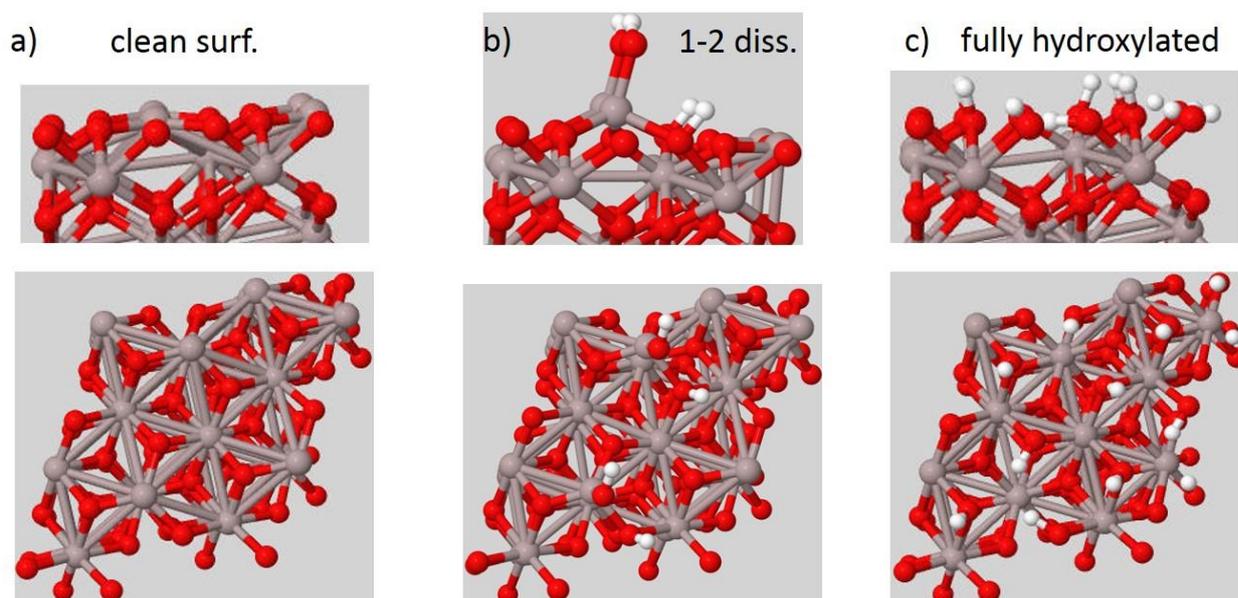
Figure 6. 7 (a) Slab used to calculate properties of the Al-I terminated α-Al$_2$O$_3$(0001) clean surface; (b) Slab used to calculate two water molecules dissociated on Al terminated α-Al$_2$O$_3$(0001) surface; (c) Slabs used to calculate fully hydroxylated α-Al$_2$O$_3$(0001) surface properties; top panel the side-view, bottom panel the top-view, each of the 2 x 2 super cell; O atom in red, Al atom in grey and H atom in white.

Figure 6. 8 displays the results of the calculated normal mode frequencies of the clean (in red), with two water molecules dissociatively adsorbed (in green), and the fully hydroxylated surface (in black). The observed resonances in SFG experiment located in the frequencies that of calculated normal modes, and also we found in theory the frequency results of (0001) is not sensitive to the size of the model applied (from 10 to 36 atom layers, no obvious change in the frequency) which in some extent make us confident with the theory frequencies (not like that for the (11-20) surface in chapter 5 where the calculated normal modes are scaled as the observed SFG resonances appears at higher frequencies than the theory, and

also the theory frequency shows dependence on model size). As discussed above, in practice our SFG spectra in UHV are restricted to infrared photon energies greater than 800 cm^{-1}. As a result here we only discuss the calculated phonon vibrations above this frequency.
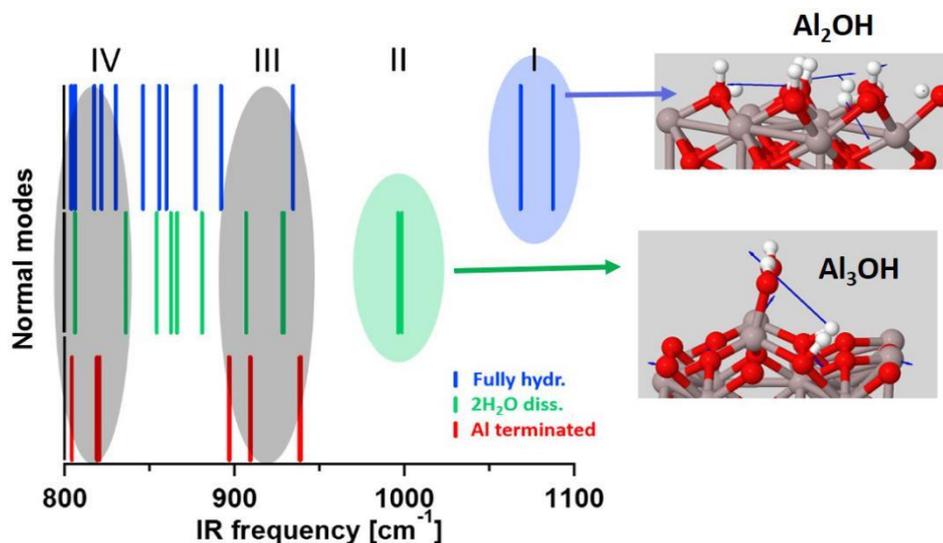
Figure 6. 8 Calculated normal modes of the phonon vibrations of Al terminated clean α-Al$_2$O$_3$(0001) surface (in red), with two water dissociated (in green) on 2x2 super cell and fully hydroxylated (in black), respectively.

As can be seen in Figure 6. 8, there are five vibrational modes for the Al terminated clean surface in theory. Clearly instrumental resolution and line broadening in the condensed phase would suggest that we should not expect to see all five in experiment. We would therefore consider in theory there are two vibrational 'zones', i.e. ~820 cm^{-1} (IV) and ~930 cm^{-1} (III) for the normal modes of clean surface. Figure 6. 8 suggests that: I) these two vibrations zones (III and IV) also appear for 0.5 tML water adsorbed surface and fully hydroxylated surfaces; II) there is an additional vibrational mode present at higher frequency, i.e. ~1000 cm^{-1}, for surface the (0001) surface with 0.5 tML dissociated water adsorption which is from the bending vibration of surface Al$_3$OH (triply coordinated surface hydroxyl groups) species; III) For the fully hydroxylated surface even higher frequency vibration modes show up at around 1100 cm^{-1} due to the bending vibration of surface Al$_2$OH (doubly coordinated hydroxyl groups, see Figure 6. 7c and Figure 6. 8).

This theory result supports our experimental observations at several points: in experiment a resonance centered at highest frequency, i.e. 1090 cm^{-1}, was only observed on the fully hydroxylated surface prepared in ambient; for both UHV (clean and with dissociated water) and ambient prepared fully hydroxylated samples we observed two additional resonances that appeared in lower frequency regions: 825-850 cm^{-1} and 940-956 cm^{-1}, consistent with theoretical predictions that for all the surfaces there is vibrational zone IV approximately ~820 cm^{-1} and zone III ~930 cm^{-1}. For the partially hydroxylated surface, two resonances centered at 830 and 970 cm-1 are observed in experiment while as predicted for

0.5 ML water dissociated surface in theory there should be possibly three vibrational zones centered at 820 cm^{-1}(IV), 930 cm^{-1}(III) and 1000 cm^{-1} (II).

For the assignment between theory and experiment, there are two points which need further discussion. I) the mismatch in the frequency between the experiment extracted 853 cm^{-1} and theoretically predicted ~820 cm^{-1} of the UHV prepared samples, which could be caused by the large uncertainty (±17 cm^{-1}) of data fitting process on this surface; because only overlapped SFG spectra under one polarization were obtained for UHV prepared samples, which resulted in the lack of constrain when applying global fitting to the data. II) A resonance centered at 970 cm^{-1} was observed for partially hydroxylated surface in SFG spectra while in theory there is normal mode at around 1000 cm^{-1}. The possible explanation could be: a) as we do not know the exact water coverage of this ambient prepared partially hydroxylated surface, the model with 0.5 tML water dissociated on the surface maybe is not the case for the partially hydroxylated surface; b) we fit the SFG data in the region 900~1000 cm^{-1} of partially hydroxylated surface with one broad resonance which turns out to be centered at 970 cm^{-1}, but in fact this should be contributed by both vibrational regions 930 cm^{-1}(III) and 1000 cm^{-1} (II). But what we are confident is that, with more and more water dissociated on the surface, higher and higher frequency normal modes should appear for (0001) surface. This is in good agreement with what we observed in SFG response.

Table 6. 4 Comparison between experimentally observed resonances in Al-O region and normal modes in theory.

	clean		partially hydroxylated		fully hydroxylated		
exp.(cm^{-1})	853±17	956±8	830±5	970±2	825±5	940±2	1090±3
theory(cm^{-1})	~820	~930	~820	~930, ~1000	~820	~930	~1100

Table 6. 4 lists the experimentally obtained resonances in Al-O region and theoretically predicted normal modes for clean, partially and fully hydroxylated surfaces, respectively, which clearly shows the consistence between theory and experiment especially for the clean and fully hydroxylated surfaces. Based on this assignment, we are able to conclude that for UHV prepared samples in this work it is Al-I termination; for ambient prepared fully hydroxylated surface in this work it is O-terminated (as shown in Figure 6. 7).

Here we would like to discuss more about the reactivity (here referring to kinetics of water dissociation on alumina) of this two terminations based on our experiment observations. The SFG responses of UHV prepared surfaces that with dissociative water adsorption have no change compared with that of clean

surface. If the water coverage for these two surfaces (with 0.26 and 0.5 eML) was something around 0.5 tML(2 water on 2x2 super cell), some additional resonance around 1000 cm^{-1} should be possibly visible in SFG spectra but in our experiment this was not the case, only two resonances centered at 853 and 956 cm^{-1} are observed. Or there is another possibility that both the 2 water dissociatively adsorbed on 2x2 super cell is not the most thermodynamically favored, which means molecular adsorption may also happens. This suggests UHV prepared water adsorbed surfaces have a coverage lower than 0.5 tML even that was flashed to relatively low temperature as 250 K or the theory structure is not the thermodynamically favored ones. However, for the ambient prepared partially hydroxylated surface which is generated by heating the fully hydroxylated surface at 500 K shows a higher frequency resonance located at 970 cm^{-1} which should be contributed by the bending vibration of surface Al$_3$OH which appears for 0.5 ML water dissociated surface as predicted in theory. From this point of view, we can come to such a conclusion that Al-I terminated (0001) is relatively inert towards water dissociation, if two water molecules were put on a 2 x 2 super cell they do not necessarily both dissociatively adsorb on the surface.

With the above discussion, we are confident to come to this conclusion: for the UHV prepared clean surface, it is Al-I termination with atomic sequence as AlO3AlAlO3-R and there is C$_{\infty v}$ symmetry for the Al-O SFG response; for the fully hydroxylated surface that pre-treated in HNO$_3$ solution, the surface is uniformly hydroxylated and the termination changed to be O-termination with atomic sequence as O3AlAlO3-R while the surface presents a 3-fold symmetry for Al-O SFG response. Only dosing water in UHV on the Al-I termination won't remove the Al layer but chemical etching does. The reactivity with water strongly depends on the termination that Al-I termination presents significant inertness towards water adsorption while the O termination instantly gets hydrated.

Therefore, any preparation procedures that may result in different terminations of α-Al$_2$O$_3$(0001) should be carefully considered when talking about the reactivities with water of this surface. In addition, the macroscopic surface properties like IEPs, water contact angle and so on will also be affected by the types of termination.

6.5 Conclusion

To understand the surface and termination of α-Al$_2$O$_3$(0001) under both UHV and in ambient is of crucial importance to understand its reactivity and performance in applications. In this work, we prepared and measured both clean surface and with sub-monolayer water adsorbed in UHV chamber, and sample that prepared in ambient to understand how the surface structure change with different amount of water adsorption. This also allows us to look insight into the reactivity of this surface with water dissociation. To characterize the surface structure we applied SFG spectroscopy, which is surface specific for center symmetry material α-Al$_2$O$_3$(0001), to probe the surface phonon vibrations. To do better assignment of

SFG data to the surface structure, we calculated the normal modes of phonon vibrations with a big model 2x2 super cell with 25 atom layers which allows to mimic both clean and hydroxylated surfaces with different coverages.

As a result, it is found the phonon modes of the clean surface under UHV conditions exhibit a $C_{\infty v}$ symmetry and this symmetry does not change with sub-monolayer coverages of water. On the other hand, those of the fully hydroxylated surface prepared and analyzed in ambient show 3-fold symmetry. These symmetry differences have been understood as the different chemical identities and geometrical configurations of the surface groups.

Consistent with previous work by us and others [10], it is found the Al-terminated surface is extremely inert toward hydroxylation in UHV, on the other hand, the hydroxylated surface is very sensitive to heating in ambient. Our SFG spectra show that the hydroxylated groups on the surface can be easily disrupted by heating while the reverse process in ambient is much slower.

From this work, two points could be extracted and they are of crucial importance to help understand many previous investigations on this c-plane especially those have conflicts or disagreement with each other:

1. Ambient preparation methods will result in different terminations: acid or base etching will presumably make Al-I terminations unlikely because of the dissolution of the topmost Al layer.
2. Al-I terminated is inert towards water dissociative adsorption while O-terminated (0001) could instantly get hydroxylated in air.

Elam et al. reported they created a hydroxylated (0001) surface by exposing the chemically etched sample with water at 10^{-2} bar pressure for 1 minute [1]. Along similar line others reported a uniformly hydroxylated surface in ambient conditions [16]. As noted above, recent work by us and others paint a very different picture [10, 27] [11]. For samples known to have the Al-I termination (the thermodynamically favorable in UHV) rates of water dissociative adsorption are very slow: weeks sitting on a laboratory bench in air is not sufficient to fully hydroxylate the surface. This difference can be understood by accounting for the pre-treatment of the α-Al$_2$O$_3$(0001) crystal in each work. In our and Kimmel's work the surface was prepared in UHV without any treatment in acid or strong base before or after delivering it to the chamber. As discussed above we expect in both groups the resulting surface termination was the Al-I (and that this termination is relatively inert with respect to water dissociative adsorption). In contrast Elam et al boiled their sample in phosphoric acid at 500 K for 3 min, presumably generating an O-terminated surface that is much more reactive towards water, thus they get a hydroxylated surface when exposing it in high water pressure.

Another big issue people confused a lot is the IEPs of α-Al$_2$O$_3$(0001) which varies from work to work over pHs from 3-8[13, 17]. Once again, much of this variability in isoelectric points can be rationalized by accounting for sample preparation. As we describe above the two different surface terminations have different types of surface oxygens – the oxygen terminated surface is dominated by doubly coordinated O, the Al-I terminated has a relatively sizable population of triply coordinated ones. Because each of these types of surface oxygens are expected to have different acidities, surface preparations that result in mixed terminations would be expected, as indeed is observed, to have widely differing IEPs. Previous attempts to rationalize these differences have invoked differing sample thermal histories, UV treatment, roughness or miscut as possible explanations for the IEP variability[33]. While we cannot dismiss the importance of these factors this study suggests that the *way* in which such sample preparation factors would affect measured IEP is by producing different surface terminations and that IEP variability can occur even in the absence of miscut or surface structural defects.

In addition, the spectral response of SFG spectrum in pH dependent study of water/α-Al$_2$O$_3$(0001) system that investigated in different group behaves quite differently[12, 14, 15] as mentioned earlier. Although they all cleaned the samples with chemical etching, but some with acid while others with strong base also the annealing temperature differed, this could possibly affect the surface termination thus change the spectral response; also in the solution side different ion strength or types (they use different kinds of salt in the solution) in these studies will be another reason for the different SFG response of OH stretching vibrations, because OH stretching at the interface not only could be contributed by the substrate side but also the solution side.

By investigating Al-O vibrations with SFG-DFT combined approach as in this work, we are able to identify the surface terminations that prepared with different procedures and to distinguish the types of surface Al-OH groups without influence from the liquid side. As discussed above, the conclusions of this work help get insight into the microscopic structure of the interface of water/α-Al$_2$O$_3$(0001). This interface is so important in surface science as it is intimately connected to many surface macroscopic properties and phenomena. More important, this experimental approach for surface phonon investigation can also be extended to other water/metal oxides systems.

6.6 References

1.   Elam, J.W., et al., *Adsorption of H$_2$O on a single-crystal α-Al$_2$O$_3$(0001) surface.* The Journal of Physical Chemistry B, 1998. **102**.

2.   Eng, P.J., et al., *Structure of the hydrated α-Al$_2$O$_3$(0001) surface.* Science, 2000. **288**: p. 1029−1033.

3.   French, T.M. and G.A. Somorjai, *Composition and surface structure of the (0001) face of α-alumina by low-energy electron diffraction.* The Journal of Physical Chemistry, 1970. **74**(12): p. 2489-2495.

4.   Guénard, P., et al., *Determination of the α-Al$_2$O$_3$(0001) surface relaxation and termination by measurements of crystal truncation rods.* Surface Review and Letters, 1997. **5**: p. 321-324.

5.   Marmier, A. and S.C. Parker, *Ab initio morphology and surface thermodynamics of α-Al$_2$O$_3$.* Physical Review B, 2004. **69**(11): p. 115409.

6.   Soares, E.A., et al., *Structure of the α-Al$_2$O$_3$(0001) surface from low-energy electron diffraction: Al termination and evidence for anomalously large thermal vibrations.* Physical Review B, 2002. **65**(19): p. 195405.

7.   Hass, K., et al., *The chemistry of water on alumina surfaces: reaction dynamics from first principles.* Science, 1998. **282**: p. 265-268.

8.   Wirth, J. and P. Saalfrank, *The chemistry of water on α-alumina: kinetics and nuclear quantum effects from first principles.* The Journal of Physical Chemistry C, 2012. **116**(51): p. 26829-26840.

9.   Wang, B., et al., *Density functional/all-electron basis set slab model calculations of the adsorption/dissociation mechanisms of water on α-Al$_2$O$_3$(0001) Surface.* The Journal of Physical Chemistry C, 2011. **115**(27): p. 13399-13411.

10.   Tong, Y., et al., *Optically probing Al-O and O-H vibrations to characterize water adsorption and surface reconstruction on alpha-alumina: an experimental and theoretical study.* The Journal of Chemical Physics, 2015. **142**(5): p. 054704.

11.   Petrik, N.G., et al., *Molecular water adsorption and reactions on α-Al$_2$O$_3$(0001) and α-alumina particles.* The Journal of Physical Chemistry C, 2018. **122**(17): p. 9540-9551.

12.   Flörsheimer, M., et al., *Hydration of mineral surfaces probed at the molecular level.* Langmuir, 2008. **24**(23): p. 13434-13439.

13.   Smit, W., et al., *Zeta-potential and radiotracer adsorption measurements on EFG α-Al$_2$O$_3$ single crystals in NaBr solutions.* Journal of Colloid and Interface Science, 1980. **78**(1): p. 1-14.

14.   Braunschweig, B., S. Eissner, and W. Daum, *Molecular structure of a mineral/water Interface: effects of surface nanoroughness of α-Al$_2$O$_3$(0001).* The Journal of Physical Chemistry C, 2008. **112**(6): p. 1751-1754.

15.   Zhang, L., et al., *Structures and charging of α-Alumina (0001)/water interfaces studied by sum-frequency vibrational spectroscopy.* Journal of the American Chemical Society, 2008. **130**(24): p. 7686-7694.

16.   Richardson, H., et al., *Freezing of water on alpha-Al$_2$O$_3$ surfaces*, in *Physics and Chemistry of Ice: proceedings of the 11th International Conference on the Physics and Chemistry of Ice*. 2007, The Royal Society of Chemistry: Bremerhaven, Germany. p. 513.

17.   Yeganeh, M., et al., *Vibrational spectroscopy of water at liquid/solid interfaces: crossing the isoelectric point of a solid surface.* Physical Review Letters, 1999. **83**(6): p. 1179-1182.

18.   Tuladhar, A., S.M. Piontek, and E. Borguet, *Insights on interfacial structure, dynamics, and proton transfer from ultrafast vibrational sum frequency generation spectroscopy of the alumina(0001)/water interface.* The Journal of Physical Chemistry C, 2017. **121**(9): p. 5168-5177.

19.   Heiden, S., et al., *Water dissociative adsorption on α-Al$_2$O$_3$(11-20) is controlled by surface site undercoordination, density, and topology.* The Journal of Physical Chemistry C, 2018. **122**(12): p. 6573-6584.

20.   Shen, Y.R., *The principles of nonlinear optics*. 1984, New York: Wiley-Interscience,. 575.

21.   Shen, Y.R., *Surface properties probed by second-harmonic and sum-frequency generation.* Nature, 1989. **337**: p. 519-525.

22.   Sung, J., Y.R. Shen, and G.A. Waychunas, *The interfacial structure of water/protonated α-Al$_2$O$_3$(11$\overline{2}$0) as a function of pH.* Journal of Physics: Condensed Matter, 2012. **24**(12): p. 124101.

23.   Sung, J., et al., *Surface structure of protonated R-sapphire (1-102) studied by sum-frequency vibrational spectroscopy.* Journal of the American Chemical Society, 2011. **133**(11): p. 3846-53.

24.   Wirth, J., et al., *Characterization of water dissociation on α-Al$_2$O$_3$((1-102): theory and experiment.* Physical Chemistry Chemical Physics, 2016. **18**(22): p. 14822-32.

25.   Tuladhar, A., et al., *Spectroscopy and ultrafast vibrational dynamics of strongly hydrogen bonded OH species at the α-Al$_2$O$_3$(11-20)/H$_2$O interface.* The Journal of Physical Chemistry C, 2016. **120**(29): p. 16153-16161.

26.   Boulesbaa, A. and E. Borguet, *Vibrational dynamics of interfacial water by free induction decay sum frequency generation (FID-SFG) at the α-Al$_2$O$_3$(11$\overline{2}$0)/H$_2$O Interface.* The Journal of Physical Chemistry Letters, 2014. **5**(3): p. 528-533.

27.   Kirsch, H., et al., *Experimental characterization of unimolecular water dissociative adsorption on α-alumina.* The Journal of Physical Chemistry C, 2014. **118**(25): p. 13623-13630.

28.   Grimme, S., *Semiempirical GGA-type density functional constructed with a long-range dispersion correction.* Journal of Computational Chemistry, 2006. **27**(15): p. 1787-99.

29.   Kresse, G.J., D., *From ultrasoft pseudopotentials to the projector augmented-wave method.* Physical Review B, 1999. **59**(3): p. 1758-1775.

30.   Blöchl, P.E., *Projector augmented-wave method.* Physical Review B, 1994. **50**(24): p. 17953-17979.

31.   Perdew, J.P., *Generalized gradient approximation made simple.* Physical Review Letters, 1996. **77**.

32.   Kurita, T., K. Uchida, and A. Oshiyama, *Atomic and electronic structures of α-Al$_2$O$_3$ surfaces.* Physical Review B, 2010. **82**(15).

33.   Lützenkirchen, J., et al., *The surface chemistry of sapphire-c: A literature review and a study on various factors influencing its IEP.* Advances in Colloid and Interface Science, 2018. **251**: p. 1-25.

Chapter 7 Summary and outlook

As discussed in the introduction, the surface structure of α-Al$_2$O$_3$ affects its performance in industrial applications dramatically. Even small amounts of water is known to change alumina's surface structure and chemistry. The purpose of this thesis is to gain insight into the interaction (adsorption structure and desorption) between water and α-Al$_2$O$_3$ under UHV conditions as well as the resulted surface structure changes induced by water adsorption as one moves from UHV to ambient conditions (with the attendant increase in water pressure). To investigate the microscopic structure of an interface where hydrogen (water) is involved is a challenge since most surface techniques (LEED, STM, XPS, etc.) are insensitive with hydrogen or not surface specific (like IR spectroscopy when we would like to probe surface phonon vibrations). The second order nonlinear spectroscopy SFG is surface-specific, sensitive to water at sub-monolayer coverages and sensitive to bonded hydrogen thus seems a good tool to gain insight into the problem in this thesis. However its application to this problem has challenges both with respect to measurement and data analysis:

1) It requires more effort to perform SFG measurements in a UHV chamber, especially for probing Al-O(H) vibrations, than to perform similar measurements in air: on the one hand, placing the sample in the UHV chamber makes the optical alignment more difficult both for signal generation and detection; on the other hand, the output of our laser system for photon energies in the long wavelength infrared range (> 10 μm for Al-O vibrations) is quite low (less than 4 μJ/pulse at the entrance window of the chamber) for our laser system (almost the limitation in the long wavelength side) and it decreases again at the window due to adsorption (window material like CaF$_2$ has strong adsorption in the long wavelength of IR) which in the end results a weak signal and possibly some additional signal that would be generated on the window. To solve this problem, KBr window is applied for surface phonon study in chapter 5 and 6. It is challenging to find UHV window materials that are both transmissive at long IR wavelengths and relatively inert (particularly with respect to humid lab air). Our initial attempts at these measurements use CaF2 which is relatively inert with respect to water. The windows we were able to procure were both somewhat absorptive at the IR wavelengths of interest and also lead to difficult to avoid spurious SFG generation (given the incident beam angles we could achieve in our chamber) presumably because of metal contamination. Midway through the thesis we located a vendor of KBr flanges with a protective coating (KBr is relatively hygroscopic). KBr is both more favorable than CaF$_2$ with respect to IR transmission and appeared to be more pure (SFG generation in the window was minimal).

2) Because α-Al_2O_3 is birefringent, its refractive index (n) depends on the polarization and propagation direction of light. This effect is particularly important for the surface phonon vibration in chapter 5 and 6, which is close or even partially overlapped with the bulk adsorption. Quantitative modeling of the surface phonon spectral response requires accounting for this, azimuthal angle dependent, birefringence by calculation of Fresnel factors for different polarizations of the incoming beams and on different cuttings of the crystal. To obtain the vibrational information of the interfacial groups, a Fresnel factor corrected global fitting method is applied in both chapter 5 and 6. For probing OD stretching vibration in chapter 3, it is not necessary to account for it because the stretching vibration is far away from the bulk adsorption.

3) In chapter 5 and 6 we also measured the azimuthal dependence of SFG response in Al-O vibration region, it demands a very stable sample mounting that guarantees the surface normal of the sample remains fixed (i.e. no tilt occurs) when rotating the crystal (the degree of tilting should be within 0.5 at the most). This requires much effort for the sample mounting inside the UHV chamber particularly because the sample is heated and cooled frequently during preparation and analysis.

4) In chapter 4 TPD is applied to study the desorption of small coverages of water (below 10% ML). For such samples even very slight desorption from the background will cause large errors in data analysis. Reaching such a small background in TPD requires both care in sample preparation and careful positioning of the QMS detector (it should be positioned as close as possible to the sample surface).

With all the above experimental challenges overcome, we are able to get insight into how water interacts with α-Al_2O_3 and, together with theory results, in what follows important findings and their implications are summarized.

For the interaction between water and alumina, much previous work has been done both theoretically and experimentally as discussed in chapter 1. To understand the mechanism of this interaction on the molecular-level, and because adsorption of even small amounts of water causes large changes in α-Al_2O_3 surface properties, the system of α-Al_2O_3 with sub-monolayer water in UHV is a good starting point. Adsorption of small amounts of water α-Al_2O_3 (0001) and (1-102) has been investigated in previous work [1-3] with a combined SFG-DFT approach. The third most thermodynamically stable surface, i.e. the (11-20), is less explored previously and is studied in this thesis in chapter 3 using the same suite of experimental (SFG spectroscopy) and theoretical approaches as in previous work in our group. This methodological similarity makes comparison and generalization about relative surface−water reactivity straightforward under UHV conditions. For all three surfaces, theory suggests that water with low coverage will firstly molecularly adsorb on the surface (with no adsorption barrier) and rapidly dissociate

(i.e. water dissociation has a barrier of <0.05 eV). The SFG results [1, 3] display resonances located in the OH(D) stretching vibrations that are consistent with theory predicted frequencies of the favorable adsorption structures. We have previously shown that on the Al-I terminated (0001) surface water dissociatively adsorbs forming 1-2 and 1-4 structures and on the O-I terminated (1-102) surface it dissociatively adsorbs forming the 1-4 structure. In this thesis we learn that water adsorption on the (11-20) surface is more complex. Here there are three sorts of favorable dissociatively adsorbed structures: inter-CUSa/Oμ2, CUSb/Oμ2 and inter-CUSb/Oμ2 (all the structures see chapter 3).

For the issue of the thermodynamics and kinetics of water ad/de-sorption on α-Al$_2$O$_3$ surfaces, some theoretical work has been done [1, 2, 4, 5]. Also in chapter 3 the kinetics of uni-molecular water dissociation on all the three surfaces is discussed based on DFT calculations (rate constant for water dissociative adsorption reaction). As discussed, uni-molecular water first adsorbs with $E_{ads-mol}$=-1.78[4], -1.48[1] and -1.40[2] eV on (11-20), (1-102) and (0001) surface, respectively; with tiny barrier, it will favorably dissociated on the surface and the rate constant for this step at 300 K on (11-20) is nearly two orders of magnitude higher than that on the other two surfaces[4]. However, to investigate this issue with experimental approaches is necessary because different theories and approximations[1] are used in calculation which yield different energies (e.g. two different exchange–correlation functions pure PBE and HSE06 result in different transition state for water dissociation); theory calculates the adsorption mechanism of one molecule on the surface but the mechanism of desorption is unclear: it may desorb from the same site where molecular adsorption happens or in a different way. While it is important to experimentally check the validity of theoretical adsorption structure, it's also worthwhile to demonstrate with experiment approaches with respect to the predicted adsorption thermodynamics and mechanisms. Nelson et al. studied the desorption energy of water from (0001) with TPD spectra which lies in a range 23 to 41 kcal/mol and assigned this to the different adsorption sites due to defects[6]. However, Hass's work suggests the adsorption energy is dependent on the coverage that it decreases fast at higher coverage based on first principle calculation[5]. In order to check the theories and to address the disagreement between previous studies, we study desorption process of water from all the three surfaces of α-Al$_2$O$_3$ with the same approach, TPD in chapter 4. By employing the same sample preparation and analysis approach for all three alumina surfaces comparison of the relative energies of water desorption from each becomes more straightforward.

Since we are interested in the desorption kinetics of uni-water molecule, samples with quite low water coverage were prepared for TPD measurement. For TPD data analysis, a method that is based on Polanyi-Wigner equation is applied in this work with a global fitting procedure (chapter 4). With this method we found the desorption energy of uni-molecular water on the α-Al$_2$O$_3$(11-20), (1-102) and (0001) surfaces to be 1.52, 1.42 and 1.28 eV respectively. The trend in desorption energy is consistent with theory where the desorption energies were found to be 2.27[4], 1.53[1] and 1.45[2] eV on the three

surfaces. Both experiment and theory suggest (11-20) is the most reactive surface, thus has the highest desorption energy, while the Al-I terminated (0001) surface is the most inactive towards water dissociation, and thus has the lowest desorption energy, among the three.

This work experimentally confirms previous theoretical predictions of water ad/de-sorption thermodynamics and kinetics [1, 2, 4, 5] at low coverages. In particular, the close correspondence between our measured desorption energy and the theoretical values predicted for the ideal (0001) surface place tight limits on the effect of surface structural defects on water reactivity for the well prepared 1x1 clean α-Al_2O_3 surface. In Nelson's work[6], they concluded that water desorption energy dropped in the range 23-41 Kcal/mol due to the adsorption at defects on the surface by simulation the TPD data with Reahead's peak maximum method which is applicable for 1st order desorption data analysis. They observed a series of TPD spectra with peak maximum shifting to higher temperatures as the coverage decreased which should be the feature of 2[ed] order desorption process thus could not be analyzed with Reahead's peak maximum method.

The TPD measurement and data analysis in this work can be easily implemented in other adsorbate/substrate systems. It helps evaluate the theoretical calculation from experiment point of view; in the other way around, it provides a way to get a reasonable adsorption energy for an adsorbate on a complex or unknown system, which is helpful for benchmarking thermodynamic calculations of the system.

The above work focused mainly on uni-molecular water interaction with alumina under UHV conditions. The interaction between water and alumina in ambient or with solutions is more relevant to industry and has been studied [2, 3, 5, 7-14] both in theory and experiment in prior work. However, there is disagreement among these previous studies especially on the water reactivity with alumina. It is generally considered that for (0001) surface prepared in ambient condition and measured in contact with liquid water, hydroxylation should readily take place [8, 12-15]. In contrast to this conclusion our previous work found it took almost a month to see clear evidence for water dissociative adsorption for a UHV prepared (0001) sample placed in ambient conditions [10]. In addition, surface properties like isoelectronic points IEPs also vary dramatically from work to work[15, 16] and people ascribe this to factors like heating treatment of the surface, the miscut, the roughness and so on. To understand these observations it is necessary to learn how the termination of alumina change with water adsorption. Therefore, in the last part of this work in chapter 5 and 6, we aim to understand how the termination changes with increasing water adsorption from UHV to ambient conditions.

To do so I studied the most water reactive surface, i.e. the (11-20) (chapter 5), and the least reactive, i.e. the (0001) (chapter 6), by probing the surface phonon (Al-O) vibrations with SFG spectroscopy. Combined with the DFT calculations (done by Dr. Sophia Heiden and Dr. Giacomo Melani in Prof. Dr.

Peter Saalfrank's group from University of Potsdam) under both ppp and ssp polarizations in UHV and ambient conditions as a function of rotation around the surface normal.

For α-Al$_2$O$_3$(11-20), we successfully probed SFG spectra changes in the Al-O vibrations in the range 900-1200 cm^{-1} for samples prepared in UHV (clean and water dissociatively adsorbed) and ambient conditions (fully protonated). Based on SFG data analysis, together with theoretical calculations of the normal modes, we learn that the UHV prepared clean (11-20) surface is O-I terminated[17] and is therefore composed of doubly coordinated Al$_2$O and triply coordinated Al$_3$O functional groups in a ratio of 1:2 (the former vibrate at higher frequencies around 1040 cm^{-1} while the later vibrate at lower frequencies around 970 cm^{-1} in SFG spectra). For this surface with sub-monolayer water coverages, composed exclusively of dissociatively adsorbed species, probing both Al-O vibrations in chapter 5 and hydroxyl stretching vibrations in chapter 3, suggests that for the O-I termination water dissociation is favorable at the inter-CUSa/Oµ2 (the most favorable structure at low coverage). Viewed in another way, only the Al$_2$O is active to be protonated while Al$_3$O stays unprotonated. For the fully protonated (11-20) surface in ambient, we propose a surface structure in theory which is supported by SFG experiment in probing surface phonon that is composed of AlO, Al$_2$O and Al$_3$O in a ratio of 1:1:1: the O-III termination in Kurita's work [17]. All three of these types of surface oxygens are protonatable. In addition, we find the O-I terminated surface could be easily fully protonated when it is moved to ambient environment; this allows us to get insight into how the O-I terminated clean surface with atomic squence (OO2Al4O2O-R) gets reconstructed into O-III termination (O2OOO2Al4O2O-R) in ambient. Now we know that O-III termination is the product of reaction between O-I and water adsorption: the top most two O layers of O-III are from water dissociation while the first singly coordinated O2 layer is from dissociated water on CUSb Al site and the second doubly coordinated O layer is from dissociated water that between two CUSa site (CUSa and CUSb are two kinds of surface Al of O-I termination structure), the below part is just the O-I termination.Our conclusions for the O-III termination of fully protonated (11-20) in one hand confirms a previous report by Catalano[18] with X-ray reflectivity method but which fails to give any information about H (the protonation state of terminal O). In Sung's work[19], they argued the Al$_3$O was difficult to get protonated except possibly under very acidic conditions while AlOH$_2$ existed given both the two H forming H-bond with the neighboring O which disagreed with what he interpreted about their SFG results.

The above findings of α-Al$_2$O$_3$(11-20) termination is of crucial importance when we want to discuss the surface macro-properties like charges which further affect the reactions with other species. What is more, the termination change from water free environment to ambient should be seriously considered especially when it is used as substrate to grow thin films or catalyst in industry since this may change the growth of the first atomic layer of the film due to the lattice change[20-24].

With the same SFG-DFT combined approach, the termination of the most thermodynamic stable surface α-Al$_2$O$_3$ (0001) is also investigated with interaction with water under both UHV and ambient conditions as discussed in chapter 6. For the UHV prepared clean surface, it is Al-I termination with atomic sequence as AlO3AlAlO3-R and there is C$_{\infty v}$ symmetry for the Al-O SFG response; for the fully hydroxylated surface created by pre-treatment in HNO$_3$ solution, the surface is uniformly hydroxylated and the termination changed to be O-termination with atomic sequence as O3AlAlO3-R while the surface presents a 3-fold symmetry for Al-O SFG response. The reactivity with water strongly depends on the termination. The Al-I termination is inert towards water adsorption while the O is instantly hydrated. Therefore, any preparation procedure that may result in different terminations of α-Al$_2$O$_3$(0001) should be carefully considered evaluating the reactivities with water of this surface.The macroscopic surface properties like IEPs, water contact angle and so on as a result will also be affected by the termination type. These findings are of crucial importance to help understand many previous investigations on this c-plane especially these have conflicts or disagreement with each other:

This disagreement on water reactivity of (0001) could be well understood based on this trend. Obviously in our work[10] we prepared the sample in UHV without any treatment in acid or strong base before or after delivering it into the chamber which will result in a Al-I termination (inert with water dissociation) while Elam[7] et al.boiled their sample in phosphoric acid at 500 K for 3 min which probably had generated O-termination. Another big issue people confused a lot is the IEPs of α-Al$_2$O$_3$(0001) which vary from work to work over the pH range 3 - 8[15, 16]. The results of this thesis offer two perspectives to rationalize this variability. Firstly one needs to accont for whether the preparation method of the sample results in an O-terminated or Al-terminated surface (since they have notably different acidities); secondly the solution used for IEPs measurement may already induce the surface reconstruction: when the crystal was soaked inside the solution, the first Al layer has dissolved and what was measured is another 'new surface'.

As a model material, the insight into interaction between water and α-Al$_2$O$_3$ including the reactivities and the surface reconstruction of alumina from UHV to ambient conditions provides inspiration to understand water interaction with other environmentally abundant alumino-silicate materials. The SFG-DFT combined approaches as applied in this thesis can also be extended to other water/metal oxides systems, and would be of general interest to those interested in oxide/water interaction or the processes such interactions control.

7.1 references

1.   Wirth, J., et al., *Characterization of water dissociation on α-Al$_2$O$_3$((1-102): theory and experiment.* Physical Chemistry Chemical Physics, 2016. **18**(22): p. 14822-32.

2.   Wirth, J. and P. Saalfrank, *The chemistry of water on α-alumina: kinetics and nuclear quantum effects from first principles.* The Journal of Physical Chemistry C, 2012. **116**(51): p. 26829-26840.

3.   Kirsch, H., et al., *Experimental characterization of unimolecular water dissociative adsorption on α-alumina.* The Journal of Physical Chemistry C, 2014. **118**(25): p. 13623-13630.

4.   Heiden, S., et al., *Water dissociative adsorption on α-Al₂O₃(11-20) is controlled by surface site undercoordination, density, and topology.* The Journal of Physical Chemistry C, 2018. **122**(12): p. 6573-6584.

5.   Hass, K., et al., *The chemistry of water on alumina surfaces: reaction dynamics from first principles.* Science, 1998. **282**: p. 265-268.

6.   Nelson, C.E., et al., *Desorption of H₂O from a hydroxylated single-crystal α-Al₂O₃(0001) surface.* Surface Science, 1998. **416**(3): p. 341-353.

7.   Elam, J.W., et al., *Adsorption of H₂O on a single-crystal α-Al₂O₃(0001) surface.* The Journal of Physical Chemistry B, 1998. **102**.

8.   Braunschweig, B., S. Eissner, and W. Daum, *Molecular structure of a mineral/water Interface: effects of surface nanoroughness of α-Al₂O₃(0001).* The Journal of Physical Chemistry C, 2008. **112**(6): p. 1751-1754.

9.   Petrik, N.G., et al., *Molecular water adsorption and reactions on α-Al₂O₃(0001) and α-alumina particles.* The Journal of Physical Chemistry C, 2018. **122**(17): p. 9540-9551.

10.   Tong, Y., et al., *Optically probing Al-O and O-H vibrations to characterize water adsorption and surface reconstruction on alpha-alumina: an experimental and theoretical study.* The Journal of Chemical Physics, 2015. **142**(5): p. 054704.

11.   Liu, P., et al., *Reaction of water vapor with α-Al₂O₃(0001) and α-Fe₂O₃(0001) surfaces: synchrotron X-ray photoemission studies and thermodynamic calculations.* Surface Science, 1998. **417**(1): p. 53-65.

12.   Zhang, L., et al., *Structures and charging of α-Alumina (0001)/water interfaces studied by sum-frequency vibrational spectroscopy.* Journal of the American Chemical Society, 2008. **130**(24): p. 7686-7694.

13.   Richardson, H., et al., *Freezing of water on alpha-Al₂O₃ surfaces*, in *Physics and Chemistry of Ice: proceedings of the 11th International Conference on the Physics and Chemistry of Ice*. 2007, The Royal Society of Chemistry: Bremerhaven, Germany. p. 513.

14.   Flörsheimer, M., et al., *Hydration of mineral surfaces probed at the molecular level.* Langmuir, 2008. **24**(23): p. 13434-13439.

15.   Smit, W., et al., *Zeta-potential and radiotracer adsorption measurements on EFG α-Al₂O₃ single crystals in NaBr solutions.* Journal of Colloid and Interface Science, 1980. **78**(1): p. 1-14.

16.   Yeganeh, M., et al., *Vibrational spectroscopy of water at liquid/solid interfaces: crossing the isoelectric point of a solid surface.* Physical Review Letters, 1999. **83**(6): p. 1179-1182.

17.   Kurita, T., K. Uchida, and A. Oshiyama, *Atomic and electronic structures of α-Al₂O₃ surfaces.* Physical Review B, 2010. **82**(15).

18.   Catalano, J.G., *Relaxations and interfacial water ordering at the corundum (110) surface.* The Journal of Physical Chemistry C, 2010. **114**: p. 6624–6630.

19.   Sung, J., Y.R. Shen, and G.A. Waychunas, *The interfacial structure of water/protonated α-Al₂O₃(11-20) as a function of pH.* Journal of Physics: Condensed Matter, 2012. **24**(12): p. 124101.

20. Bolt, P.H., et al., *The interaction of thin NiO layers with single crystalline α-Al$_2$O$_3$(11-20) substrates.* Surface Science, 1995. **329**(3): p. 227-240.

21. Bolt, P.H., et al., *Interfacial reaction of NiO with Al$_2$O$_3$(11-20) and polycrystalline α-Al$_2$O$_3$.* Applied Surface Science, 1995. **89**(4): p. 339-349.

22. Kotula, P.G., et al., *Kinetics of thin-film reactions of nickel oxide with alumina: I, (0001) and (11-20)reaction couples.* Journal of the American Ceramic Society, 1998. **81**(11): p. 2869-2876.

23. Sung, J., G.A. Waychunas, and Y.R. Shen, *Surface-induced anisotropic orientations of interfacial ethanol molecules at air/sapphire(1-102) and ethanol/sapphire(1-102) interfaces.* The Journal of Physical Chemistry Letters, 2011. **2**(14): p. 1831-1835.

24. Liu, Y., et al., *Termination, stability and electronic structures of α-Al$_2$O$_3$(0114) surface: An ab initio study.* Applied Surface Science, 2014. **303**: p. 210-216.

Appendix

Sample used in this work

Chapter 3: α-Al$_2$O$_3$(11-20) single crystal used in this chapter is differs from those used in later chapters as introduced in section 2.1.2: it is 10x15 mm with one side polished to roughness < 0.5 nm, the thickness is 1 mm. The treatment of the surface is the same as being described in section 2.1.2. Sample mounting in this work is shown in Figure 2. 4.

Chapter 4, Chapter 5 and Chapter 6: it is round crystal with diameter =15 mm, polished on one side to a roughness < 0.5 nm (MaTeck. Corp) and has a thickness of 1 mm. Sample mounting in these works is shown in Figure 2. 3.

SFG data simulation

We employ the Levenberg-Marquart algorithm, as implemented in the data analysis program Igor Pro (Wavemetrics) to actually fit the SFG data in chapter 3, 5 and 6. For the analysis of the low frequency Al-O (H) response of one sample in chapter 5 and 6, we have assumed that the center frequency and line width of one resonance are the same for all the components of $\chi^{(2)}$ because all components of the $\chi^{(2)}$ sample the same underlying resonance.

Publications

Yanhua Yue, Sophia Heiden, Yujin Tong, Peter Saalfrank and R. Kramer Campen. *An optical study on surface reconstruction of α-Al$_2$O$_3$(11-20) induced by water adsorption: from UHV conditions to ambient.* To be submitted.

Yanhua Yue, Harald Kirsch, Martin Thämer, R. Kramer Campen. *TPD Study on thermodynamics of water desorption on α-Al$_2$O$_3$.* To be submitted.

Yanhua Yue, Giacomo Melani, Peter Saalfrank, R. Kramer Campen and Yujin Tong. *Probing surface phonon of α-Al$_2$O$_3$ (0001) both in ultrahigh vacuum and ambient conditions with sum frequency generation.* To be submitted.

Sophia Heiden, Yanhua Yue, Harald Kirsch, Jonas Wirth, Peter Saalfrank and R. Kramer Campen.*Water dissociative adsorption on α-Al$_2$O$_3$(11-20) is controlled by surface site undercoordination, density, and topology.* J. Phys. Chem. C, 2018, 122, 6573−6584.

Acknowledgement

I would like to thank Prof. Dr. Martin Wolf for leaving the topic of the present dissertation, as well as the funding support for my extended study in Fritz-Haber Institute.

A special thanks goes to Prof. Dr. R. Kramer Campen, who was my advisor and the leader of my working group for the last five years in FHI, for his valuable suggestions on the proceeding of the whole study, great efforts on each sentence of this thesis, and nice and convenient working environment he provided during these years.

Furthermore I would like to thank Dr. Yujin Tong, who spent a lot of his time especially on the second part of this work, both in experiment and data analysis, and help solve scientific problems with his patient and rich knowledge.

And I want to thank Dr. Harald Kirsch who helped me in the beginning of my research, especially helped me with all UHV stuffs, to build the new and repair the broken, without his effort the first part work in the thesis won't be finished until now.

I would also like to thank Dr. Sophia Heiden and Dr. Giacomo Melani from the research group of

Prof. Dr. Peter Saalfrank at the University of Potsdam for their wonderful calculations to the water/alumina systems.

Many thanks should be given to Dr. Martin Thamer for his great help in programming with igor for TPD data analysis and Frank Quadt for his efforts with labview program for UHV controlling. And many thanks to all the colleagues in Kramer's group who contributed to the amounting of the new UHV system and movement of the lab from Fabeckstraβe to building G.

CV

Since 09. 2014	PhD thesis	*"Towards understanding the interaction of water with α-Al$_2$O$_3$ surfaces: a sum frequency gerneration perspective"*
		Fritz Haber Institute, MPG, Berlin, Germany
		Supervisor Prof. Dr. Martin Wolf,
		Co-supervisor Prof. Dr. R. Kramer Campen
07. 2012–07.2014	R&D Engineer	Synthesis and optimizing LiFePO$_4$ for energy storage in Lithium ion battery (LIBs).
		Pulead Co., Beijing , China
09. 2009-07. 2012	Master	*"High performance energy storage material for LIBs"*
		Qingdao Institute of Bioenerg and Bioprocess Technology,
		Chinese Academy of Sciences, China
		Supervisor: Prof. Dr. Guanglei Cui
09. 2005-07. 2009	Bachelor	*Bioengineering*
		Beijing University of Chemical Technology, China